DISSERTATION

RARE B DECAYS TO STATES CONTAINING A J/ψ MESON

Submitted by

Jinlong Zhang

Department of Physics

In partial fulfillment of the requirements

for the Degree of Doctor of Philosophy

Colorado State University

Fort Collins, Colorado

Summer 2002

ProQuest Information and Learning Company
300 North Zeeb Road
P.O. Box 1346
Ann Arbor, MI 48106-1346

COLORADO STATE UNIVERSITY

June 24, 2002

WE HEREBY RECOMMEND THAT THE DISSERTATION PREPARED UNDER OUR SUPERVISION BY JINLONG ZHANG ENTITLED RARE B DECAYS TO STATES CONTAINING A J/ψ MESON BE ACCEPTED AS FULFILLING IN PART REQUIREMENTS FOR THE DEGREE OF DOCTOR OF PHILOSOPHY.

Committee on Graduate Work

Adviser

Department Head

ABSTRACT OF DISSERTATION

Rare B Decays to States Containing a J/ψ Meson

Results are presented on preliminary measurements of the branching fractions for $B^+ \to J/\psi\phi K^+$, $B^0 \to J/\psi\phi K^0_S$, $B^0 \to J/\psi\phi$, $B^0 \to J/\psi\eta$ and $B^0 \to J/\psi\eta'$ using 56 million $B\bar{B}$ events collected at the $\Upsilon(4S)$ resonance with the *BABAR* detector at PEP-II. We measure branching fractions of $\mathcal{B}(B^+ \to J/\psi\phi K^+)=(4.4 \pm 1.4(stat) \pm 0.5(syst))\times 10^{-5}$ and $\mathcal{B}(B^0 \to J/\psi\phi K^0_S)=(5.1 \pm 1.9(stat) \pm 0.5(syst))\times 10^{-5}$, and set upper limits at 90% C.L. for branching fractions $\mathcal{B}(B^0 \to J/\psi\phi) < 9.2\times 10^{-6}$, $\mathcal{B}(B^0 \to J/\psi\eta) < 2.7 \times 10^{-5}$, and $\mathcal{B}(B^0 \to J/\psi\eta') < 6.3 \times 10^{-5}$.

Jinlong Zhang
Department of Physics
Colorado State University
Fort Collins, CO 80523
Summer 2002

Acknowledgments

It is a pleasure to thank my advisor Prof. John Harton. His guidance and continuous support made this work possible.

Prof. Walter Toki and Prof. Robert Wilson in the CSU HEP group provided generous help in the last four years. Their valuable ideas and suggestions always lead my work to new progress. It is wonderful to work in this team.

I would like to express my appreciation to Dr. William Dunwoodie. Dr. Stephen Wagner. Prof. Riccardo Faccini. and Prof. Christos Touramanis. They are great resources for my work in the tracking group and the charmonium group. Dr. Yuval Grossman clarified many theoretical confusions. I also want to thank Dr. Wei Yang. Dr. Abner Soffer. Dr. Johan Blouw. Dr. Stefan Spanier and Ms. Mahalaxmi Krishnamurthy. Their numerous suggestions. comments and discussions on all aspects are significantly illuminating.

I gratefully thank Dr. Dahua Zhang. a physicist with high intellectual power and warm feeling to people as well.

Finally. I would like to thank my parents and my sister for their years of encouragement and help.

Preface

This document includes the main work done by the author at the *BABAR* experiment. The search for five rare B decay modes, $J/\psi\omega$, $J/\psi\eta$, $J/\psi\eta'$, $J/\psi\omega K^+$, and $J/\psi\omega K_S^0$ is described. The details have been arranged into six chapters covering material from the theory introduction to the preliminary experimental results.

Chapter 1 briefly overviews the four theory topics related with this analysis. Together with the exclusive modes such as $B^0 \to J/\psi K^0$, some inclusive B decays can also be used to study CP violation to clarify further the theoretical uncertainties. The decays $B^0 \to J/\psi\eta$, $B^0 \to J/\psi\eta'$ are categorized into one type of these final states. The decay dynamics for two-body hadronic B decays are approached with some predictions on branching fractions and $\eta - \eta'$ mixing. A very rare decay mechanism without thorough understanding, the rescattering process as in $B^0 \to J/\psi\omega$, is introduced with some naive assumptions. Then the search for a possible hybrid state $\psi_g(4.3GeV)$ in $B \to J/\psi\omega K$ decays is explained.

Chapter 2 introduces the PEP-II accelerator and the main components of the *BABAR* detector. The *BABAR* detector contains a five-layer silicon vertex tracker (SVT) and a forty-layer drift chamber (DCH) in a 1.5 T solenoidal magnetic field. These devices detect charged particles and measure their momentum and energy loss. Photons and neutral hadrons are detected in a CsI(Tl) crystal electromagnetic calorimeter (EMC). The EMC detects photons with energies as low as 20 MeV and

identifies electrons by their large energy deposit. The charged particle identification (PID) combines SVT and DCH track energy loss measurements and particle velocity measurements by an internally reflecting ring-imaging Cherenkov detector (DIRC) of quartz bars circumjacent to the DCH. The slotted steel flux return is instrumented with 18-19 layers of planar resistive plate chambers (IFR). The IFR identifies penetrating muons and neutral hadrons. A quick overview of the trigger system and the online system is also included.

Chapter 3 describes the data used in this analysis. The real data were collected in two periods. October 1999 to October 2000 (Run1) and February 2001 to December 2001 (Run2). They correspond to a total integrated luminosity of 50.9 fb^{-1} taken on the $\Upsilon(4S)$ resonance and 6.3 fb^{-1} taken off-resonance at an energy 0.04 GeV below the $\Upsilon(4S)$ center of mass energy and below the threshold for $B\bar{B}$ production. There are 55.5 ± 0.9 million $B\bar{B}$ events ($N_{B\overline{B}}$) in this data set. The raw data were taken by an on-line system, then reconstructed after some background filtering, and skimmed to small data sets for physics analysis. This analysis also depends on a detailed simulation of the events and the detector, i.e., Monte Carlo (MC) data. The MC events were generated with comparable equivalent luminosity as real data.

Chapter 4 starts with the selection of single tracks and photons, then explains the PID system for charged particles, $e^{\pm}, \mu^{\pm}, \pi^{\pm}$ and $K^{\pm}$. All intermediate state particles are constructed with the right particle combinations in the required mass

window. Some specific angular cuts are introduced. The B candidates are built for every exclusive decay mode.

Chapter 5 explains how to evaluate the background. The background has two components. the combinatoric background and the peaking background. The normalization of the combinatoric background for each mode is obtained from a fit to the distributions of the energy-substituted mass of the on-peak data. This method has been checked with MC simulation. off-peak data and some special on-peak data samples. The peaking background is determined from a sample of MC $B\overline{B}$ events that is normalized to the equivalent data integrated luminosity and contains at least one decay of $J/\psi \rightarrow$ leptons.

Chapter 6 includes three parts. The raw efficiency for selection of signal events was calculated as the ratio between the number of MC signal events passing all cuts and the total MC events generated. Several corrections were applied to the raw efficiency because of the discrepancies between the real data and MC in a few areas. The yield is calculated from the total number of events in a 3σ signal box. minus the total background. Several systematic uncertainties are considered: the uncertainty in the number of $B\overline{B}$ events. the uncertainty from secondary branching fractions. the MC statistical error. the uncertainties in PID. tracking efficiency and photon detection efficiency. the uncertainty from the variations in the event selection criteria. and the uncertainty from background parameterization.

Chapter 7 shows the preliminary results on the branching fractions for two $B \rightarrow J/\psi K$ modes and the upper limits for the other three modes. The branching fraction results are consistent with the existing experimental results but statistically improved. So far no conclusion can be drawn for the existence of ψ_g state. This first measurement of the upper limit on $B^0 \rightarrow J/\psi\omega$ mode supports the factorization hypothesisand can lead to theoretical improvments and experimental clarification. The measurement of the upper limit on $B \rightarrow J/\psi\eta$ pushes the exsiting result down by two orders. The result on $B \rightarrow J/\psi\eta'$ is the first measurement.

BABAR is a collaboration of some 600 people. and the studies and physics analysis I have done would not have been possible without this enormous collective effort. which includes the building of the detector. and the acquisition and reconstruction of the data. not to mention the running of the PEP-II accelerator. I profited from countless pointers and suggestions on BaBar computing from my collaborators and from many conversations with theorists.

Contents

List of Figures

List of Tables

LIST OF TABLES

Chapter 1

CP Violation and Hadronic B Decays

1.1. CKM Matrix and CP Violation

1.1.1. $C.P.T$ Transformations

The group of Lorentz transformations includes the proper continuous transformations and the discrete transformations. For a field theory Lagrangian, three discrete transformations imply potential symmetries. Charge conjugation, performed by the unitary operator C, changes the particle to the corresponding antiparticle. Space inversion, performed by the Hermitian operator P, transfers a left-handed system into a right-handed system. Time reversal, performed by the anti-unitary operator T, leads to the interchange between the initial state and the final state. The combined CP transformation changes a particle to its antiparticle and flips the momentum and the helicity. The product of three transformations $C.P.T$ applied in any order is

always an exact symmetry if a local field is Lorentz invariant and satisfies the spin-statistics requirement (Boson fields obey commutation rules and fermion fields obey anti-commutation rules) [1].

Of the four fundamental forces, gravitation is C, P and T invariant. The electromagnetic interaction and the strong interaction are always symmetric under C, P and T operations. The weak interactions violate C and P symmetries, but conserve T and CP in most cases. Only in the neutral K system [2] and the B system [3], a small breakdown of CP invariance has been observed.

1.1.2. Quark Mixing

The Standard Model (SM) is a gauge theory based on the local group $SU(3)_C \times SU(2)_L \times U(1)_Y$, which describes the strong interaction ($SU(3)_C$) [4], and the unification of the electromagnetic interaction and the weak interaction: the electroweak interaction ($SU(2)_L \times U(1)_Y$) [5]. The Lagrangian of the SM theory contains: (1) gauge potentials (propagators of force), (2) matter fields (quarks and leptons), (3) Higgs fields (mass terms for the gauge bosons and matter fields through spontaneous symmetry breaking).

In the unbroken $SU(2)_L \times U(1)_Y$ gauge theory, the eigenstates of the three gen-

erations of quarks are

$$Q_{jL} = \begin{pmatrix} u_{jL} \\ d_{jL} \end{pmatrix}, \quad u_{jR}, \quad d_{jR}, \qquad j = 1, 2, 3. \tag{1.1}$$

For the j-th generation, they include a left-handed doublet Q_{jL} and right-handed singlets, u_{jR} and d_{jR}. In order to generate quark mass, the single Higgs scalar doublet ϕ is needed. The Yukawa couplings of quarks with the single Higgs scalar doublet are given by

$$\mathcal{L}_Y = -G_{ij}\overline{Q_{iL}}\phi d_{jR} - F_{ij}\overline{Q_{iL}}\tilde{\phi}u_{jR} + \text{hermitian conjugate}. \tag{1.2}$$

where the interaction depends on the 18 elements of two 3×3 matrices, G and F. With spontaneous symmetry breaking and the substitution of $\phi^0 \rightarrow \sqrt{\frac{1}{2}}(v + H^0)$, the mass terms appear in $\mathcal{L}_Y$:

$$\mathcal{L}_M = -\sqrt{\frac{1}{2}}vG_{ij}\overline{d_{iL}}d_{jR} - \sqrt{\frac{1}{2}}vF_{ij}\overline{u_{iL}}u_{jR} + \text{h.c.}. \tag{1.3}$$

The mass terms are

$$\overline{(u_1, u_2, u_3)_R}M^u \begin{pmatrix} u_1 \\ u_2 \\ u_3 \end{pmatrix}_L + h.c., \quad \overline{(d_1, d_2, d_3)_R}M^d \begin{pmatrix} d_1 \\ d_2 \\ d_3 \end{pmatrix}_L + h.c. \tag{1.4}$$

where $M^d_{ij} = \frac{v}{\sqrt{2}}G_{ij}$ and $M^u_{ij} = \frac{v}{\sqrt{2}}F_{ij}$ are quark mass matrices in generation space.

each with 9 complex parameters. By applying a unitary transformation on the quark states of the unbroken electroweak theory.

$$(u_1, u_2, u_3)_{L,R} = U_{L,R} \begin{pmatrix} u \\ c \\ t \end{pmatrix}_{L,R} \quad . \quad (d_1, d_2, d_3)_{L,R} = D_{L,R} \begin{pmatrix} d \\ s \\ b \end{pmatrix}_{L,R} \quad . \tag{1.5}$$

M^u and M^d are diagonalized.

$$U_R^{-1} M^u U_L = \begin{pmatrix} m_u & 0 & 0 \\ 0 & m_c & 0 \\ 0 & 0 & m_t \end{pmatrix} . \quad D_R^{-1} M^d D_L = \begin{pmatrix} m_d & 0 & 0 \\ 0 & m_s & 0 \\ 0 & 0 & m_b \end{pmatrix} . \tag{1.6}$$

where U_R, U_L, D_R and D_L are unitary matrices, and the diagonal elements are quark masses. The weak eigenstates u_1, u_2, u_3 are linear superpositions of the mass eigenstates u, c, t and the analogous relation for d_1, d_2, d_3 and d, s, b.

The charged current interaction of the $SU(2)_L$ gauge bosons under the unbroken symmetry is given by

$$\mathcal{L}_W = -\frac{1}{2} g \overline{Q_{iL}} \gamma^\mu \tau^a 1_{ij} Q_{jL} W_\mu^a . \tag{1.7}$$

After symmetry breaking, it is described with the distinguishable quark doublets and gauge bosons.

$$\mathcal{L}_W = -\sqrt{\frac{1}{2}} g \overline{u_{iL}} \gamma^\mu 1_{ij} d_{jL} W_\mu^+ + \text{h.c.}, \tag{1.8}$$

or in the mass eigenbasis.

$$\mathcal{L}_{W^-} = -\sqrt{\frac{1}{2}} g \overline{u_{iL}^m} \gamma^\mu V_{ij} d_{jL}^m W_\mu^+ + \text{h.c.}. \tag{1.9}$$

Quark fields with superscript m denote mass eigenbasis. The matrix $V = U_L^\dagger D_L$ is the mixing matrix for three quark generations.

1.1.3. CKM Matrix

The complex matrix V is unitary. Thus it only has 9 independent parameters. which can be chosen as three real angles and six phases. Without changing the diagonal mass matrix. more transformations can remove 5 phases. The remaining phase is called Kobayashi-Maskawa phase [6]. δ_{KM}. The matrix is called the CKM matrix [7].

$$V = \begin{pmatrix} V_{ud} & V_{us} & V_{ub} \\ V_{cd} & V_{cs} & V_{cb} \\ V_{td} & V_{ts} & V_{tb} \end{pmatrix}. \tag{1.10}$$

The CKM matrix can be parameterized as [8].

$$V = \begin{pmatrix} c_{12}c_{13} & s_{12}c_{13} & s_{13}e^{-i\delta} \\ -s_{12}c_{23} - c_{12}s_{23}s_{13}e^{i\delta} & c_{12}c_{23} - s_{12}s_{23}s_{13}e^{i\delta} & s_{23}c_{13} \\ s_{12}s_{23} - c_{12}c_{23}s_{13}e^{i\delta} & -c_{12}s_{23} - s_{12}c_{23}s_{13}e^{i\delta} & c_{23}c_{13} \end{pmatrix}. \tag{1.11}$$

where $c_{ij} = cos\theta_{ij}$ and $s_{ij} = sin\theta_{ij}$.

Another parameterization method is to expand the CKM matrix in terms of four parameters. λ, A, ρ and η, called the Wolfenstein parameters [9]. Here $\lambda = |V_{us}| = 0.22$ is the expansion parameter and η represents the CP-violating phase.

$$V = \begin{pmatrix} 1-\frac{\lambda^2}{2} & \lambda & A\lambda^3(\rho - i\eta) \\ -\lambda & 1-\frac{\lambda^2}{2} & A\lambda^2 \\ A\lambda^3(1-\rho-i\eta) & -A\lambda^2 & 1 \end{pmatrix} + O(\lambda^4). \tag{1.12}$$

Generally it is sufficient to keep the first few terms in the expansion. Because λ is small, the expansion parameter for each element in V is at λ^2.

The relation between the parameters of (1.11) and (1.12) is given by

$$s_{12} \equiv \lambda, \quad s_{23} \equiv A\lambda^2, \quad s_{13}e^{-i\delta} \equiv A\lambda^3(\rho - i\eta). \tag{1.13}$$

The unitarity of the CKM matrix leads to three useful relations among its elements:

$$V_{ud}V_{us}^* + V_{cd}V_{cs}^* + V_{td}V_{ts}^* = 0. \tag{1.14}$$

$$V_{us}V_{ub}^* + V_{cs}V_{cb}^* + V_{ts}V_{tb}^* = 0. \tag{1.15}$$

$$V_{ud}V_{ub}^* + V_{cd}V_{cb}^* + V_{td}V_{tb}^* = 0. \tag{1.16}$$

In the complex plane the three relations above can be represented as triangles. The Unitarity Triangle, which is the triangle associated with the relation 1.16, is shown

in Figure 1.1 after rescaling.

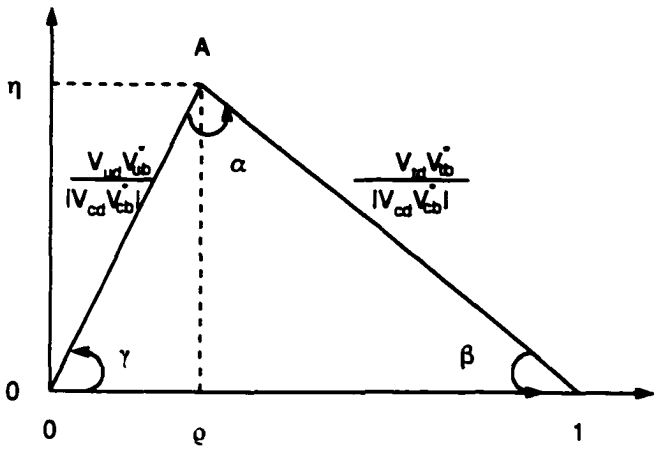

Figure 1.1: Unitarity Angle.

The three angles of the Unitarity Triangle. α. β and γ can be given:

$$\alpha \equiv \arg\left[-\frac{V_{td}V_{tb}^*}{V_{ud}V_{ub}^*}\right], \quad \beta \equiv \arg\left[-\frac{V_{cd}V_{cb}^*}{V_{td}V_{tb}^*}\right]. \tag{1.17}$$

and

$$\gamma \equiv \arg\left[-\frac{V_{ud}V_{ub}^*}{V_{cd}V_{cb}^*}\right] \equiv \pi - \alpha - \beta. \tag{1.18}$$

Or using Wolfenstein parameters. they can be expressed as

$$\sin 2\alpha = \frac{2\bar{\eta}[\bar{\eta}^2 + \bar{\rho}(\bar{\rho}-1)]}{[\bar{\eta}^2 + (1-\bar{\rho})^2][\bar{\eta}^2 + \bar{\rho}^2]}, \quad \sin 2\beta = \frac{2\bar{\eta}(1-\bar{\rho})}{\bar{\eta}^2 + (1-\bar{\rho})^2}. \tag{1.19}$$

where

$$\bar{\rho} = \rho(1 - \lambda^2/2). \quad \bar{\eta} = \eta(1 - \lambda^2/2). \tag{1.20}$$

1.1.4. CP Violation Conditions

The single complex phase in the CKM matrix can result in CP violation. But CP is not necessarily violated in the three generations of quarks. If two quarks of the same charge have same masses, one mixing angle and the phase can be removed from V. So CP violation requires

$$(m_t^2 - m_c^2)(m_c^2 - m_u^2)(m_t^2 - m_u^2)(m_b^2 - m_s^2)(m_s^2 - m_d^2)(m_b^2 - m_d^2) \neq 0. \tag{1.21}$$

Furthermore, if the phase equals to 0 or π, V is a real matrix and CP is conserved. And if one mixing angle equals 0 or $\pi/2$, the phase can be removed in matrix V. Thus CP violation requires the phase not be 0 or π and all three mixing angles not be 0 or $\pi/2$ as well.

All fourteen conditions above together ensure CP violation. If CP is violated, there exists no mass basis with the necessary phase convention where all interaction couplings and masses are real.

1.2. CP Violation in a Coherent $B\bar{B}$ System

1.2.1. CP Violation Mechanism

For the neutral B system. the mass eigenstates are not flavor eigenstates. $B^0(\bar{b}d)$ and $\bar{B}^0(b\bar{d})$. And if CP is not a good symmetry. the mass eigenstates are also not CP eigenstates. The mass eigenstates B_H and B_L can be given by the combinations:

$$|B_H >= p|B^0 > -q|\bar{B}^0 >. \tag{1.22}$$

$$|B_L >= p|B^0 > +q|\bar{B}^0 >. \tag{1.23}$$

where p and q are complex coefficients. and governed by the time-dependent Schrodinger equation

$$i\frac{d}{dt}\begin{pmatrix} p \\ \\ q \end{pmatrix} = (\mathbf{M} - \frac{i}{2}\mathbf{\Gamma})\begin{pmatrix} p \\ \\ q \end{pmatrix}. \tag{1.24}$$

Matrix $\mathbf{M}$ and $\mathbf{\Gamma}$ are given by summing over intermediate states in second-order perturbation theory. The ratio q/p can be obtained as

$$\left|\frac{q}{p}\right| = \frac{\Delta m_B - \frac{i}{2}\Delta\Gamma_B}{2(M_{12} - \frac{i}{2}\Gamma_{12})} = -\frac{2(M_{12}^* - \frac{i}{2}\Gamma_{12}^*)}{\Delta m_B - \frac{i}{2}\Delta\Gamma_B}. \tag{1.25}$$

where M_{12} and Γ_{12} are the off-diagonal terms in the corresponding matrices. The mass difference and the width difference are defined as follows:

$$\Delta m = m_H - m_L. \tag{1.26}$$

$$\Delta\Gamma = \Gamma_H - \Gamma_L. \tag{1.27}$$

Considering decays of B^0 and $\bar{B}^0$ to a final state f. we have two amplitudes:

$$A_f = < f|H|B^0 >. \tag{1.28}$$

$$\bar{A}_f = < f|H|\bar{B}^0 > . \tag{1.29}$$

If CP is conserved. there are three relations.

$$|A_f| = |\bar{A}_{\bar{f}}|. \quad |A_{\bar{f}}| = |\bar{A}_f|. \tag{1.30}$$

$$\left|\frac{q}{p}\right| = 1. \tag{1.31}$$

$$arg(\frac{p^2}{q^2} A_f \bar{A}_f^* A_{\bar{f}} \bar{A}_{\bar{f}}^*) = 0. \tag{1.32}$$

The possible CP violations can be categorized by this three relations:

- Direct CP violation. or CP violation in decay. in which the amplitude of a decay is different from that of its CP conjugate process. Equation 1.30 does

not hold. It applies to both the neutral B system and the charged B system.

- Indirect CP violation, or CP violation in mixing, in which the two mass eigenstates are not the CP eigenstates for the neutral meson system. Equation 1.31 does not hold.

- Interference between mixing and decay, in which B^0 and $\bar{B}^0$ decay to the common final states. Equation 1.32 does not hold.

To a good approximation, CP violation from the interference between mixing and decay is the only effect at *BABAR*[1]. For the neutral B system, the effect can be given by the asymmetries in the decays to CP eigenstates f_{CP}:

$$a_{f_{CP}} = \frac{\Gamma(\bar{B}^0_{\rm phys}(t) \to \bar{f}_{CP}) - \Gamma(B^0_{\rm phys}(t) \to f_{CP})}{\Gamma(\bar{B}^0_{\rm phys}(t) \to \bar{f}_{CP}) + \Gamma(B^0_{\rm phys}(t) \to f_{CP})}. \tag{1.33}$$

$\bar{B}^0_{\rm phys}(t)$ is a physically observed state that has evolved from an initially pure $\bar{B}^0$ state at $t = 0$. The analogous definition is applied to $B^0_{\rm phys}(t)$. A useful variable is defined to quantify the CP violation for the final state f_{CP}:

$$\lambda_{f_{CP}} = \frac{q}{p}\frac{\bar{A}_{f_{CP}}}{A_{f_{CP}}}. \tag{1.34}$$

[1]In a heavy meson system, if the small nonzero $1 - \left|\frac{q}{p}\right| \sim 10^{-3}$, which leads to CP violation in mixing, is neglected. Equation 1.32 is equivalent to $Im\lambda_f = 0$ if the final state f is a CP eigenstate. For B decays $Im\lambda_f$ can be large in SM prediction. An example is $Im\lambda_{J/\psi K^0_S} = sin(2\beta) = 0.75$.

1.2.2. CP Violation in Inclusive $b \to c\bar{c}d$ Decays

Generally the CP final states used to extract CP asymmetry are exclusive states. One example is the B decay to the CP odd final state $J/\psi K_S^0$.

$$\lambda_{J/\psi K_S^0} = -\left(\frac{V_{tb}^* V_{td}}{V_{tb} V_{td}^*}\right)\left(\frac{V_{cb} V_{cs}^*}{V_{cb}^* V_{cs}}\right)\left(\frac{V_{cd}^* V_{cb}}{V_{cd} V_{cb}^*}\right). \quad Im\lambda_{J/\psi K_S^0} = \sin(2\beta). \tag{1.35}$$

But the final state f can also be an inclusive state. which includes all final states associated with a special category of quark decay. The possible inclusive final states with charmed particles can be used to measure CP angle β if they have total strange number $S = 0$ and total charm number $C = 0$ [10]. The quark transition is $b \to c\bar{c}d$ or $\bar{b} \to c\bar{c}\bar{d}$. and the decay modes include $B \to J/\psi\eta$. $B \to J/\psi\eta'$. The total branching fraction of $b \to c\bar{c}d$ is $\sim 1\%$ of the total B decay. The CP related equation is:

$$Im\xi = Im\frac{M_{12}^*}{|M_{12}|}\frac{\Gamma_{f,12}}{\Gamma_{f,11}} = \mathsf{d} \cdot sin2\beta. \tag{1.36}$$

The definition of $\Gamma_{f,ij}$ is

$$\Gamma_{f,ij} = \sum_k < i|f_k >< f_k|j >. \tag{1.37}$$

where i, j are B^0 and $\bar{B}^0$ and f is the final state sums over the total possible channel

k. d is called the dilution factor. which is the part in $Im\xi$ with CKM factor excluded[2]. A value of $d = -0.41$ can be obtained with quark mass $m_b = 4.8$ GeV. $m_c = 1.4$ GeV and renormalization scale equal to m_b. and decay constant $f_B = 180$ MeV [10].

The calculation above requires strong assumptions and has a large theoretical uncertainties [10]. The contribution below the leading order is neglected.

1.3. Two-body Hadronic *B* Decays

1.3.1. Factorization

In *B* decays to hadronic final states. the dynamics are quite complicated. The initial state and the final state are connected by trees of quark and gluon interactions. loops and pair productions. Soft and hard gluon exchange leads to quark rearrangement. But in the two-body decays with energetic final state particles. the complicated strong interactions could be less important in the weak Hamiltonian. This is because once the quarks are grouped into color-singlet states. the soft gluons are not effective any more. The color transparency model [11] points out the quark-antiquark pair remains a state with a small chromomagnetic moment until it is far away from the other decay products. Thus the hadronization of the final state products does not occur until they travel some distance away from each other [11]. Based on these arguments. the decay amplitude can be factorized into the product of two hadronic

[2]For the $b \to c\bar{c}d$ transition. CKM factor in $Im\xi$ is $sin2\beta$.

matrix elements of color-singlet quark states [12].

The method to calculate the amplitudes is to use the operator product expansion (OPE) [13]. which incorporates all long-distance QCD effects in the hadronic matrix elements of local four-quark operators. For example. in $b \to c\bar{c}d$ transitions (Figure 1.2). the effective Hamiltonian can be written as [14]

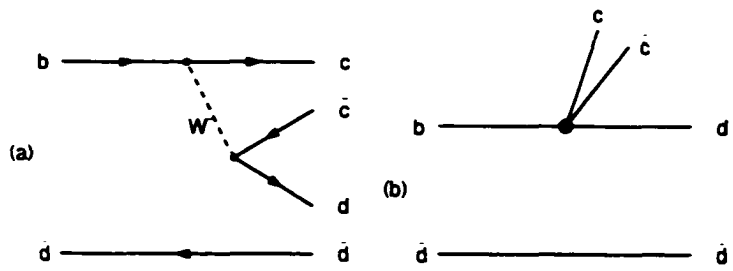

Figure 1.2: The $b \to c\bar{c}d$ transitions: (a) the color-suppressed diagram. and (b) the diagram with the local operators.

$$H_{eff} = \frac{G_F}{\sqrt{2}} V_{cb} V_{cd}^{*} [C_1(\mu)\mathcal{O}_1 + C_2(\mu)\mathcal{O}_2] + \text{penguin operators.} \tag{1.38}$$

$\mathcal{O}_1$. $\mathcal{O}_2$ are local operators.

$$\mathcal{O}_1 = \bar{c}_i \gamma^\mu (1-\gamma_5) b^i \bar{d}_j \gamma_\mu (1-\gamma_5) c^j. \tag{1.39}$$

$$\mathcal{O}_2 = \bar{c}_i \gamma^\mu (1-\gamma_5) b^i \bar{d}_j \gamma_\mu (1-\gamma_5) c^i. \tag{1.40}$$

where i. j are color indices. and $C_1(\mu)$. $C_2(\mu)$ are Wilson coefficients [13] computed

at the energy scale $\mu \approx m_b = 4.8$ GeV. At the leading logarithmic approximation [15] the values are $C_1(\mu) = 1.133$ and $C_2(\mu) = -0.291$. And some different models can be used to improve the calculation [16] [12].

In weak interactions, a meson can be generated by a quark current carrying the right parity and flavor quantum numbers. Thus the decay amplitude is factorized into two current matrix elements [17]. An example is for $\bar{B}^0 \to J/\psi\eta$, where the amplitude is

$$< J/\psi\eta|H_{eff}|B >= \frac{G_F}{\sqrt{2}} V_{cb}V_{cd}^* a_2 < J/\psi|(c\bar{c})_{V-A}|0 >< \eta|(d\bar{b})_{V-A}|B > . \qquad (1.41)$$

The coefficient a_2 is a function of $C_1(\mu)$ and $C_2(\mu)$. In the amplitude, the first matrix element $< J/\psi|(c\bar{c})_{V-A}|0 >$ is determined by the meson decay constants, and the second matrix element $< \eta|(d\bar{b})_{V-A}|B >$ is determined by the hadronic form factors.

In general, for a vector meson $V(p', \varepsilon)$, the first matrix element is parameterized [12] as

$$< 0|(V^\mu - A^\mu)|V(p', \varepsilon) >= \varepsilon^\mu m_V f_V . \qquad (1.42)$$

$V^\mu - A^\mu$ describes the weak current-current interaction. For a pseudoscalar meson $P(p')$, the first matrix element is parameterized [12] as

$$< 0|(V^\mu - A^\mu)|P(p') >= ip'^\mu f_P . \qquad (1.43)$$

The decay constants f_V, f_P can be deduced from the decay widths of the mesons obtained from experiment results.

Several models [12] can be used to obtained the second matrix element in Equation 1.41. One model adapted the semileptonic matrices which have been determined by experiments [18]. Two form factors (F_0, F_1) are needed to describe the transition to a pseudoscalar meson $P(p')$.

$$< P(p')|(V^\mu - A^\mu)|B(p) >= -\frac{M_P^2 - M_B^2}{q^2} q^\mu F_0(q^2) + [(p+p')^\mu + \frac{M_P^2 - M_B^2}{q^2}]F_1(q^2). \tag{1.44}$$

But four form factors (V, A_0, A_1, A_2) are needed to describe the transition to a vector meson $V(p', \varepsilon)$.

$$\begin{aligned} < V(p', \varepsilon)|(V^\mu - A^\mu)|B(p) > \; = \; & \frac{2V(q^2)}{M_B + M_V} \varepsilon^{\mu\nu\alpha\beta} \varepsilon^*_\nu p_\alpha p'_\beta \\ & + i\varepsilon^* \cdot q \frac{2M_V}{q^2} q_\mu A_0(q^2) \\ & + i(M_B + M_V)[\varepsilon^*_\mu - \frac{\varepsilon^* \cdot q}{q^2} q_\mu] A_1(q^2) \\ & - i\frac{\varepsilon^* \cdot q}{M_B + M_V}[(p+p')_\mu - \frac{M_P^2 - M_B^2}{q^2} q_\mu] A_2(q^2) \end{aligned} \tag{1.45}$$

All form factors can be expressed as a function of the momentum transfer q^2. To obtain these form factors we need some theoretical models [18] [12].

The results on some decays based on numerical calculations are list in Table 1.1.

Table 1.1: The predicted width and branching fractions for two -body B decays [18].

Mode	Decay width	Branching fraction
$J/\psi\pi^0$	$4.5a_2^2\|V_{cb}V_{cd}^*\|^2$	$(3.7 \pm 1.6) \times 10^{-5}$
$J/\psi\eta$	$1.2a_2^2\|V_{cb}V_{cd}^*\|^2$	$(1.0 \pm 0.4) \times 10^{-5}$
$J/\psi\rho^0$	$6.7a_2^2\|V_{cb}V_{cd}^*\|^2$	$(5.3 \pm 1.8) \times 10^{-5}$
$J/\psi\omega$	$6.7a_2^2\|V_{cb}V_{cd}^*\|^2$	$(5.3 \pm 1.8) \times 10^{-5}$

1.3.2. $\eta - \eta'$ Mixing in B Decays

By defining the non-strange and strange quark-antiquark wavefunctions as $|N>= |u\bar{u} + d\bar{d}> /\sqrt{2}$ and $|S>= |s\bar{s}>$. the normalized $\eta - \eta'$ wavefunctions are given by:

$$|\eta>= |N> \cdot cos\theta - |S> \cdot sin\theta. \tag{1.46}$$

$$|\eta'>= |N> \cdot sin\theta + |S> \cdot cos\theta. \tag{1.47}$$

In B^0 decays to $J/\psi\eta(\eta')$. η and η' are produced from the non-strange components. The decay amplitudes have the relations:

$$A(B^0 \to J/\psi\eta) = cos\theta \cdot A(B^0 \to J/\psi N). \tag{1.48}$$

$$A(B^0 \to J/\psi\eta') = sin\theta \cdot A(B^0 \to J/\psi N). \tag{1.49}$$

Thus we can estimate the relative amplitude between $B^0 \to J/\psi\eta$ and $B^0 \to J/\psi\eta'$:

$$A(B^0 \to J/\psi\eta) = cot o \cdot A(B^0 \to J/\psi\eta'). \tag{1.50}$$

It is convenient to connect the o and the ideal mixing angle, θ_P, which uses the $SU(3)$ flavor octet η_8 and singlet η_1.

$$\eta_1 = (u\bar{u} + d\bar{d} + s\bar{s})/\sqrt{3}. \tag{1.51}$$

$$\eta_8 = (u\bar{u} + d\bar{d} - 2s\bar{s})/\sqrt{6}. \tag{1.52}$$

to describe the $\eta - \eta'$ mixing:

$$|\eta> = \eta_8 \cdot cos\theta_P - \eta_1 \cdot sin\theta_P. \tag{1.53}$$

$$|\eta'> = \eta_8 \cdot sin\theta_P + \eta_1 \cdot cos\theta_P. \tag{1.54}$$

Simply, we get

$$cot o = \frac{cos\theta_P - \sqrt{2}sin\theta_P}{\sqrt{2}cos\theta_P + sin\theta_P}. \tag{1.55}$$

The experiment results favor $\theta_P = -20°$ [19]. So naively it can be predicted that the decay amplitude of $B^0 \to J/\psi\eta$ is roughly a factor of 0.8 times the decay amplitude of $B^0 \to J/\psi\eta'$. The only existing experimental result is the upper limit on the branching fraction of $B \to J/\psi\eta$ came from L3 Collaboration [20], which is $< 1.2 \times$

10^{-3}.

1.4. Rescattering in B Decays

Rescattering is a form of final state interaction (FSI) effect in which the final hadrons have interactions after their production. In many B decays, it is believed that the quasi-elastic rescattering is small but not completely negligible. Furthermore, it is believed that when the inelastic rescattering process occurs, it does strongly affect the extraction of FSI phases, which is important to estimate various rates and the effect of sub leading amplitudes [21] like direct CP violation effects.

1.4.1. Rescattering Mechanism

Rescattering processes are not in the spectator model regime, i.e., the spectator quark must also be involved in the decay. An example is $b \to c\bar{c}d$ transition in B decay, in which all quarks $c\bar{c}d\bar{d}$ including the spectator $\bar{d}$ rescatter as $c\bar{c}s\bar{s}$, leading to the final state $J/\psi\phi$ or $D_S^+ D_S^-$. Generally the decays without spectator quark also include the exchange and annihilation processes (Figure 1.3), which have the same diagrams as rescattering. Only the total effect can be studied because the long-distance rescattering effect is not distinguishable from the short-distance annihilation effect.

In many cases it is easy to calculate all inelastic production if FSI are treated as

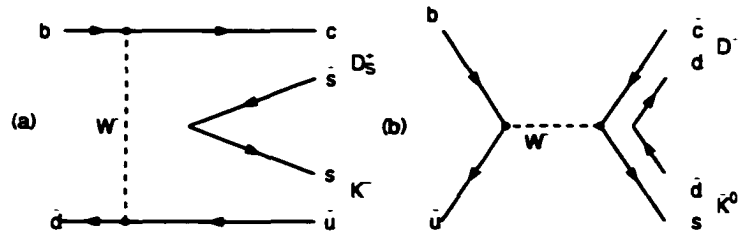

Figure 1.3: The Feynman diagrams for two processes without spectator quark: (a) exchange. and (b) annihilation.

short-distance quark-line diagrams [22]. But this assumption does not provide the correlation between the spectator quark and the products of b quark decay. which ensures that the quarks "know about" each other at some level [23]. So the long-distance mechanisms are necessary to explain the hadrons. hadron-level dynamics and the inelastic rescattering effects. An example is Regge exchange [24] [25].

Experimentally. it is difficult to measure the rescattering since in most cases it is only a subdominant effect. It is possible to search for some processes in which the whole effect is due to rescattering but they are very rare decays. This type of processes must be those charged B decays without u quark or B^0 decays without d quark in the final states. The advantage is that the amplitudes of the decays without spectator quark are predicted to be small in all known models. Thus any possible new physics probably cannot enhance them. and it is only low energy QCD that determines the effect of rescattering. So the results cannot be "contaminated" by the

presence of new physics.

1.4.2. Possible Rescattering Processes in B Decays

There are many decays that have no spectator quark. Some decays consistent with the rescattering processes from tree level transitions are listed in Table 1.4.2. Only meson final states are considered because the baryon states are much more difficult experimentally. For each decay, T means tree level and P means penguin level, and λ^0 means Cabibbo allowed, λ^1 means Cabibbo suppressed and λ^2 means doubly Cabibbo suppressed.

1.4.3. $B^0 \to J/\psi\phi$ Estimation

At the quark level the rescattering in the form of $c\bar{c}d\bar{d} \to c\bar{c}s\bar{s}$ has two processes.

$$(a)\ B^0 \to J/\psi\phi. \qquad (b)\ B^0 \to D_s^+ D_s^-. \tag{1.56}$$

Any theory model that trys to explain rescattering is expected to predict the following ratio [26].

$$R \equiv \frac{\mathcal{B}(B^0 \to J/\psi\phi)}{\mathcal{B}(B^0 \to D_s^+ D_s^-)}. \tag{1.57}$$

Subsequently the experiments can do crucial tests. The model [24] based on Regge exchange is used to describe the rescattering. Based on this model, the amplitudes

Table 1.2: Rescattering decays.

Transition	Meson	Order	Rescatter to	Final states
$b \to c\bar{u}d$	$\bar{B}^0$ $(b\bar{d})$	$T(\lambda^0)$	$\bar{s}s\bar{u}c$	$D_s^+K^-, oD^0$
			$\bar{c}c\bar{u}c$	$D^0\upsilon$
$b \to c\bar{c}d$	$\bar{B}^0$ $(b\bar{d})$	$T(\lambda^1)+P(\lambda^1)$	$\bar{u}u\bar{c}c$	$\upsilon\pi^0, D^0\bar{D}^0$
			$\bar{s}s\bar{c}c$	$\upsilon o, D_s^+D_s^-$
$b \to u\bar{u}d$	$\bar{B}^0$ $(b\bar{d})$	$T(\lambda^1)+P(\lambda^1)$	$\bar{s}s\bar{u}u$	K^+K^-
			$\bar{c}c\bar{u}u$	$D^0\bar{D}^0$
$b \to u\bar{c}d$	$\bar{B}^0$ $(b\bar{d})$	$T(\lambda^2)$	$\bar{s}s\bar{c}u$	$o\bar{D}^0$
			$\bar{c}c\bar{c}u$	$\bar{D}_0\upsilon$
			$\bar{d}d\bar{c}u$	$D^-\bar{\pi}^+$
$b \to u\bar{c}s$	B^- $(b\bar{u})$	$T(\lambda^1)$	$\bar{s}s\bar{c}s$	oD_s^-
			$\bar{c}c\bar{c}s$	$D_s^-\upsilon$
			$\bar{d}d\bar{c}s$	$D^-\bar{K}^0$
$b \to u\bar{c}d$	B^- $(b\bar{u})$	$T(\lambda^2)$	$\bar{s}s\bar{c}d$	$o\bar{D}^0$
			$\bar{c}c\bar{c}d$	$\bar{D}_0\upsilon$
			$\bar{d}d\bar{c}d$	$D^-\bar{\pi}^+$

of the two decays can be parameterized as follows.

$$A(B^0 \to J/\upsilon o) = E_1 + R_a. \qquad A(B^0 \to D_s^+D_s^-) = E_2 + Reg + R_b. \tag{1.58}$$

Here E_1, E_2 denote exchange diagram (c) and (d) from Figure 1.4. Because the couplings in two diagrams involve soft gluons, it is not clear how to determine the

relative amplitude of them. An unsolid assumption[3] is $E_1/E_2 \sim 0.04$ [27]. *Reg* denotes the Regge exchange that contribute only to $B^0 \to D_s^+ D_s^-$. R_a and R_b are the unknown rescattering amplitudes. Naively, the amplitudes of tree diagram, color-suppressed diagram and exchange diagram have relation $T : C : E_2 = 1 : \lambda : \lambda^2$ [28].

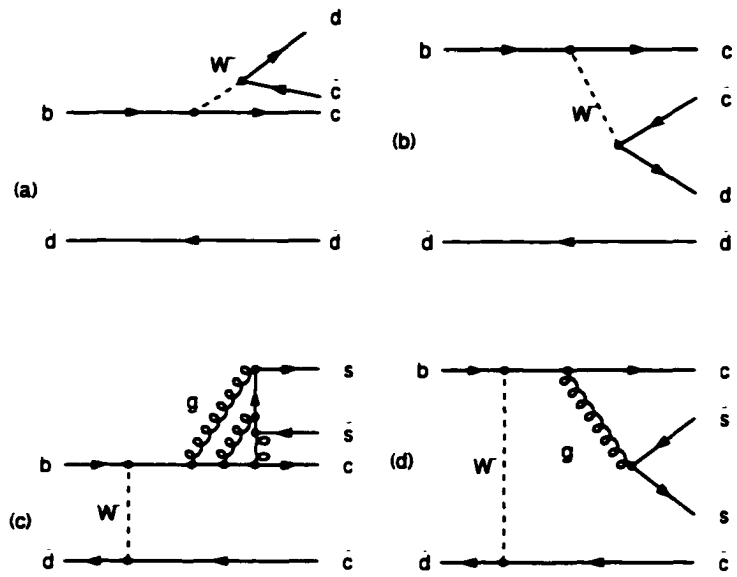

Figure 1.4: The Feynman diagram examples. (a) tree. (b) color suppressed. (c) external exchange. and (d) internal exchange.

where $\lambda^2 = f_B/m_B \sim 0.05$. Experimental results like [29] can be used to estimate the ratios such as

$$\frac{C}{T} \sim \sqrt{\frac{\mathcal{B}(B \to J/\psi\rho^0)}{\mathcal{B}(B \to D^{*+}D^{*-})}}. \tag{1.59}$$

[3]Just assume that two more gluons contribute a factor of $\alpha_s^2(m_b) = 0.04$. It can also be considered as OZI suppressed effect.

The ratio R can be quite different according to the relative size of the terms in Equation 1.58. The first case is that rescattering is very small and thus E_1 and E_2 are the dominant amplitudes. Then we use:

$$E_2/T \sim \lambda^2 \sim 0.05. \quad \mathcal{B}(B \to D^{*+}D^{*-}) \sim 8.3 \times 10^{-4}. \tag{1.60}$$

can get

$$\mathcal{B}(B^0 \to D_s^- D_s^-) \sim 2.1 \times 10^{-6}. \qquad \mathcal{B}(B^0 \to J/\psi o) \sim 3.4 \times 10^{-9}. \tag{1.61}$$

$$R \sim 1.6 \times 10^{-3}. \tag{1.62}$$

The second case is that the Reg is dominant over the short distance. For example. in [24] it is assumed $Reg/T \sim \lambda$. In that case we find

$$\mathcal{B}(B^0 \to D_s^- D_s^-) \sim 4.2 \times 10^{-5}. \qquad \mathcal{B}(B^0 \to J/\psi o) \sim 3.4 \times 10^{-9}. \tag{1.63}$$

$$R \sim 8.0 \times 10^{-5}. \tag{1.64}$$

Finally consider the case where the rescattering is not well described by the Regge exchange. and it is dominated by unknown amplitudes. R_a and R_b. In this case the ratio R can not be estimated because no known theoretical models predict R_a and R_b. It becomes an experimental question.

The amplitudes E_1 and E_2 can be calculated using the factorization assumption. But factorization is not a good approximation for some other contributions involved here. thus factorization can not improve the above estimation too much.

No experiment results on $B^0 \to J/\psi\sigma$ are available. But this rare decay can be studied with the high integrated luminosity of *BABAR*.

1.5. Searching For Hybrid States in B Decays

QCD theory allows the existence of meson states other than $|q\bar{q}>$. Because states with exotic J^{PC} have no interference with states with common J^{PC}. the search for states with exotic J^{PC} includes some hybrid states. will be feasible and interesting. Several theoretical models predicted a $|c\bar{c}g>$ hybrid state with mass 4.3GeV. which can be examined in the decays such as $B \to J/\psi\sigma K$.

1.5.1. Meson States Other Than $|q\bar{q}>$

For the strong interaction between the point-like quark. antiquark and gluon. the QCD Lagrangian is

$$\mathcal{L} = \sum_k \bar{q}_k(i\gamma^\mu\partial_\mu - m_k)q_k - g\bar{q}_k\gamma^\mu A^a_\mu(\lambda^a/2)q_k - \frac{1}{4}G^a_{\mu\nu}G^{a\mu\nu}. \qquad (1.65)$$

where $q_k(k = 1.2.3)$ are the quark fields and $A^a_\mu(a = 1.2....8)$ are the gauge fields for gluons. The theory is base on the gauging of the non-Abelian $SU(3)$ color group. The

fundamental couplings in the Lagrangian are $q\bar{q}g$ and gluon self-couplings including $g^3(ggg)$ and $g^4(gggg)$. QCD theoretically postulates that observed hadrons should be color-singlets and experimental results consistently support this rule.

The physically allowed color-singlet states can be formed by pure quarks and antiquarks, pure gluons and quark gluon combinations. In those color-singlet states formed by pure quarks plus antiquarks, there are three type of base states, baryon $|qqq>$, antibaryon $|\bar{q}\bar{q}\bar{q}>$ and meson $|q\bar{q}>$. And there may also be some reducible states in Fock space, which are called multi-quark states, such as $|q^2\bar{q}^2>$, $|qqqqqq>$, etc. Multiquark states can contribute many resonances to the meson spectrum. But the decay of a multiquark state is quite different from the decay of normal $|q\bar{q}>$ meson and it just rearranges into a state of several base meson states or baryon states [30]. This makes much harder to detect it because it could have very broad width or may not be realized as a resonance at all.

The color-singlet states formed by pure gluons, generally $|gg>$, are named glueballs. Using lattice QCD, several groups [31] predicted a $J^{PC} = 0^{++}$ glueball with mass at $\sim 1600MeV$, and a $J^{PC} = 2^{++}$ glueball with mass at $\sim 2400MeV$. The evidence for scalar glueball could be the $f_0(1500)$ found in $p\bar{p}$ annihilation experiment [32] but several states are tangled in that mass region [19]. There is a state, named as $\xi(2230)$, which could be a good candidate for 2^{++} glueball [33].

The color-singlet states formed by quark gluon mixture, i.e., $|q+\bar{q}+gluon_{excited}>$,

are hybrids states. Because $|q\bar{q}g>$ can include all flavor nonets the hybrids have a much richer spectrum.

1.5.2. Exotic States

For $q\bar{q}$ states, parity P and charge-conjugation C are given by

$$P = (-1)^{L+1}. \qquad C = (-1)^{L+S}. \tag{1.66}$$

where L is the orbital angular momentum. S is the spin and the sum of L and S is the total total angular momentum J. It is obvious for a two fermion system that some J^{PC} combinations can not arise, such as $0^{--}, 0^{+-}, 1^{-+}, 2^{+-}, 3^{-+}$, ... These states are called spin-parity exotic states. Theoretically flavor exotic states can appear as well although all experiment candidates are favored spin-parity exotics [34].

No exotic states are expected in multi-quark state spectrum. And no spin-parity exotics are expected in glueball spectrum below 4 GeV [31]. But for hybrid states all possible J^{PC} can be constructed in wide mass range with all flavor nonets. Because those exotic J^{PC} states have no interference with the conventional $q\bar{q}$ states, they are expected to be identified easily.

1.5.3. Models of Hybrid States

There are several models focusing on "excited glue" such as the flux-tube model. and the bag model. The mass and other properties can be predicted by QCD sum rules and Lattice Gauge Theory (LGT) without model assumptions. The color-charge flux tube is used to quantized the field between the separated static color sources. which is an analogous idea to the quantized magnetic flux tubes in superconductivity. The flux tube carries a finite amount of energy per unit length so that the potential rises linearly. The flux tube model [35] describes the gluons as strings of point masses connected by the linear potential. The strings can have normal excitation modes which are transverse to the string axis. The quantum numbers of hybrid systems are obtained by the combinations with the spin and the angular momentum of the $q\bar{q}$ system. which can be obtained from the rigid body wavefunctions for the string excitation. The prediction of this model has 8 J^{PC} hybrids:

$$J^{PC} = 0^{\pm\mp}.1^{\pm\mp}.1^{\pm\pm}.2^{\pm\mp}. \tag{1.67}$$

The lightest hybrid mass from the model is $1.8 \sim 1.9$ GeV. Because of 8 J^{PC} values. the model predicts 72 resonances around 2.0 GeV in addition to the standard meson spectrum.

The bag model [36] describes quarks and gluons as spherical cavity modes of

Dirac and Maxwell quanta that are confined by the color boundary conditions. The expression of the conventional mesons is $|q\bar{q}> + O(\sqrt{\alpha_s})|q\bar{q}g>$ and the expression of hybrids is $|q\bar{q}g> + O(\sqrt{\alpha_s})(|q\bar{q}> + |q\bar{q}g^2> + ...)$. In this model, the lowest quark mode is the conventional $J^P = \frac{1}{2}^+$ but the lowest gluon mode is $J^P = 1^+$. The combinations give hybrid states as:

$$J^{PC} = (0^-, 1^-) \otimes 1^+ = 0^{-+}, 1^{--}, 1^{-+}, 2^{-+}. \tag{1.68}$$

The lightest hybrid in the bag model is predicted as $\sim$ 1.5 GeV.

Both LGT and QCD sum rules use the correlation functions $< 0|\mathcal{O}(\vec{x}, \tau)\mathcal{O}^\dagger(0,0)|0>$ to calculate the hybrid masses, where the operator $\mathcal{O}$ couples the hybrid state to the vacuum. The estimation strongly depends on parameterization, approximation used and uncertainties on the high-mass contributions.

The current results [37] [38] are consistent with the flux-tube mode within statistical errors. The lightest 0^{+-} is $\sim$3 GeV while the lightest 1^{-+} is $\sim$ 2GeV. The 0^{+-} and 2^{+-} are below 2 GeV. Furthermore, the nonrelativistic heavy quark exotic hybrids have been predicted with very small statistical error. NRQCD group [39] predicted 1^{-+} hybrid with b quark at 10.99 GeV and 1^{-+} hybrid with c quark at 4.39 GeV.

1.5.4. $\psi_g(c\bar{c}g)$ (4.3 GeV) State

The charmonium system is good for study of non-perturbative QCD effects like gluonic excitations. This heavy quark system is quasi-relativistic and the $O(v/c)|ccg>$ gluonic configuration is large enough to be determined and compared with model predictions. Additionally, the $c\bar{c}$ spectrum is relatively simple and the unmixed charmonium hybrids can be clarified easily.

The theoretical prediction on the mass of 1^{--} $(c\bar{c}g)$ hybrid [37] is statistically accurate:

$$M_{c\bar{c}g}(1^{--}) = M_{c\bar{c}}(1S) + 1.323(13)\ GeV = 4.39\ GeV. \tag{1.69}$$

If the hybrid state does not mix with the conventional $q\bar{q}$ states, a general selection rule works well for heavy flavors, which says that hybrid decay modes to two mesons with the same spatial wave function are suppressed [40]. So if the $|ccg>$ state has exotic J^{PC}, say 1^{--}, which can not mix with the conventional $c\bar{c}$ excitation states, the decay modes such as D^*D^*, $\pi\pi$, $\eta\eta$, $\eta'\eta'$, are suppressed. The decays for the hybrids without mixing follow the annihilation mode $\psi_g \rightarrow (gg)$ $\rightarrow$light hadrons or the cascade mode $\psi_g(c\bar{c}g) \rightarrow (gg) + (c\bar{c})$ $\rightarrow$light hadrons+$(\psi, \eta_c, ...)$. With the annihilation mode, the hadron production rate for $\psi_g(C = -)$ is suppressed by one order of α_s compared to $\psi_g(C = +)$.

The relative width between two modes can be estimated with some simplifica-

tions [41]:

$$\Gamma(\upsilon_g(C=+) \to light\ hadrons) \sim O(20MeV). \tag{1.70}$$

$$\Gamma(\upsilon_g \to (c\bar{c}) + light\ hadrons) \sim O(0.5MeV). \tag{1.71}$$

1.5.5. υ_g in $b \to c\bar{c}s$ Transition

The Cabibbo favored transition $b \to c\bar{c}s$ is an excellent place to search υ_g. A large coupling is expected between the $c\bar{c}$ pair in υ_g and the $c\bar{c}$ pair from transition. which is dominantly produced in a color octet [42].

The recent *BABAR* measurement on the direct $B \to J/\upsilon + X$ production is $(0.74 \pm 0.01)\%$ [43]. It is somehow enhanced with respect to the calculation from the color suppressed factorization [44]. And the experimental result shows a sizable excess on the momentum of J/υ in center-of-mass frame compared to the theoretical prediction [43]. That is a hint for possible feed-down from high mass states like υ_g. Additionally. the factorization rules out the decays like $b \to c\bar{c}s \to \chi_{c2}s$ at the leading order but not $b \to c\bar{c}s \to \chi_{c1}s$. Thus if decays like $b \to c\bar{c}s \to \chi_{c2}s$ are observed at some level. there is another possible feed-down from the higher mass states [45]. The production size of υ_g can be assumed comparable to the excitation $c\bar{c}$ states like χ_{c2}. The measurements on the inclusive excitation $c\bar{c}$ states can put more constraints on it.

For the transition $b \to c\bar{c}s$. the $c\bar{c}$ mass distributions peaks near $3 - 3.7$ GeV [42]. and is more inclusive at low $M_{c\bar{c}}$ and more exclusive at high $M_{c\bar{c}}$. So $B \to J/\psi\phi K$ will be the favored decay around 4 GeV if J/ψ and ϕ come from ψ_g (4.3GeV).

In addition to the possible quasi-two-body decay $B \to \psi_g + K. \psi_g \to J/\psi\phi$. the same final states can be obtained by creating an additional $s\bar{s}$ quark pair or gluon coupling (Figure 1.5).

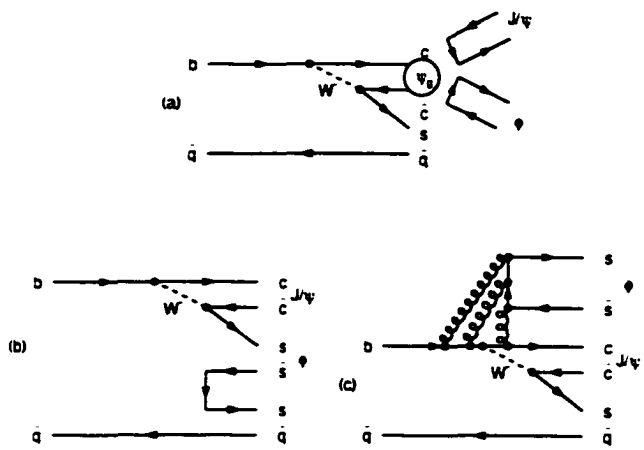

Figure 1.5: The Feynman diagrams for $B \to J/\psi\phi K$. (a). hybrid. (b). sea quark. and (c) gluon coupling.

Using 9.6×10^6 $B\overline{B}$ pairs. CLEO [46] found 8 $B^+ \to J/\psi\phi K^+$ events and 2 $B^0 \to J/\psi\phi K_S^0$ events. They obtain the branching fraction $\mathcal{B}(B \to J/\psi\phi K) = (8.8^{+3.5}_{-3.0} \pm 1.3) \times 10^{-5}$. No evidence was found for ψ_g state due to the low statistics in the Dalitz plot and the helicity plot.

1.6. Motivation and Status

In this document, five rare decays are studied. $B \to J/\psi\eta$ in two η modes. $B \to J/\psi\eta'$. $B^0 \to J/\psi\omega$. $B^+ \to J/\psi\phi K^+$ and $B^0 \to J/\psi\phi K_S^0$. The results on two-body hadronic decay $B \to J/\psi\eta$ and $B \to J/\psi\eta'$ can be used to test the color-suppressed mechanism and factorization prediction. These two decays are also in the category of the inclusive states that can be used to measure the CP angle β. The decay $B^0 \to J/\psi\omega$ is a rescattering process and its measurement can put a critical constraint on the theoretical models, and help to resolve the discrete ambiguity in the $\cos(2\beta)$ measurement with $B \to J/\psi K^*$ [47]. The decay $B^+ \to J/\psi\phi K^+$ and $B^0 \to J/\psi\phi K_S^0$ could be promising places to search hybrid states.

A summary on the current status of these modes is shown in Table 1.3.

Table 1.3: The branching fractions of five B decays.

Mode	Theoretical prediction	Existing result
$J/\psi\eta$	$(1.0 \pm 0.4) \times 10^{-5}$	$< 1.2 \times 10^{-3}$
$J/\psi\eta'$	None	None
$J/\psi\omega$	None	None
$J/\psi\phi K^+$	None	$(8.8^{+3.5}_{-3.0} \pm 1.3) \times 10^{-5}$
$J/\psi\phi K_S^0$	None	

Chapter 2

BABAR Detector

The *BABAR* experiment was designed to study *CP*-violating asymmetries in the decay of neutral B mesons to *CP* eigenstates [48]. In addition to this, precise measurements of CKM matrix elements can be performed, and many rare B meson decays can be measured, which put more constraints on the fundamental parameters of the Standard Model. Because of the high luminosity, many other physics topics can be studied, including decays of bottom and charm mesons and τ leptons, and two-photon physics.

2.1. PEP-II and the Interaction Region

The PEP-II was an upgrade of PEP (Positron Electron Project), which was an e^+e^- storage ring constructed in early 1980s. PEP-II has two rings which store different energy beams: the high energy ring for electrons of 9.0 GeV and the low

energy ring for positrons of 3.1 GeV. PEP-II operates at a center-of-mass energy of 10.58 GeV. the mass of the $\Upsilon(4S)$ resonance with design luminosity at 3×10^{33} $cm^{-2}s^{-1}$ and above. The asymmetric beams result in a Lorentz boost to the $\Upsilon(4S)$ resonance of $\beta\gamma = 0.56$. This boost makes it possible to reconstruct the decay vertices of the two B mesons which are consequently separated by $\sim 250\mu m$. to determine their relative decay times. and thus to measure the time dependence of their decay rates.

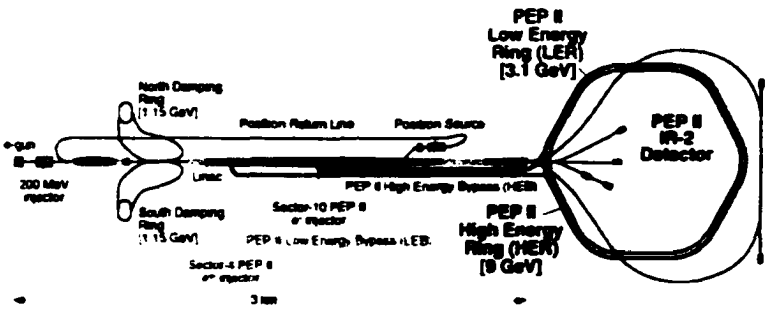

Figure 2.1: The schematic view of PEP-II.

A schematic representation of the accelerator and storage system is shown in Figure 2.1. In the electron gun. laser light is used to knock electrons off the surface of a semiconductor to produce two bunches. The two bunches are accelerated to approximately 1 GeV before one enters the damping ring whose purpose is to reduce the dispersion in the beams. After that those electrons are accelerated in the Linac. The other bunch is diverted to collide with a tungsten target and create a positron beam. which in turn passes through the damping ring and is accelerated in the Linac. The electron and positron beam are fed into the PEP-II storage rings where they

collide at the interaction region as shown in Figure 2.2.

Before the next collision. the beams are separated horizontally by dipole magnetes called B1 located ±21cm on each side of the interaction point. The strong focusing of the beam is achieved by using quadrupole magnets. The interaction point is surrounded by a water-cooled beryllium beam pipe with an outer radius of 2.8 cm. contributing about 1.98% of a radiation length. Some focusing magnets. the beam pipe and the silicon vertex detector are assembled into a rigid support structure called the support tube. It has a diameter of roughly 43 cm. and contributes about 0.5% of a radiation length.

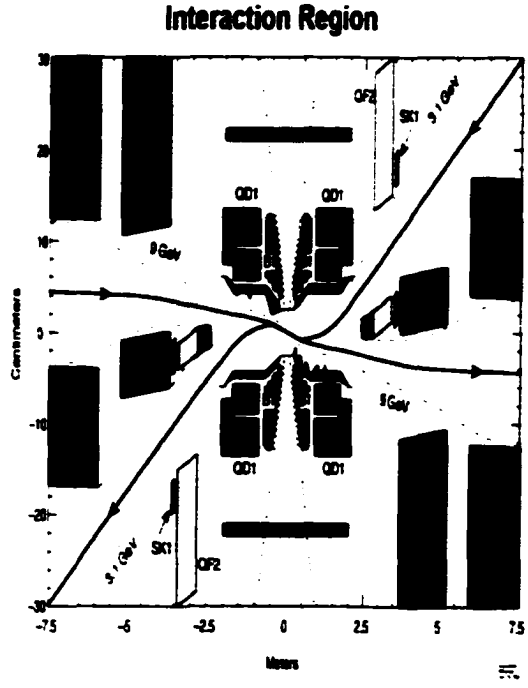

Figure 2.2: The interaction region.

The high luminosity of the machine has been achieved by using high beam currents, a multi-bunching mode of operation and strong focusing of the beams.

2.2. Detector Components

The *BABAR* detector is shown in Figure 2.3. The details are given in [49] and [50]. The detector-related figures and numbers in this chapter are quoted from those two documents. The detector coordinate system is a right-handed coordinate system defined as $+z$ in the high energy beam (electron beam) direction, $+x$ in the horizontal direction and $+y$ in the vertical direction. In this document if there is no definition given, all angles labeled as θ with possible subscripts are polar angles with respect to the $+z$ direction, and all angles labeled as ϕ are azimuthal angles in $x-y$ plane. The detector consists of the following main subsystems:

- The Silicon Vertex Tracker (SVT), which has been designed to measure angles and positions of charged particles just outside the beam pipe;
- The Drift Chamber (DCH), which provides the momentum measurement for charged particles. It also supplies information for the charged particle trigger and the measurement of dE/dx for particle identification.
- The Detector of Internally Reflected Cherenkov light (DIRC), which is a device that provides information on particle type and hence separation of pions and kaons in the momentum range from about 500 MeV/c to 4.5 GeV/c, which is

the kinematic limit on π/K separation with the difference between Cherenkov angles.

- The Electromagnetic Calorimeter (EMC), which is designed to detect electro magnetic showers with excellent energy and angular resolution over the energy range from 20 MeV to 4 GeV.

- A superconducting solenoid, which provides 1.5 T magnetic field.

- The Instrumented Flux Return (IFR), which is designed to identify muons and to detect neutral hadrons.

The energy boost makes most decay particles move to the forward direction. In order to achieve good efficiency the polar angle coverage of the detector is roughly $17° < \theta_{lab} < 150°$ in the laboratory frame.

2.3. Silicon Vertex Tracker (SVT)

The Silicon Vertex Tracker has been designed as a precise vertexing detector. The mean separation between two B mesons at PEP-II is $\sim 250\ \mu m$. For the measurement of time-dependent CP-violating asymmetries, study shows the resolution on z separation of two B vertices should be better than 50% of the value of z separation. This requires the spatial resolution on each B decay vertex along z axis to be better than $\sim 80\ \mu m$. And SVT should provide a resolution at the order of $\sim 100 \mu m$ in

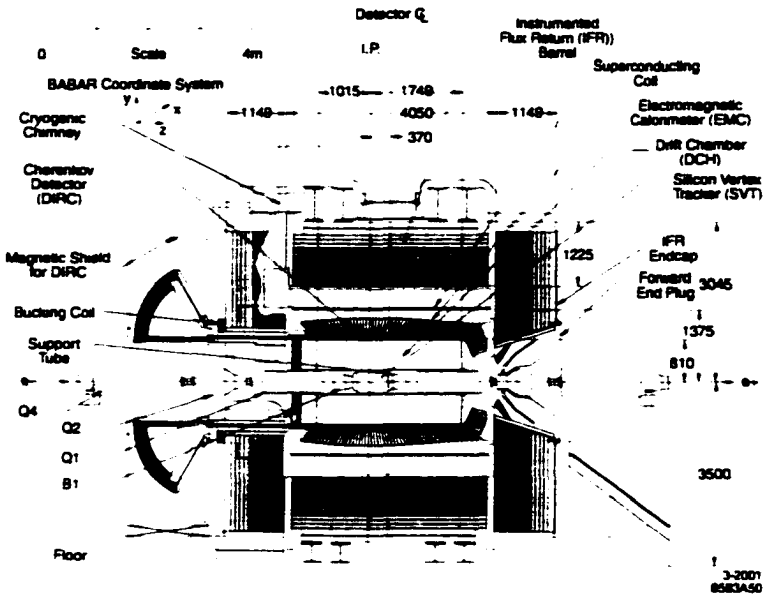

Figure 2.3: The longitudinal section of *BABAR* detector.

x-y plane for reconstructing the final states of B decays. as well as τ and charm decays. In the 1.5 T magnetic field. many tracks from B decays are short tracks with low transverse momentum p_t. The tracking efficiency for these tracks needs to be at 70% or more so SVT has been designed to provide precise reconstruction of charged particle trajectories. SVT can also provide stand-alone tracking for particles with $p_t < 0.120$ GeV. which is the minimum that can be well measured by DCH alone.

2.3.1. Layout

The SVT consists of five layers of double-sided silicon strip sensors as shown in Figure 2.4. Layers 1-3 have six modules each in a barrel arrangement. while layer 4 has 16 and layer 5 has 18 modules . Layers 4-5 form arch shapes in order to increase

solid angle coverage with less silicon (Figure 2.5).

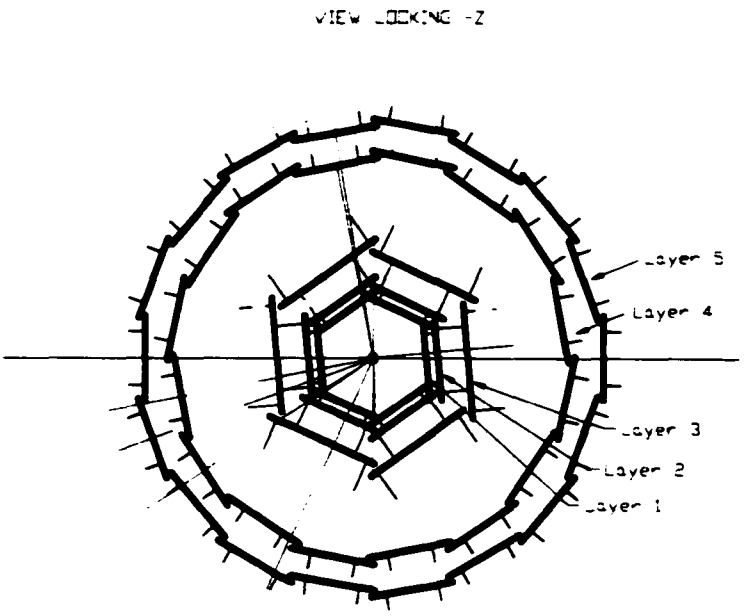

Figure 2.4: The transverse section of SVT.

The inner sides of the layers have strips which are oriented perpendicular to the beam direction to measure the z coordinates. The outer sides of the layers have strips orthogonal to the z strips to measure the ϕ coordinates. Each module is divided into forward and backward half-modules which are kept electrically isolated from one another. In total there are 340 silicon sensors with $\sim 150,000$ readout channels.

2.3.2. Readout

The signals from the strips are routed to the electronics by the fanout circuits. The front-end interface card, ATOM (A Time-Over-Threshold Machine), preamplifies.

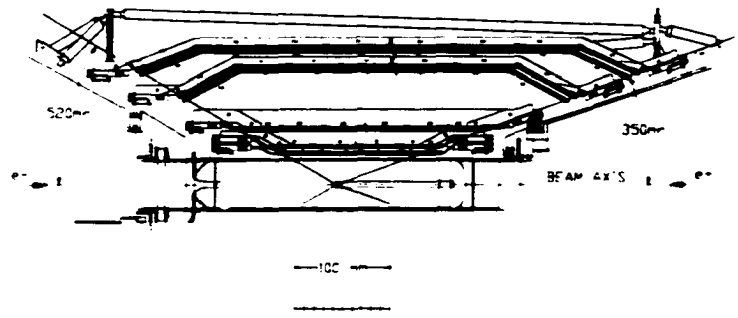

Figure 2.5: The longitudinal section of SVT.

shapes and digitizes the signals. The digitized signals are transfered from ATOM to the match cards. where they connect to the regular cables. Then the signals are multiplexed and sent to the Readout Modules (ROMs).

2.3.3. Performance

By comparing the number of associated hits to the number of tracks crossing the active area of the module. a combination of hardware and software gives a 97% of hit efficiency. The space resolution of SVT hits is determined by measuring the distance between the track trajectory and the hit using the high momentum tracks in two prong events. Figure 2.6 shows the SVT hit resolution for z and ϕ hits as a function of track incident angle for each of the five layers.

By converting the time over threshold (ToT) value to the pulse height. the ionization dE/dx can be obtained. The 60 % truncated mean dE/dx is calculated for those tracks with at least 4 sensors in the SVT and a resolution on the truncated

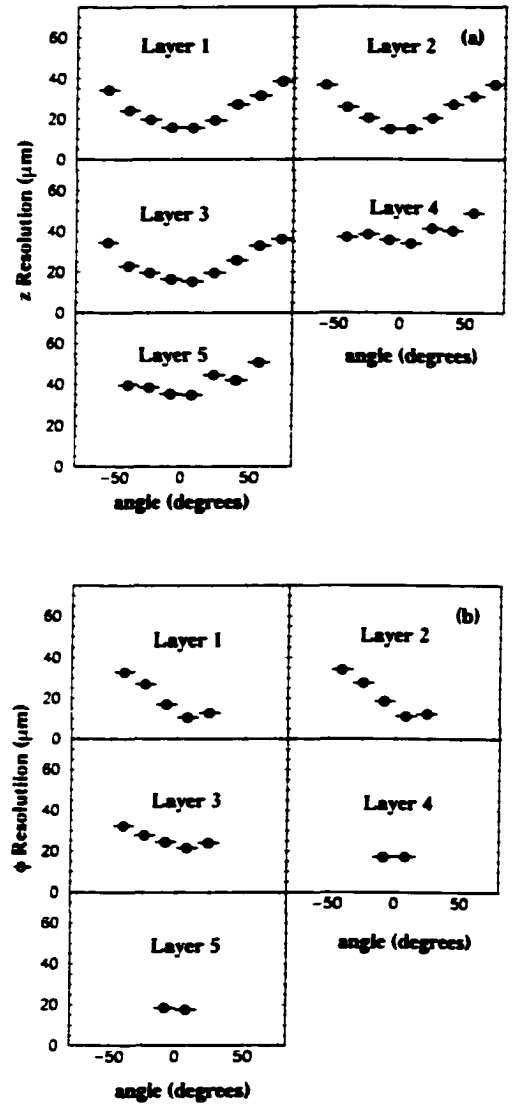

Figure 2.6: SVT hit resolution as a function of track incident angle in z and ϕ.

mean dE/dx is ~14% for the minimum-ionizing particles. The momentum region for a 2σ separation between the kaons and pions goes up to momentum of 500 MeV/c. and between kaons and protons extends beyond 1 GeV/c.

2.4. Drift Chamber (DCH)

In order to reconstruct multi-track B decay events, the DCH should provide high precision measurements of the momentum and angles of the charged particles. And it is also necessary for DCH to measure the longitudinal position for the vertex outside of SVT region as well as the transverse momentum and position. For low momentum particles DCH can be used for particle identifications by measuring dE/dx. The DCH also provides information for the charged particle trigger with a maximum time jitter of 0.5 μs, which is required by the buffer capacity limit of the front-end electronics (FEE).

2.4.1. Layout

The DCH, shown in Figure 2.7, consists of a 280 cm long cylinder with aluminum end-plates, whose inner and outer radii are 23.6 cm and 80.9 cm, respectively. All wires, including tungsten-rhenium sense wires, low-mass aluminum field wires, guard wires and clearing wires, are strung in the holes on the endplates between the inner wall and the outer shell. The DCH gas is 80:20 mixture of helium:isobutane, which

can reduce multiple scattering. Because of the boost the solid angle coverage is not forward-backward symmetric: $17° < \theta_{lab} < 152°$. The wires are organized into 40

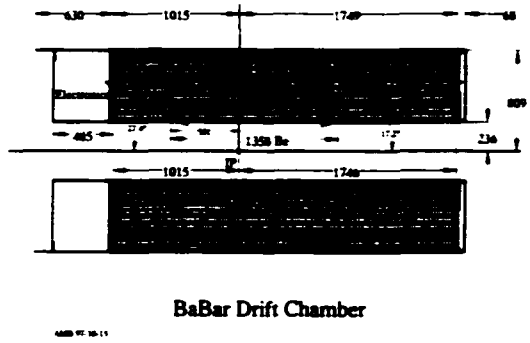

Figure 2.7: The Longitudinal section of the DCH.

layers of small hexagonal cells. subdivided into 10 superlayers in an alternating axial (A) and stereo (U,V) pattern (Figure 2.8).

2.4.2. Readout

The front-end assemblies (FEAs) hold the amplifiers. digitizers and the trigger interface electronics and are mounted on the rear endplate of the DCH. in water-cooled aluminum boxes. For each 16 sectors there are 3 FEAs. The FEAs connect to the sense wires via the service boards. The data from the readout interface in each FEA are multiplexed by the data I/O module and the trigger I/O modules. then sent to the data acquisition system. The feature extraction converts the signal to the total charge. the drift times and the status word.

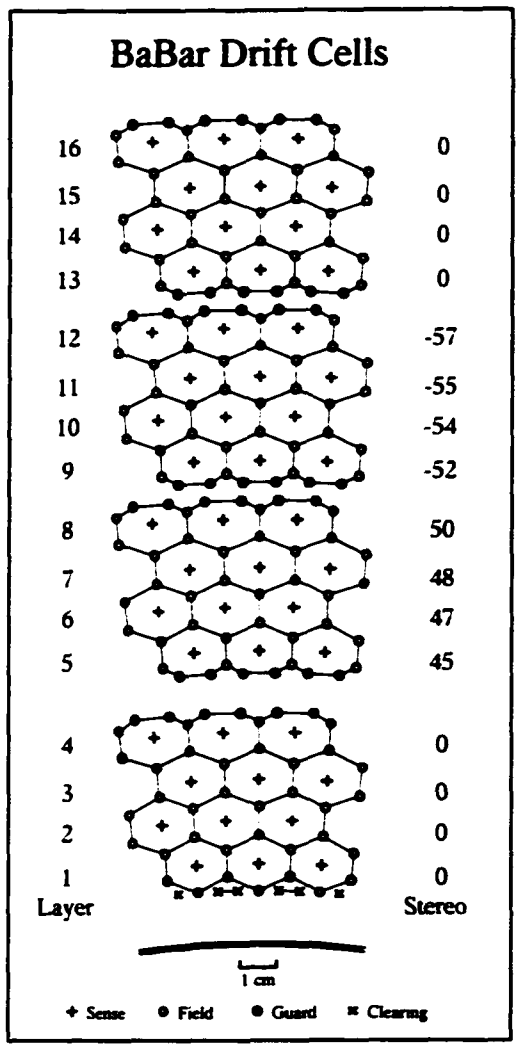

Figure 2.8: The layout of the drift cells for the 1-4th superlayers.

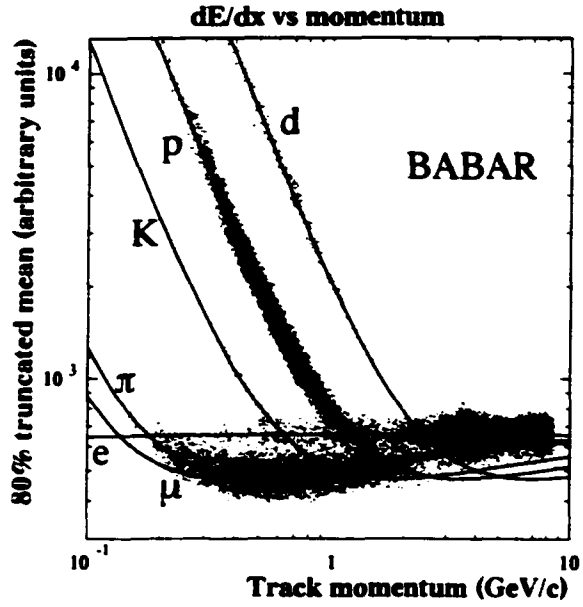

Figure 2.9: dE/dx as a function of momentum.

2.4.3. Performance

The truncated mean of the energy loss per track is measured in the DCH. Figure 2.9 shows the distribution of dE/dx as a function of track momentum.

The tracking efficiency is $98 \pm 1\%$ per track with momentum great than 200 MeV/c at the high voltage 1960 V.

By reconstructing comic ray tracks into two segments, the difference of four tracking parameters between the two segments can be measured (Figure 2.10). These differences are very sensitive to all components of tracking system because the two segments are really from one track. These plots can be used for monitoring the performance of tracking system.

From the cosmic data, the resolution on the transverse momentum can be ob-

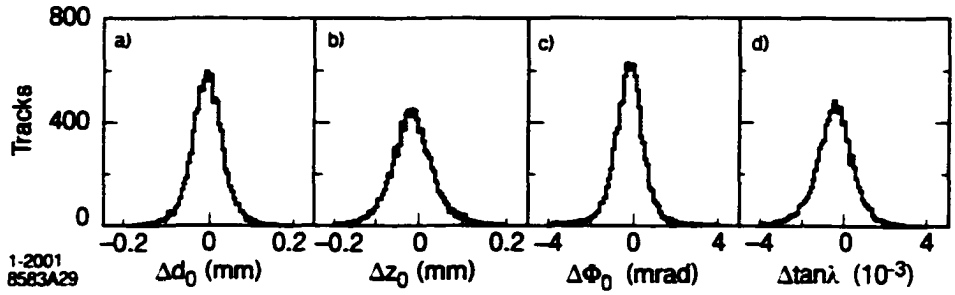

Figure 2.10: The difference of 4 tracking parameters.

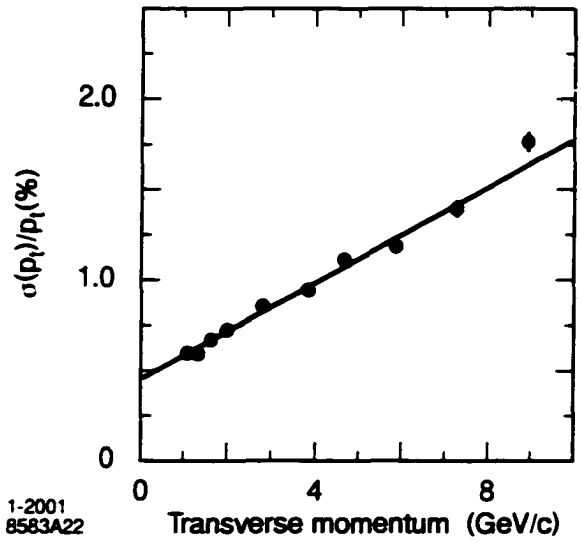

Figure 2.11: The p_t resolution.

tained: $\sigma_{p_t}/p_t = (0.13 \pm 0.01)\% p_t + (0.45 \pm 0.03)\%$.

2.5. Detector for Internally Reflected Cherenkov Light (DIRC)

A novel particle identification (PID) device at *BABAR*. Detector for Internally Reflected Cherenkov light (DIRC). can provide π/K separation of $\sim 4\sigma$ or greater, for all tracks from B meson decays within the momentum range from the pion Cherenkov threshold up to 4.5 GeV/c. This is desirable for physics analyses such as the kaon

tagging procedure used to decide B meson flavor. in which the momentum of kaon is 1~2 GeV/c. and the rare two-body decay $B^0 \to \pi^+\pi^-$ vs. $B^0 \to K^-\pi^+$. where the momentum of kaon/pion can be up to 4 GeV/c.

A schematic in Figure 2.12 shows the principle of the light production. transport and imaging in the DIRC. In a medium with index of refraction n (fused silica quartz with $n = 1.473$ for DIRC). if a particle moves with the speed v which is faster than the speed of the light in the medium. a cone of Cherenkov radiation will be generated with a half-opening angle $\theta_C = 1/3n$ with respect to the particle direction. If the index of refraction of the medium is larger than that of the surrounding medium. most of the light will be internally reflected at and above a critical angle of incidence. Then the light will travel in the medium by reflecting.

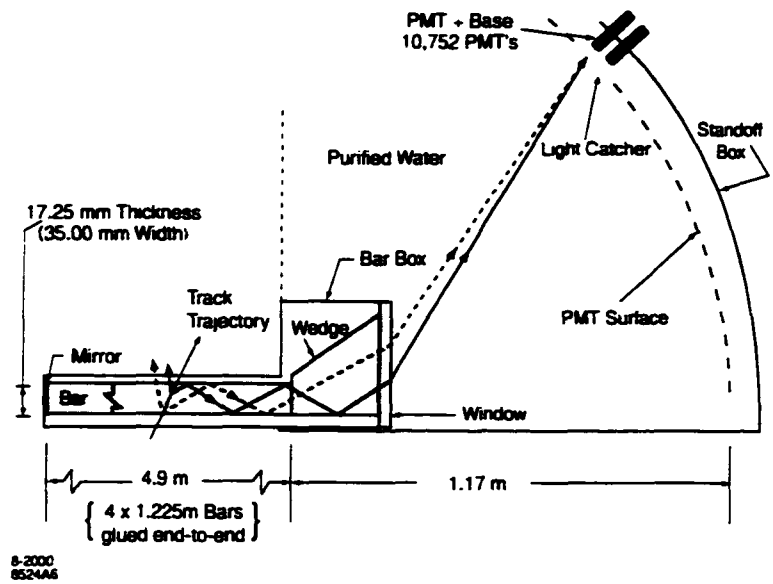

Figure 2.12: The DIRC bar and imaging region.

2.5.1. Layout

DIRC consists of 144 bars of synthetic quartz arranged in a 12-sided polygonal barrel shape. Each bar box contains 12 bars. Each bar has the dimension of 1.7 cm thick by 3.5 cm wide and are 4.9 m long. The quartz extends through the magnet flux return in the backward direction in order to keep the forward endcap of the calorimeter without gap.

The major mechanical elements of the DIRC are shown in Figure 2.13.

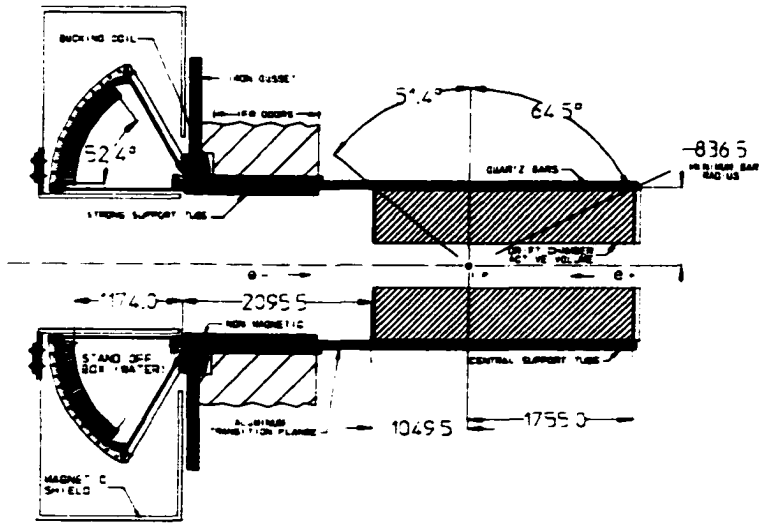

Figure 2.13: The DIRC system geometry.

2.5.2. Readout

The Cherenkov image expands in a tank of purified water whose refractive index is close to that of the quartz bars. At the far end of the tank is an array of photomultiplier tubes (PMTs) lying on the surface which is approximately toroidal so as

to make all photon pathlength equal to 1.2 m. The backward end of each bar has a small trapezoidal piece of quartz glued to it. This allows for a reduction in the number of PMTs by reflecting photons with large angles in the radial direction back into the detection array.

2.5.3. Performance

The measured single photon resolution is 1.7 ns. which is close to the expected value of the single-photon resolution of PMTs. 1.5ns. The efficiency for kaon identification and the probability to misidentify a pion are shown in Figure 2.14 by using $D^0 \rightarrow K^-\pi^+$ control sample. The average kaon selection efficiency is (96.2±0.2)% and the pion mis-identification probability is (2.1±0.1)%.

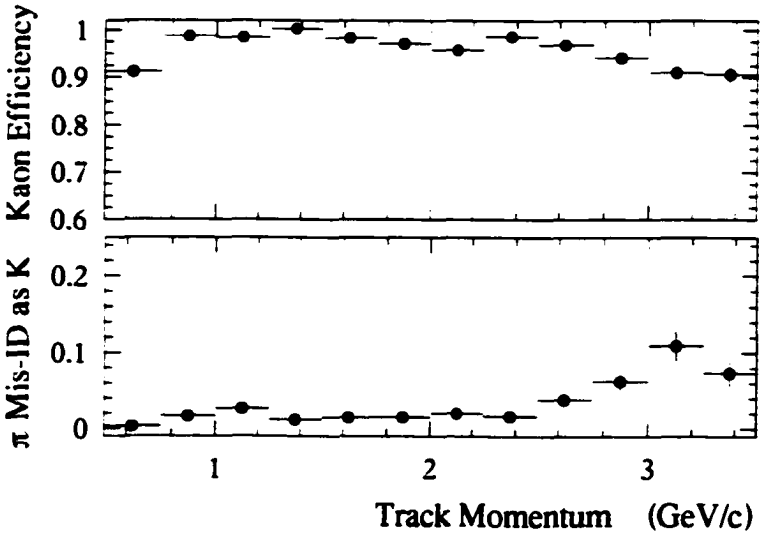

Figure 2.14: The kaon efficiency and pion mis-identification probability.

2.6. Electromagnetic Calorimeter(EMC)

The Electromagnetic Calorimeter (EMC) has been designed to detect photons and to differentiate electrons and positions from other charged particles. It should provide high efficiency for photons in a wide energy range, from the low bound due to B decays with multiple π^0 or η mesons, to the upper bound due to the QED processes used in calibration and luminosity such as $e^+e^- \rightarrow e^+e^-(\gamma)$, $e^+e^- \rightarrow \gamma\gamma$. The mass resolution is dominated by the energy resolution for π^0s with energy below 2 GeV but by the angular resolution for π^0s with energy above 2 GeV. The crucial requirement on resolution comes from some rare B decays with π^0s, which require the fractional resolution on energy be at $1 \sim 2\%$ level. The EMC is capable of these measurements and has good energy and angular resolution over the range from 20 MeV to 9 GeV.

2.6.1. Layout

EMC has two main sections (Figure 2.15), the barrel and the forward endcap. There are 5,760 CsI crystals in the barrel region, arranged in 48 θ rows, each row with 120 identical crystals around ϕ. The angular coverage of the barrel in the lab frame is $-0.80 < cos\theta_{lab} < 0.89$. The endcap is a conic shape with a 22.7^0 tilted angle with respect to the vertical. The 820 endcap crystals are arranged in 8 rings in θ and grouped into 20 modules of 41 crystals each in ϕ. The endcap covers $0.89 < cos\theta_{lab} < 0.97$ in the lab frame.

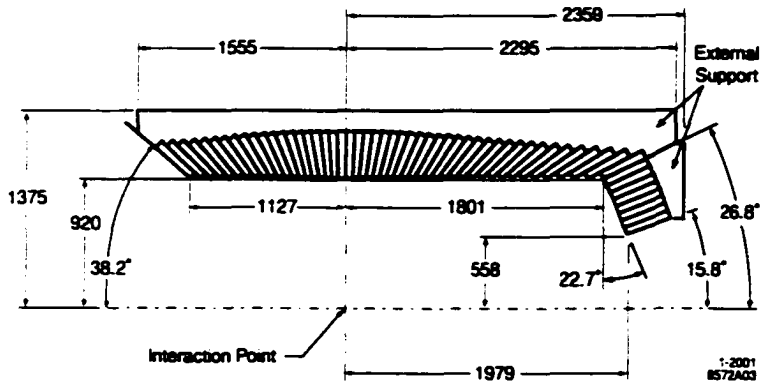

Figure 2.15: The top half of the longitudinal section of the EMC.

2.6.2. Readout

The scintillation light produced in each crystal is detected by two $1cm \times 2cm$ photodiodes glued to its back face. The output is sent to the ROM after preamplifying, postamplifying and digitizing.

2.6.3. Performance

The photons in different processes(Figure 2.16) are used to measure the energy resolution. The fit to the energy dependence gives the result:

$$\frac{\sigma_E}{E} = \frac{(2.32 \pm 0.30)}{\sqrt[4]{E(GeV)}} \oplus (1.85 \pm 0.12)\%. \tag{2.1}$$

The result is consistent with the MC simulation and slightly worse than the optimistic estimates.

The angular resolution is based on the π^0 and η analysis:

$$\sigma_\theta = \sigma_\phi = (\frac{3.87 \pm 0.07}{\sqrt{E(GeV)}} + 0.00 \pm 0.04) \quad mrad. \tag{2.2}$$

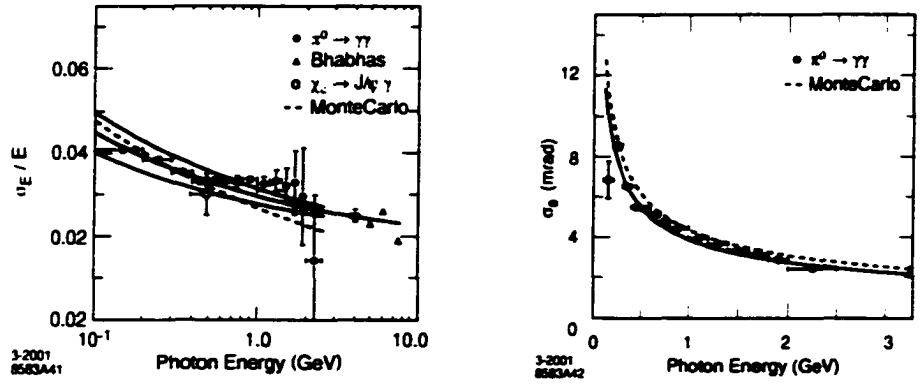

Figure 2.16: The energy resolution and the angular resolution of the photons.

The efficiency for electron identification and the pion miss-identification are measured with $e^+e^- \rightarrow e^+e^-e^+e^-$ events and charged pions from K^0_S decay.

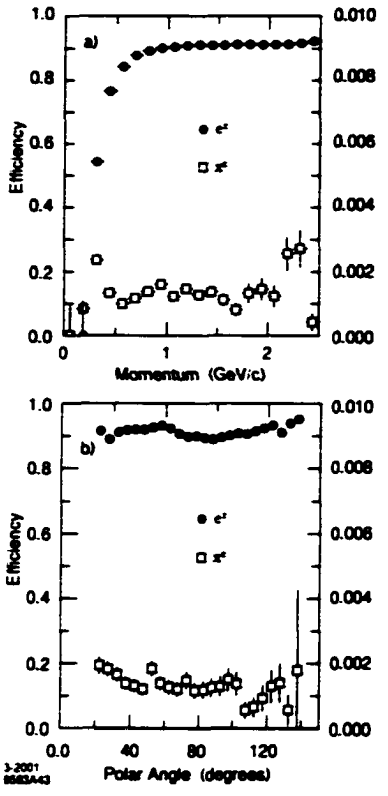

Figure 2.17: The electron selection efficiency and the pion mis-identification efficiency.

2.7. The Instrumented Flux Return (IFR)

The Instrumented Flux Return (IFR) is dedicated to identifying muons and neutral hadrons such as K_L^0 with high efficiency and good purity over a wide range of momenta and angles. Muons are used in lepton tagging for the flavor estimation of neutral B mesons. K_L^0 appears in CP eigenstates of B decays.

2.7.1. Layout

The three parts of the IFR. the barrel. the forward endcap and the backward endcap. are shown in Figure 2.18. They are divided into sextants. IFR uses Resistive Plate Chambers (RPCs) as the active detectors. and the steel flux return as muon filter and hadron absorber. The RPCs are located between the layers of the steel. There are 19 layers of RPC in the barrel. 18 layers in the endcaps and 2 layers called the inner RPCs between the EMC and the magnet.

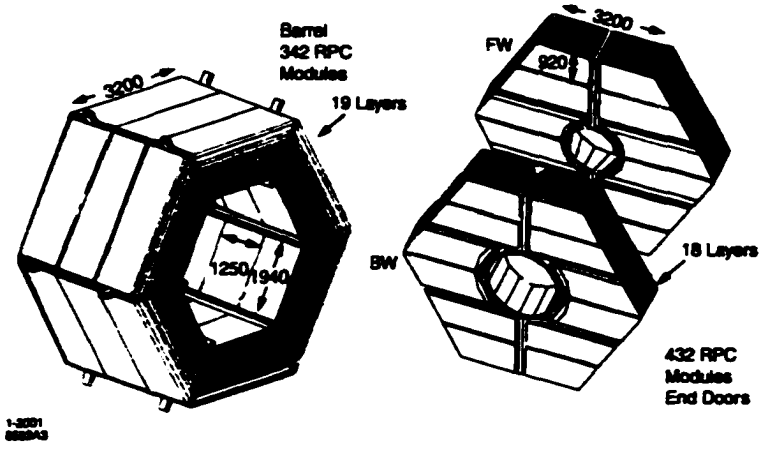

Figure 2.18: IFR. barrel sectors and forward. backward endcap.

2.7.2. Readout

The readout strips on one side of RPCs are orthogonal to those on the other side so that the chamber can provide three-dimensional position information. The signals from each sixteen strips are sent to a front-end card (FEC). which shapes and discriminates them. The FEC output is transfered to the IFR front-end crates.

which hold data handling cards, trigger cards and crate controller cards. The data handling cards provide hit buffering, time information, and calibration, and the crate controller cards forward the data to the ROM.

2.7.3. Performance

With the control sample $ee\mu\mu$ events and $\mu\mu\gamma$ events, a 90% detection efficiency for muon has been obtained in the momentum range 1.5 GeV/c < p < 3.0GeV/c. And the pion misidentification probability is 6 – 8% (Figure 2.19). Combined with EMC information, K_L^0 detection efficiency varies between 20% and 40% in the momentum range from 1 GeV/c to 4 GeV/c.

2.8. Trigger

The trigger system selects interesting events at the rate ~120Hz from the total beam crossing rate ~238MHz at design luminosity. For an event with at least one track or at least one EMC cluster[1] the background rate is ~20kHz. The trigger system should provide more than 99% efficiency for $B\bar{B}$ events, at least 95% efficiency for continuum[2] events and 90-95% for τ events, but introduce less than 1% dead time.

The trigger system includes the Level 1 trigger, which reduces the output rate to less than 2kHz in hardware, and Level 3 trigger, which subsequently cuts the rate to

[1] A cluster is a contiguous area of crystals with energy deposited greater than the threshold.
[2] Continuum means the final states from $e^+e^- \rightarrow u\bar{u}, d\bar{d}, s\bar{s}, c\bar{c}$.

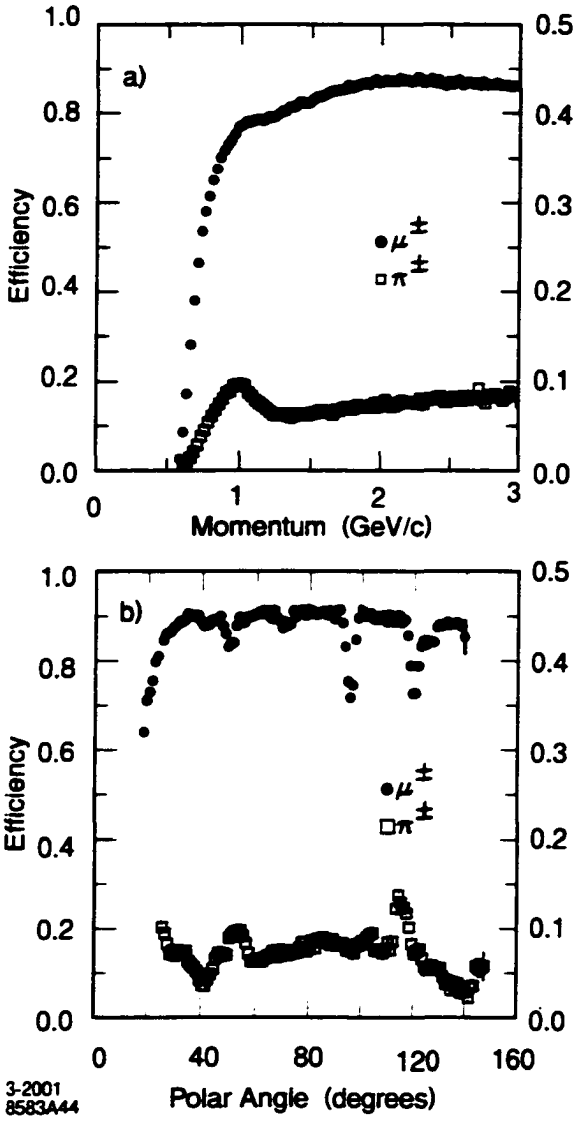

Figure 2.19: Muon efficiency (left scale) and pion mis-identification efficiency (right scale).

120Hz in software. Software filters, described in the next chapter, reduce this rate to about ~ 42 Hz, which are mostly events of physics interest.

2.8.1. L1 trigger

Level 1 trigger uses three subdetector hardware triggers together to make decisions. Drift Chamber Trigger (DCT), Calorimeter Trigger (EMT) and IFR Trigger (IFT). The DCT algorithms are deployed in three steps. The Track Segment Finder (TSF) finds the track segments based on one bit for each of the 7104 DCH cells. Then the Binary Link Tracker (BLT) is used to link segments to complete tracks. The transverse momentum discriminator (PTD) is run to find the tracks with large p_t. The output of DCT is three *primitives* in terms of 16-bit ϕ maps, called B, A and A' corresponding to increasing p_t thresholds. The definitions of all primitives are explained in Table 2.1. In the EMT 10 Trigger Processor Boards (TPBs), each sum the energy from 40 ϕ sectors in the full range of θ and compare the energy to the thresholds to make primitives. The output is five primitives in terms of 10-bit ϕ maps, called M, G, E, X and Y corresponding to increasing energy thresholds. For IFT, the 3-bit trigger word, U, is generated from the trigger objects in 10 sectors to provide rough indication of muons.

The primitives from the subdetectors are sent to the global trigger (GLT) to form the 24 trigger lines based on the logical combinations of the primitives. The

Table 2.1: Trigger primitives.

	Definition	Builder	No. of bits	Threshold
B	Short track reaching DCH superlayer 5	BLT	16	120 MeV/c
A	Long track reaching DCH superlayer 10	BLT	16	180 MeV/c
A′	High p_T track	PTD	16	800 MeV/c
M	All-θ Minimum-ionizing energy	TPB	20	100 MeV
G	All-θ intermediate energy	TPB	20	250 MeV
E	All-θ high energy	TPB	20	700 MeV
X	Forward endcap Minimum-ionizing	TPB	20	100 MeV
Y	Backward barrel high energy	TPB	10	1 GeV
1U	$\geq$2 μ topologies other than U=5-7			
2U	1 μ in backward endcap			
3U	1 μ in forward endcap			
4U	1 μ in barrel			
5U	2 back-back μ's in barrel + 1 forward μ			
6U	1 μ in barrel + 1 forward μ			
7U	2 back-back μ's in barrel			

trigger efficiencies for physics events based on some selected trigger lines are shown in Table 2.2. The * superscript in the trigger line means that two primitives are required to be back-to-back in ϕ. As a trigger line example. M* $\geq$ 1 & A$\geq$ 1 & A′ $\geq$ 1. requires at least one long track (A). at least one high p_t track (A′) and at least two minimum-ionizing energy clusters that are back-to-back (M*).

Table 2.2: Level 1 Trigger efficiencies (%) and rates (Hz) at a luminosity of 2.2 × $10^{33}\,cm^{-2}s^{-1}$. The pure DCT lines, the pure EMT lines and the combined lines are separated into three blocks.

Level 1 Trigger	$\epsilon_{B\bar{B}}$	$\epsilon_{c\bar{c}}$	ϵ_{uds}	ϵ_{ee}	$\epsilon_{\mu\mu}$	$\epsilon_{\tau\tau}$	Rate
A≥3 & B* ≥1	97.1	88.9	81.1	–	–	17.7	180
A≥1 & B* ≥1 & A′ ≥1	95.0	89.2	85.2	98.6	99.1	79.9	410
Combined DCT (ORed)	99.1	95.3	90.6	98.9	99.1	80.6	560
M≥3 & M* ≥1	99.7	98.5	94.7	–	–	53.7	160
EM* ≥1	71.4	77.1	79.5	97.8	–	65.8	150
Combined EMT (ORed)	99.8	98.8	95.6	99.2	–	77.6	340
B≥3 & A≥2 & M≥2	99.4	94.8	87.8	–	–	19.7	170
M* ≥1 & A≥1 & A′ ≥1	95.1	90.1	87.0	97.8	95.9	78.2	250
E≥1 & B≥2 & A≥1	72.1	77.7	79.2	99.3	–	72.8	140
M* ≥1 & U≥5 (μ-pair)	–	–	–	–	60.3	–	70
Combined Level 1 triggers	>99.9	99.9	98.2	>99.9	99.6	94.5	970

2.8.2. L3 trigger

Level 3 trigger is a software filter which takes the L1 output and the fast control (FCT) scalers as the input. The first step is to define at least one L3 Input line for each L1 output. Then L3 scripts are used to select events, finally the L3 output lines are defined. The whole process is to refine the L1 output and reject more background.

2.9. Online System

The online system performs the data acquisition from the front-end electronics, event building and data loging. It also includes the control and monitoring of the

Table 2.3: L3 trigger efficiency (%) based on Monte Carlo simulation.

L3 Trigger	$\epsilon_{B\bar{B}}$	$\epsilon_{c\bar{c}}$	ϵ_{uds}	$\epsilon_{\tau\tau}$
1 track filter	89.9	89.2	88.2	94.1
2 track filter	98.9	96.1	93.2	87.6
Combined DCH filters	99.4	97.1	95.4	95.5
2 cluster filter	25.8	39.2	48.7	34.3
4 cluster filter	93.5	87.4	85.5	37.8
Combined EMC filters	93.5	87.4	85.6	46.3
Combined DCH+EMC filters	>99.9	99.0	97.6	97.3
Combined L1+L3	>99.9	98.9	95.8	92.0

detectors and data acquisition. monitoring of data quality and the online calibration. The design capability can process the input from L1 accept rate up to 2 kHz and the maximum L3 output rate at 120 Hz while adding less than 3% dead time.

A schematic configuration for the system hardware is shown in Figure 2.20. There are 157 custom VME ROMs(Readout Module) located on 23 crates that obtain data from the FEE though 1.2Gbps optical fibers. then send the data to 32 SUN Ultra5 computers to build events. via a network switch connected with 100Mbps Ethernet. L3 trigger software on 32 machines selects events then writes to the storage via the log server. which is a SUN Enterprise450 computer. Several other servers are available for online databases. online software and operation display. There are another fifteen VME crates that hold the data acquisition hardware for the detector control subsystem.

The following main subsystems are deployed for the online system:

ODF(Online Data Flow). which receives L1 trigger output. then communicates the detector FEE to get the data and assemble them to events:

OEP(Online Event Processing). which performs L3 triggering. DQM(Data Quality Monitoring). the final Calibrations:

Logging Manager. which receives events from OEP then writes them to disks for Prompt Reconstruction later:

Detector Control. which controls and monitors the conditions of the detector systems:

Run Control. which coordinates all other systems.

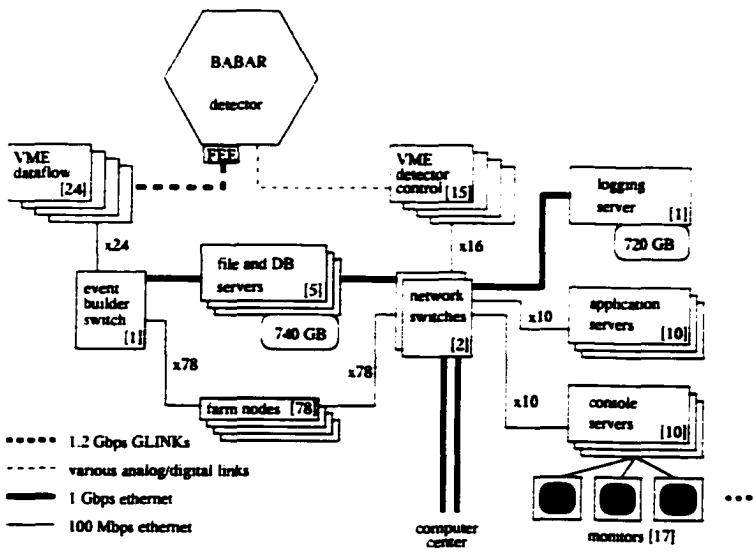

Figure 2.20: the *BABAR* on-line system.

Chapter 3

Data Description

3.1. *BABAR* Data

Both Run1 and Run2 data are used for the analysis. This refers to all data taken from Feb. 4. 2000 to Dec. 1. 2001. The total number of runs[1] is 6130 with the run number range from 11334 to 24419. The integrated luminosity of on-peak data. which were taken on the $\Upsilon(4S)$ resonance. is 50.9 fb^{-1}. Table 3.1 shows the production cross sections of the most important physics processes. The total number of $B\overline{B}$ events ($N_{B\bar{B}}$) is $(55.5 \pm 0.9) \times 10^6$ [51]. The integrated luminosity of off-peak data. which were taken slightly below the $\Upsilon(4S)$ resonance. is 6.3 fb^{-1}.

Only those runs that were marked as *good* by Data Quality Monitoring (DQM) were used. The good quality requires that all sub detector hardware be in reliable

[1]A run is a small data set taken in a short time period. normally less than two hours. Each run has an integer serial number. its so-called run number.

Table 3.1: The cross sections for possible productions on $\Upsilon(4S)$ resonance.

Final State	Cross section (nb)
$b\bar{b}$	1.05
$c\bar{c}$	1.30
$s\bar{s}$	0.35
$u\bar{u}$	1.39
$d\bar{d}$	0.35
$\tau^+\tau^-$	0.94
$\mu^+\mu^-$	1.16
e^+e^-	~40

status. the specific performance checking for each subdetector show no problems. there should be no luminosity inconsistency. and the data be processed without problem.

The data were divided into small sets according to the internal consistency. denoted by year. *block*. *subset* and *chunk*[2]. A block is a large set of data with common basic quality. Different blocks usually have some different hardware configuration like DCH high voltage. which was set at 1900 V and 1960 V during Run1 period. 1930 V during Run2 period (Table 3.2). Different high voltages cause different tracking efficiencies. mass resolutions and background ratios. etc. When an analysis uses different data blocks. all possible discrepancies need to be considered.

A subset is a set of data which are more internally consistent. The data in each subset have been processed with the same software release. and the SVT local align-

[2]BABAR jargons for data set convention.

Table 3.2: Data blocks divided by DCH high voltage.

Block	DCH HV	*Luminosity*(fb^{-1})
1	1900V	10.7
2	1960V	9.6
3	1930V	31.3

ment constants. The SVT local alignment is a procedure to determine the relative positions of the 340 silicon sensors. The six local parameters of each sensor are obtained by minimizing a χ^2 built with the hit residuals from muon tracks ($\mu^+\mu^-$ events or cosmic rays) and the survey information during the assembly. A different SVT local alignment (Table 3.3) is needed after magnet quenches or detector access. It has important impact on tracking parameter resolutions and vertexing, which are critical for physics analyses, especially the lifetime measurements.

Table 3.3: The SVT local alignment sets.

SVT local alignment set	Run range
A	9731-10681
B	10682-11330
C	11331-12708
D	12709-14542
E	14543-17106
N	17301-

All data used in this document were reprocessed with the improved local alignment

algorithm in set N.

A chunk of data is a further refinement of a subset, based on on-peak or off-peak running.

3.2. Monte Carlo Generation

Two categories of events were generated: background events, which include uds, $c\bar{c}$ and generic $B\bar{B}$; and signal events for each mode. When the background events were generated inclusively, all possible decay modes were included according to branching fractions and decay modes from Particle Data Group (PDG) [19]. For the signal events, only the final states that will be searched for were generated. Signal MC events are used to determined the efficiency for detecting the signal. For all modes with a J/ψ, only $J/\psi \to e^+e^-$ and $J/\psi \to \mu^+\mu^-$ were generated with 50% ratio each and all hadronic J/ψ decays were omitted. A similar method was applied to K^0_S, ρ, η, η' decays.

The decay mechanism is not well understood for the decays $B \to J/\psi\rho K$ and $B^0 \to J/\psi\rho$ so no specific Dalitz distributions and amplitudes were used. When $B \to J/\psi\rho K$ modes were generated, simple three-body phase space was assumed. For $B^0 \to J/\psi\rho$ two-body phase space was assumed. But the helicity amplitude matrix elements were used for vector-pseudoscalar modes $B \to J/\psi\eta$ and $B \to J/\psi\eta'$.

For the background study in the rare decay analysis, the inclusive J/ψ sample

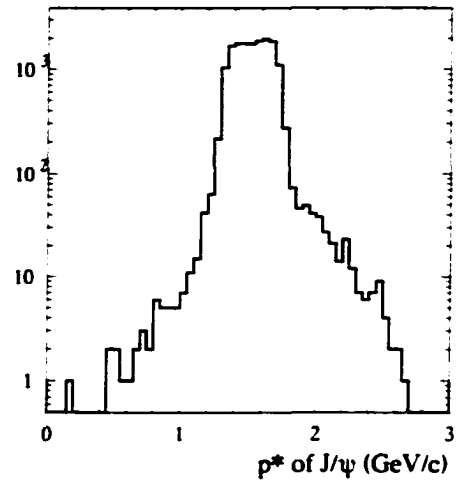

Figure 3.1: p* of J/ψ in $B^0 \rightarrow J/\psi\phi$ decays.

(inclusive $B \rightarrow J/\psi + X$ events) is very useful. It was generated with the $B\overline{B}$ generators, but a filter was applied so only the events with a J/ψ were then fully simulated and reconstructed. This is effective to get a large sample comparable to the real data luminosity but with less computing consumption. The sample was generated in two categories: one requires the momentum of the J/ψ in center-of-mass frame, p^*, be greater than 1.3 GeV/c; the other sample does not have this requirement. For most analyses of two body B decays at *BABAR*, the p^* of J/ψ is greater than 1.3 GeV/c and the first sample is used. In this document the latter one was used because in these modes the p^* of J/ψ may be less than 1.3GeV/c; see Figures 3.1 and 3.2.

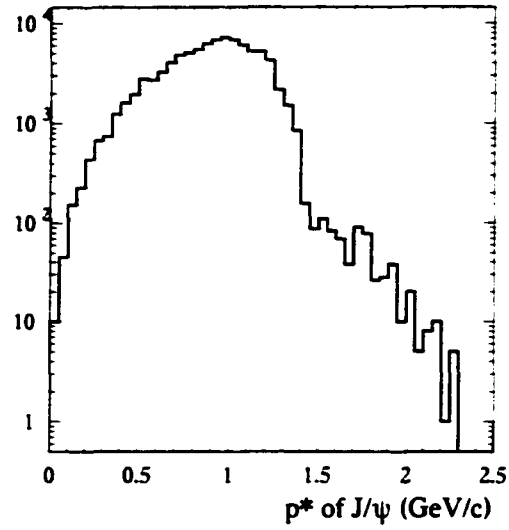

Figure 3.2: p* of J/ψ in $B^0 \to J/\psi\phi K^0_S$ decays.

Monte Carlo (MC) events were produced in two cycles: Simulation Production cycle 3 (SP3) and cycle 4 (SP4). SP3 is based on GEANT3 and SP4 is based on GEANT4 [52]. The simulation procedure involves three steps: the physics process generation: the detector simulation: and the reconstruction. In order to simulate the real *BABAR* running status. the different machine background levels and the various detector conditions were considered for the different time periods. The signal events were generated in SP4. but the background events were generated in both SP3 and SP4. The number of events and correspondingly equivalent luminosity are listed in Table 3.4 and Table 3.5.

Table 3.4: Signal SP4 MC events.

Signal mode	Cycle	No. of events
$B \to J/\psi\eta, \eta \to \gamma\gamma$	SP4	19.000
$B \to J/\psi\eta, \eta \to \pi^+\pi^-\pi^0$	SP4	19.000
$B \to J/\psi\eta'$	SP4	17.000
$B^0 \to J/\psi\omega$	SP4	23.000
$B^+ \to J/\psi\omega K^+$	SP4	23.000
$B^0 \to J/\psi\omega K^0_S$	SP4	20.000

Table 3.5: SP3/SP4 MC events for background.

Type	No. of events	Luminosity (fb^{-1})
uds	18.191.830	8.71
$c\bar{c}$	12.096.226	9.30
$B^0\overline{B}^0$	3.675.361	7.00
B^+B^-	4.457.402	8.49
Inclusive J/ψ (SP3)	243.000	84.5
Inclusive J/ψ (SP4)	220.000	76.5

3.3. Database

BABAR supports two main database systems. Objectivity database and KANGA. The main database is an object oriented database based on the commercial software. Objectivity [53]. The second one. KANGA. is based on ROOT [54]. which is an object oriented framework for data analysis developed at CERN.

3.3.1. Objectivity

The Objectivity database system consists of three main domains. the *configuration database*. the *condition database*. and the *event store*. The user applications access the event store by the *event collections*. which are the references to a set of events in the event store. generally a run.

The configuration database creates the associations of the configuration information data with a single *configuration key* for all subsystems of *BABAR*. The key can be used to retrieve the corresponding configuration information.

The conditions database includes the information of running status of *BABAR*. such as detector calibrations. electronics calibrations and detector alignments. It consists of the full description of the experiment variation with the time and component.

The event store is the core part of the database. Both performance and capability are critical. On one side. fast access to the massive data should be possible for users: on the other side. the database should be be capable of all kinds complicated queries. Based on these requirements. the whole event information are encapsulated into different levels according to the possible query frequency (Figure 3.3). Technically. an event is described by hierarchical objects based on different *event headers*. This header contains references to multiple low level objects. each corresponding to a particular processing level. For each level a header at this level includes the references

to the further low level objects.

The different levels that can be associated with each event are the following:

- Event header (Hdr). The event header consists of references to the further information.

- Simulated data (Sim). This is only for MC simulation events. It includes the Raw data and additionally the truth information such as the decay trees, the true position and momentum, etc (Tru).

- Raw data (Raw). This is the converted output of the online system with the database format, which have been processed by the front-end electronics and possibly by the OEP. The *xtc* file is the output data from the FEE ROMs that was formated by the feature extraction code into the form of an extended tagged container. For further processing, xtc files are converted into *digi* format, which is the data structure that can be accessed by the reconstruction code.

- Reconstructed data (Rec). This is the data after full reconstruction. It contains track information, cluster information, etc.

- Event summary data (Esd). This is the compressed Rec data. It corresponds to the DST data conventionally in database systems. At this level there still are enough information to do event display, redo reconstruction, etc.

- Analysis object data (Aod). This is end-user data, which is mainly used for

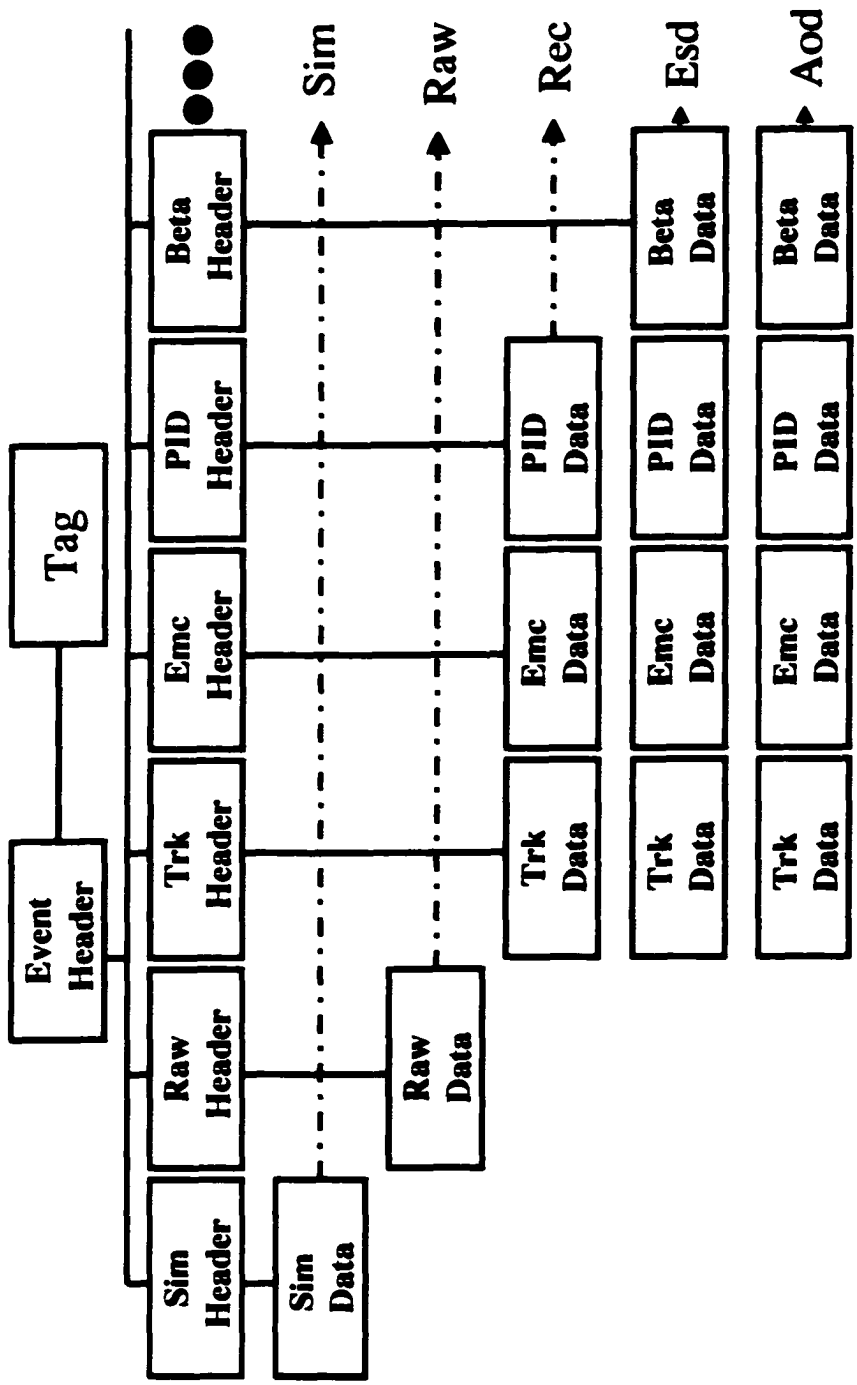

Figure 3.3: The database structure.

final physics analysis and is called the Micro database at *BABAR*. For most physics analyses, the Micro information is enough. But for some studies like tracking efficiency, it is necessary to start from xtc files.

- Tag data (Tag). This is an event summary designed to allow for fast but simple queries on a small subset of the attributes of the children objects without having to access all objects directly. Event level tags are also produced. Extremely high performance queries can make rough selections based on the event tags, allowing the complicated analyses with low performance to run on just a small subset of the events. This strategy can result in dramatic performance gains.

A very rough estimate of the sizes of this information is shown in Table 3.6.

Table 3.6: The sizes of different levels of Objectivity data per event.

Part	Size
Hdr	~50 Bytes
Sim	-
Raw	~50 KBytes
Rec	~100 KBytes
Esd	~10 KBytes
Aod	~1 KBytes
Tag	~100 Bytes

3.3.2. KANGA

KANGA is an acronym for "Kinder ANd Gentler Analysis". It is a database system based on ROOT. It was designed as an alternative solution with reasonable functionality for physics analyses to access Micro database using the standard framework, but without the overhead and reduced speed of Objectivity. It is transparent for user applications to access the event store, and compatible with the analysis software framework available. It can run on all supported operating systems. It runs fast and can be easily distributed to remote sites. But the KANGA database provides only Micro information, no Raw and Rec part at all.

A similar ROOT conditions database was developed. It is a flat file that contains the beam conditions and the DCH dE/dx Bethe-Bloch parameterization [55], etc.

To mimic the objectivity database, the event store is organized in a split mode such as Aod, Tag, etc. The data is written with ROOT compression level 2.

The MC truth information can be accessed in a KANGA file for generated events, but the matching between the true information and the reconstructed information is not persistent as in the Objectivity database. Rather a χ^2 based associator was used.

The size of a physics event (`isPhysicsEvents` in the next section) in KANGA format is $\sim$ 2 kBytes on average, including the Tag component. It is similar to the size of the corresponding part in Objectivity database, Aod. The size of a multi-hadron event is at the order of 4 kBytes, while the size of a $\mu^+\mu^-$ event, is 0.8 kByte. For

MC data. the truth information adds 4 to 5 kBytes for a hadronic event.

3.4. Data Processing

Not all 120Hz output of L3 trigger are fully reconstructed. Before the full reconstruction, a selection was applied by two levels of filters: `DigiFilter` and `BGFilter`. `DigiFilter` uses the digi information to make selections and requires no reconstruction. It is just based on the L1 trigger and L3 trigger output, so it can be run after the conversion from xtc to digi. The main purpose is to reject calibration events such as Bhabha events.

The tag bits that are defined in DigiFilter are shown in Table 3.7.

Table 3.7: Tag bits in `DigiFilter`.

Tag Bit	Description
`DigiFL1Prescale`	Prescaled L1 output
`DigiFL3Prescale`	Prescaled L3 output
`DigiFL3OutDchEmcPreVetoPrescale`	L3 output before Bhabha vetoing
`DigiFBhabhaFlat`	Flattened Bhabha events
`DigiFRadiativeBhabha`	Radiative Bhabha events
`DigiFRandomPrescale`	Prescaled random trigger events

A partial reconstruction was run for those events that pass the `DigiFilter`. During the partial reconstruction, only drift chamber was used to find tracks, and the

calorimeter reconstructions just found the clusters and did not split them to bumps[3]. A simple track-cluster matching algorithm was applied afterward. Based on these tracks and clusters, several selectors together called **BGFilter**, were used to classify all possible physics events such as multihadron, τ events or two-prong events, etc. If an event fails the **BGFilter**, it only can be recovered from the xtc files. The **BGFilter** tag bits are listed in Table 3.8. The overall offline selection is illustrated in Figure 3.4.

Table 3.8: Tag bits in **BGFilter**.

Tag Bit	Description
BGFMultiHadron	Multi-hadron events
BGFNeutralHadron	Hadronic events with a neutral mode
BGFTau	$e^+e^- \to \tau^+\tau^-$
BGFMuMu	$e^+e^- \to \mu^+\mu^-$
BGFTwoProng	Two-prong events
BGFGammaGamma	Two-photon events $e^+e^- \to \gamma\gamma$
BGFRadBhabha	Radiative Bhabha events
BGFPhiGamma	$e^+e^- \to \phi\gamma$
BGFAllNeutralTwoPhoton	Events with neutral modes only
BGFVirtualComptonScattering	Virtual Compton scattering events

About 35% of the events in the xtc files were fully reconstructed with the current configuration. In these events, most are physics events, some are prescaled trigger events and Bhabha events for luminosity study.

The events passing the **BGFilter** are collectively called **isPhysicsEvents** events.

[3]A bump is a local maximum of the deposited energy in a contiguous area in the calorimeter.

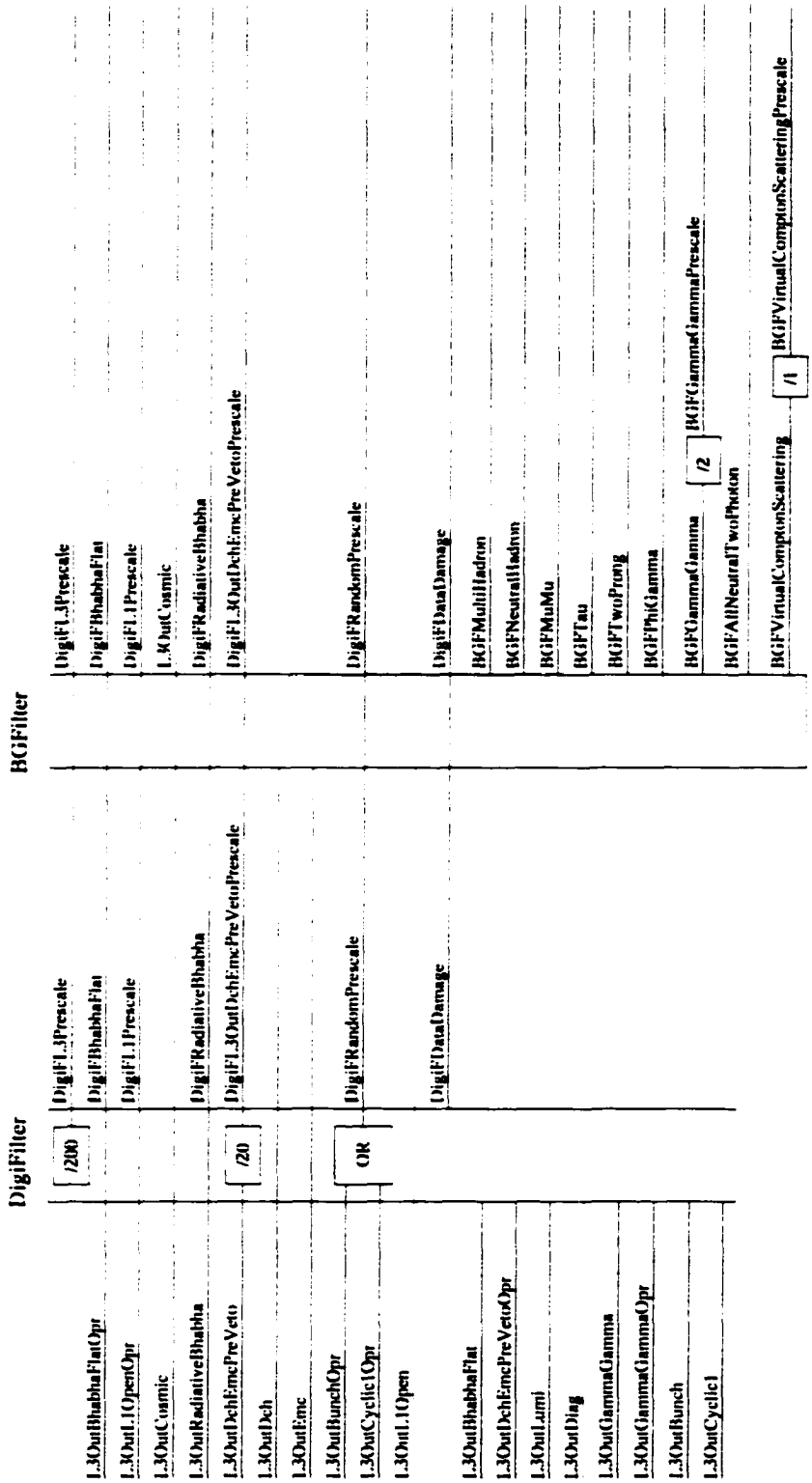

Figure 3.4: The configuration of the `DigiFilter` and `BGFilter` in prompt reconstruction [56].

These data have been written in the database. Other events left are stored on the tapes as xtc files. The Raw and Rec parts of the `isPhysicsEvents` events are not always kept on disk because of the huge size, but the Micro and Tag parts are kept on disk[4].

3.5. Skims and Streams

In order to make it easier for physics analyses to access small samples frequently, and for remote sites to export particular data sets, data skims and data streams for interesting physics modes and detector performance studies were filtered out. For each type of event, conventionally, one skim, a filter was configured based on tag database information. Then a central skim job on OPR processing wrote the small collections for merged skims as well as the large collection for total `isPhysicsEvents` events. In order to minimize the overall computing usage, the skims were merged into 20 streams based on the optimization between reducing overhead and maintaining convenience. An objectivity collection was made for each stream. Then some streams were converted to KANGA files.

An example for a skim is the `TauQEDAllevents` skim. It is configured for all possible final states in τ lepton decays. The tag bits classified by the decay multiplicity are included as follows:

[4]With the drastic increasing of the data, this strategy is being changed.

- **Tau1on1**. for both τ's decay to 1-prong states. i.e.. the states with one charged track:
- **Tau3Loose**. for one τ decays to 1-prong states and another decays to 3-prong states:
- **Tau3on3**. for both τs decay to 3-prong states:
- **Tau1on5**. for one τ decays to 1-prong and another decays to 5-prong states:
- **Tau2on1Tracking**. for final states similar to **Tau3Loose** but only two tracks are selected on the 3-prong side:
- **is2Gam4Prongs**. for four-prong two photon interaction and historically incorporated into this skim.

An example stream is Stream 16. which includes are the following skims:

- **BToll**. for B decays to two lepton final states:
- **BToDstarlnu**. for $B \rightarrow D^* l\nu$ decays:
- **Jpsitoll**. for $B \rightarrow J/\psi(\psi(2S)) + X$. $J/\psi(\psi(2S)) \rightarrow l^+l^-$ decays:
- **DiLepton**. for di-lepton final states.

The size of each skim is from $< 1\%$ to $\sim 10\%$ of **isPhysicsEvents**. The combined stream can have a size from $\sim 1\%$ to $\sim 20\%$ of **isPhysicsEvents**.

3.6. Jpsitoll Skim Selection

The skim Jpsitoll in Stream 16 was used for these analyses, which includes the preselected $B \to J/\psi(\psi(2S)) + X$, $J/\psi(\psi(2S)) \to l^+l^-$ events. The following criteria were applied:

- The event should be tagged as a BGFMultihadron event:
- The event satisfies the hadron selections for $B\overline{B}$ counting:
  - The event can pass L3OutDch or L3OutEmc trigger line. These two lines are the physics output lines of the Level 3 trigger, one from the DCT and the other from the EMT.
  - The tracks in fiducial volume with polar angle $0.41 < \theta_{lab} < 2.54$ and the neutrals with energy >30 GeV, polar angle within $0.41 < \theta_{lab} < 2.409$ are used for $B\overline{B}$ counting.
  - There are at least 3 GoodTracksLoose (described in the next chapter) tracks in the event.
  - The primary vertex must be reconstructed less than 0.5 cm in x-y plane and 6 cm in z from the beam spot.
  - R_2, which is the ratio of the second to the zeroth Fox-Wolfram moment, is required to be less than 0.5. The definition of the n-th Fox-Wolfram

moment [57] is:

$$H_n = \sum_{i,j} \frac{|\vec{p}_i||\vec{p}_j|}{E_{vis}^2} P_n(cos\theta_{ij}). \quad (3.1)$$

where $cos\theta_{ij}$ is the angle between particle i with momentum vector $\vec{p}_i$, and particle j with momentum vector $\vec{p}_j$. E_{vis} is the total visible energy of the event. P_n is the Legendre polynomials. Hadronic events have small R_2 values while Bhabha events have R_2 values around one.

- The total energy must be greater than 4.5 GeV.

- One of the four tag bits. `JpsiELoose`, `JpsiMuLoose`, `Psi2ELoose` and `Psi2MuLoose`, must be true. The first two bits are used for $J/\psi \to l^+l^-$ candidate selection and the details are discussed in the next chapter. The last two bits are used for $\psi(2S) \to l^+l^-$ candidate selection.

`Jpsitoll` skim is less than 2% of the `isPhysicsEvents` events. The loss of signal events at skim selection level is negligible. It is much easier to use `Jpsitoll` skim rather than all `isPhysicsEvents` events, and it yields a huge savings in computing resources and real time.

Chapter 4

Event Selection

4.1. Particle List

In each event in the *BABAR* data structure, all reconstructed particles are organized into *lists*. A list is a group of particles that satisfy some special requirements. Every list has a unique and somewhat descriptive name. It can be very generic, like the `ChargedTracks` list for all charged tracks in an event, but also can be very specific, like the `eLooseNoCal` list for all tracks passing loose electron-like selection but without calorimeter information.

Lists are available for both simple particles and intermediate or composite particles. The lists of intermediate particles can be obtained by combining the information from some lists of simple particles. An example is the `rho0Default` list for $\rho^0 \to \pi^+\pi^-$ candidates, which combines two `GoodTracksLoose` lists with pion mass assigned.

4.2. Track and Photon Quality

Before the intermediate particle candidates were built, the charged tracks and the photons were subjected to some quality cuts. This is crucial for several later procedures that have prerequisites on the quality of the single track and the single photon.

4.2.1. Track Quality Cuts

The primary purpose to perform track selection is background rejection at the early stage of analyses. Furthermore, the tracking efficiency studies that were applied to this analysis were made only for tracks that passed some loose requirements (labeled `GoodTracksLoose` below), and the selectors of particle identification (PID) only have reliable performance for tracks which satisfied quality requirements in specific angular regions.

Track quality is classified into four levels, with increasingly strict reconstruction criteria, denoted `ChargedTracks`, `GoodTracksVeryLoose`, `GoodTracksloose` and `GoodTracksTight`. The selections for these four lists are based on the tracking parameters and the DCH hit information.

`ChargedTracks` are all reconstructed tracks, and they are assigned pion mass hypothesis.

`GoodTracksVeryLoose` applies more cuts on tracks passing `ChargedTracks` crite-

ria. The additional cuts include the total momentum < 10 GeV/c: the number of of DCH hits > 0: the tracking fit χ^2 probability > 0: DOCA. which is the closest approach of the track in the x-y plane. < 1.5 cm: the magnitude of Zdoca. which is the z closest approach. < 10 cm.

`GoodTracksLoose` tightens two cuts based on `GoodTracksVeryLoose`: the transverse momentum P_t > 0.1 GeV/c: the number of DCH hits > 12.

`GoodTracksTight` additionally requires DOCA < 1 cm and |Zdoca|< 3 cm for `GoodTracksLoose` tracks.

For most tracks that come from the region close to the interaction point. `GoodTracksLoose` was used in this analysis. For those tracks that come from the intermediate decay points. `ChargedTracks` was used.

4.2.2. Photon Quality Cuts

`GoodPhotonLoose` selection was applied to all photons in the analyses. It requires a single calorimeter bumps unmatched with any track. The photon mass hypothesis was assigned for the bumps. The cut on minimum raw energy is 0.030 GeV. The lateral moment (LAT. described later) should be less than 0.8.

4.3. Particle Identification (PID)

To reconstruct the exclusive final states, good PID for leptons and hadrons over a wide range of momentum and solid angle is essential. Information from all the subdectors was combined to distinguish charged particles at high effciency.

4.3.1. Electron Identification

Several selectors[1] were used to identify electrons. Cuts on the following quantities were applied to the `GoodTracksLoose` tracks, and different values constitute different selectors:

- DCH dE/dx, which is a Gaussian distribution peaking at ~ 650 with the width of ~ 50 (Units are arbitary).
- The number of EMC crystals, $N_{crystal}$.
- E/p. E is the calibrated energy from the raw bump energy associated with a track, and p is the momentum of the track at the origin. The E/p distribution for electrons and positrons is centered at 1 after the E/p calibration and has a width of $0.02 \sim 0.03$. For hadrons and muons the E/p distribution is centered far away below 1 and has a long tail.

[1] A selector is a set of cuts.

- LAT, which denotes the lateral energy distribution [58]. The definition is:

$$LAT = \frac{\sum_{i=3}^{n} E_i r_i^2}{\sum_{i=3}^{n} E_i r_i^2 + E_1 r_0^2 + E_2 r_0^2}. \qquad E_1 \geq E_2 \geq ... \geq E_n. \tag{4.1}$$

The sum runs over all crystals in a shower. r_0 is the average distance between two crystals front-faces and r_i is the distance between the i-th crystal and the shower center. Generally LAT is smaller for electromagnetic showers than that for hadronic showers because electromagnetic showers in the calorimeter have most of their energy deposited in one or two crystals.

- A_{42}, which is a particular Zernike-moment. The general definition of Zernike-moment [59], A_{mn}, is:

$$A_{nm} = \sum_{r_i \leq R_0}^{n} \frac{E_I}{E} \cdot f_{nm} \frac{r_I}{R_0} \cdot e^{-im\phi_i}. \qquad R_0 = 15cm. \tag{4.2}$$

$$f_{nm}(\rho_i \equiv \frac{r_i}{R_0}) = \sum_{s=0}^{(n-m)/2} \frac{(-1)^s (n-s)! \rho_i^{n-2s}}{s!((n+m)/2-s)!((n-m)/2-s)!}. \tag{4.3}$$

where n, m are non-negative integers. And n-m is even. $m \leq n$. A_{mn} describes the shape variation of the shower and when $m \geq 2$ the azimuthal variation in shower shape comes in. So $|A_{42}|$ can be used for PID because the hadronic shower is more irregular than electromagnetic shower.

- When $N_\gamma > 9$ in DIRC, then the measured Cherenkov angle must be consistent

with an electron hypothesis within 3σ.

- $\Delta\phi$. which measures the separation in ϕ between the track extrapolated into EMC and the shower centroid.

The cuts for five modes of electron identification are summarized in Table 4.1.

Table 4.1: The criteria of the electron identification.

Selector	Mode	dE/dx	$N_{crystal}$	E/p	LAT	A_{42}	$N_\gamma > 9$	$\Delta\phi$
NoCal	1	(540, 860)	-	-	-	-	-	-
VeryLoose	2	(500, 1000)	3	(0.50, 5.0)	(-10.0, 10.0)	(-10.0, 10.0)	no	no
Loose	3	(500, 1000)	3	(0.65, 5.0)	(-10.0, 10.0)	(-10.0, 10.0)	no	no
Tight	4	(500, 1000)	3	(0.75, 1.3)	(0.0, 0.6)	(-10.0, 10.0)	no	no
VeryTight	5	(540, 860)	3	(0.89, 1.2)	(0.0, 0.6)	(-10.0, 0.11)	yes	yes

The selectors only use the tracks in the fiducial volume $20.6° < \theta_{lab} < 135.9°$. The efficiencies inside this angular region are $> 97\%$ for VeryLoose and Loose modes, $\sim 95\%$ for Tight mode and $\sim 88\%$ for VeryTight mode. NoCal mode was used only for tracks without EMC energy matched or beyond the EMC acceptance.

4.3.2. Muon Identification

Based on the EMC and IFR information, the muon selectors use the following variables:

- E_{cal}. which is the energy deposited in the EMC:
- N_L. which is the number of hit layers in IFR for a cluster:

- $hasInnner$, which tests if there is a hit in the inner RPC;
- F_h, which is the first hit layer in the cluster;
- L_h, which is the last hit layer in the cluster;
- λ, which is the number of interaction lengths traversed in *BABAR*;
- λ_{exp}, which is the expected number of interaction lengths traversed in *BABAR*;
- χ^2_{trk}, which is the $\chi^2/d.o.f.$ of the IFR hit strips in the cluster with respect to the track extrapolation;
- χ^2_{fit}, which is the $\chi^2/d.o.f.$ of the IFR hit strips in the cluster with respect to a third order polynomial fit of the cluster;
- $N_s(i)$, which is the total numbers of IFR hit strips in the i-th layer;
- N_s, which is the total number of IRF hit strips in the cluster.

Several variables are constructed with the information above:

$$\Delta\lambda = \lambda_{exp} - \lambda. \tag{4.4}$$

$$T_c = \begin{cases} \frac{N_L}{L_h - F_h + 1} & hasInner = false \\ \frac{N_L}{L_h - F_h} & hasInner = true \end{cases} \tag{4.5}$$

The average multiplicity of hit strips per layer. $\bar{m}$ and its error σ_m are calculated by combining the number of hit strips.

After validation with the control sample. the cuts for five selectors are summarized in Table 4.2.

Table 4.2: The criteria for muon identification.

Selector	Mode	E_{cal}	N_L	$\Delta\lambda$	λ	χ^2_{trk}	χ^2_{fit}	T_c	$\bar{m}$	σ_m
Minimum Ionizing (MIP)	1	< 0.5	-	-	-	-	-	-	-	-
VeryLoose	2	< 0.5	≥ 2	< 2.5	> 2			> 0.1	< 10	< 6
Loose	3	< 0.5	≥ 2	< 2	> 2	< 7	< 4	> 0.2	< 10	< 6
Tight	4	0.05 0.4	≥ 2	< 1	> 2.2	< 5	< 3	> 0.3	< 8	< 4
VeryTight	5	0.05 0.4	≥ 2	< 0.8	> 2.2	< 5	< 3	> 0.34	< 8	< 4

The selectors only used the tracks in the fiducial volume $17° < \theta_{lab} < 155°$. The efficiencies are $\sim$ 100%. $\sim$ 92%. $\sim$ 86%. $\sim$ 70% and $\sim$ 67% for five selectors. respectively.

4.3.3. Kaon and Pion Identification

Three subdetectors are involved in kaon selection. SVT. DCH and DIRC. Two types of selectors are available: `PidKaonSMSSelector`. which uses different likelihood ratios. and `PidKaonMicroSelector`. which uses likelihood with a neural-network-based approach. The first one was used in the analyses.

The likelihood functions for SVT and DCH are based on dE/dx information. Gaussian distributions were obtained for both subsystems after calibration.

The DIRC likelihood l_i for a particle i (electron. muon. pion. kaon. proton). consists two uncorrelated parts: the Gaussian part for Cherenkov angle and the Poisson part for photon counting.

For Cherenkov angle θ. its error σ_θ and expected angle Θ. the Gaussian part is

$$g_i = \frac{1}{\sqrt{2\pi}\sigma_\theta} e^{-0.5\cdot\chi_i^2}, \quad i = e.\mu.\pi.K.p. \tag{4.6}$$

where

$$\chi_i = \frac{\theta - \Theta_i}{\sigma_\theta}. \tag{4.7}$$

The normalization is:

$$\sum_{i=e}^{p} g_i = 1. \tag{4.8}$$

$$\sum_{i=x+1}^{p} g_i = (p - x)\cdot 0.2 = m. \tag{4.9}$$

$$\sum_{i=1}^{x} = 1 - m. \tag{4.10}$$

$$\tag{4.11}$$

To have a continuously defined probability, we must distinguish between particles that are above and below the Cherenkov threshold for a given momentum. With x being the heaviest particle above threshold. all particles more massive than x will have a constant probability of 0.2.

For the number of signal photons Ng_s, the background photons Ng_b and the expected number of photons Ng_{exp}, the Poisson[2] part can be constructed as:

$$p_i = \mathrm{P}(Ng_s + Ng_b; Ng_{exp} + Ng_b). \quad i = e, \mu, \pi, K, p. \tag{4.12}$$

The normalization is:

$$\sum_{i=e}^{p} p_i = 1. \tag{4.13}$$

Then we can calculate the total probability for particle i:

$$l_i = g_i \cdot p_i / \sum_{j=e}^{p} g_j \cdot p_j \tag{4.14}$$

After tuning with the control samples, the cuts associated with five selectors are summarized in Table 4.3.

The selectors only use the tracks in the fiducial volume $0.35 < \theta_{lab} < 2.55$. For tracks with momentum $< 3\mathrm{GeV}/c$, the efficiencies of the selectors are momentum dependent and range around $70 \sim 90\%$ for all selectors except the veto selector `NotAPion`, which has efficiency $> 90\%$.

To select charged pions, no dedicated selectors were used. A high-efficiency method is to reverse the requirements in kaon selectors, that is to apply a logical NOT.

[2]Poisson distribution for n observed and the expected value μ: $P(n; \mu) = \frac{\mu^n e^{-\mu}}{n!}$.

Table 4.3: The criteria for kaon identification.

Selector	Momentum range(GeV/c)			Likelihood cut		
	SVT	DCH	DIRC			
NotAPion (5)	< 0.5	< 0.6	> 0.6	reject. if $r_\pi l_\pi > l_K \& r_\pi l_\pi > l_p$		
				$p \leq 0.5, r_\pi = 0.1$		$p < 0.5, r_\pi = 1.0$
VeryLoose (1)	< 0.6	< 0.6	> 0.6	$l_K > r_\pi l_\pi \& l_K > r_p l_p, r_p = 1$		
				$p < 2.5, r_\pi = 3$	$p < 2.5, r_\pi = 3$	$0.4 < p < 0.7, r_\pi = 20$
Loose (2)	< 0.7, > 1.5	< 0.7, > 1.5	> 0.6	$l_K > r_\pi l_\pi$ if no DIRC; $l_K > r_\pi l_\pi \& l_K \geq r_p l_p, r_p = 1$		
				$p < 2.7, r_\pi = 1$	$p < 2.7, r_\pi = 80$	$0.5 < p < 0.7, r_\pi = 15$
Tight (3)	< 0.7	< 0.7	> 0.6	$l_K > r_\pi l_\pi \& l_K > r_p l_p, r_p = 1$		
				$p < 2.7, r_\pi = 1$	$p < 2.7, r_\pi = 80$	$0.5 < p < 0.7, r_\pi = 15$
VeryTight (4)	< 0.6	< 0.6	> 0.6	$l_K > r_\pi l_\pi \& l_K > r_p l_p, r_p = 1$		
				$p < 2.5, r_\pi = 3$	$p > 2.5, r_\pi = 200$	$0.4 < p < 0.7, r_\pi = 20$

4.4. Angular Cuts

Denoting the momentum vector of the i-th track as $\vec{p}_i$ for a set of n tracks, the thrust [60] is defined by

$$T = \frac{\sum_{i=1}^{n} |\vec{p}_i \cdot \hat{t}|}{\sum_{i=1}^{n} |\vec{p}_i|}. \tag{4.15}$$

The thrust axis $\hat{t}$ maximizes the value of T. A thrust angle is defined as the angle between the thrust axis of the B and the thrust axis of the rest of the event. Generally $B\bar{B}$ events with high multiplicity are more spherical, while the continuum events are more jet-like. Thus the absolute value of the cosine of this thrust angle can be used to reject continuum background (Figure 4.1) .

Several helicity angles for the decay $\Upsilon(4S) \rightarrow B\bar{B}, B \rightarrow J/\psi(e^+e^-, \mu^+\mu^-) + X$ are involved in the analyses. In the reaction $Y \rightarrow X + ...$ $X \rightarrow a + b$, the helicity angle of

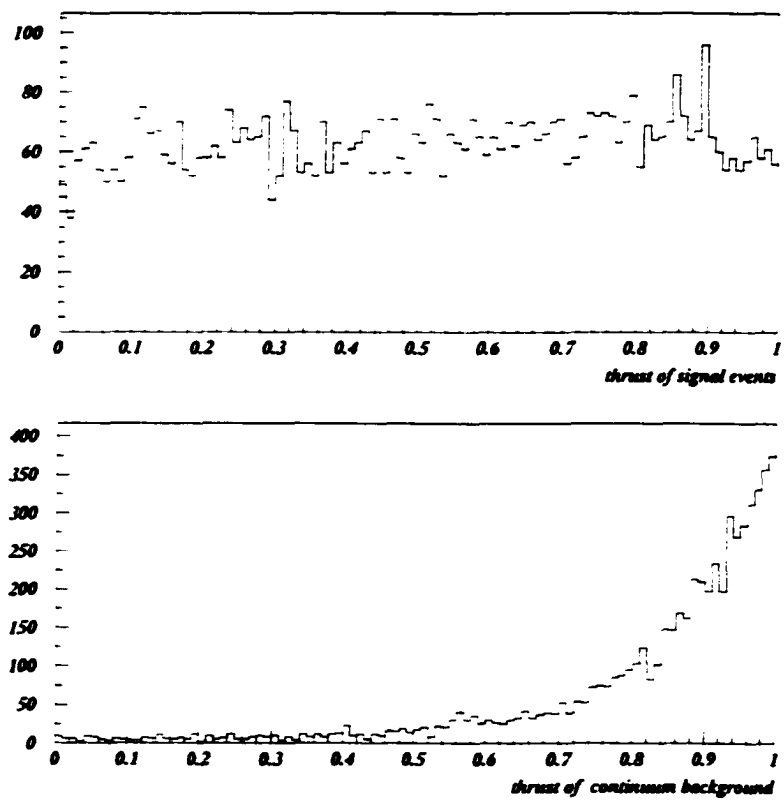

Figure 4.1: The absolute value of the cosine of the thrust angles.

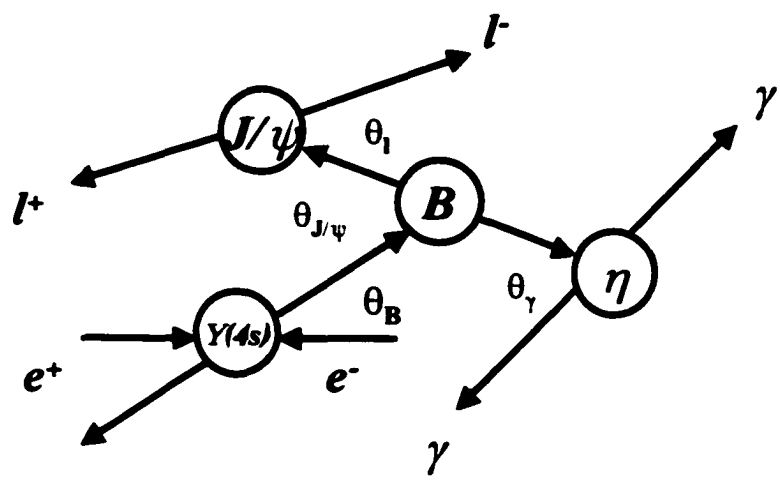

Figure 4.2: Helicity angles in B decays.

particle a is the angle measured in the rest frame of the decaying parent particle, X, between the direction of the decay daughter a and the direction of the grandparent particle Y. The figure 4.2 shows the decay chain of $\Upsilon(4S) \rightarrow B\bar{B}, B \rightarrow J/\psi\eta, \eta \rightarrow \gamma\gamma$ with all kinematic angles, θ_B, $\theta_{J/\psi}$, θ_l and θ_γ, where the $\bar{B}$ is not reconstructed.

For the decay of a pseudoscalar B, to a vector J/ψ plus a pseudoscalar X (η, η'), the lepton angular distribution from J/ψ follows $\sin^2\theta_l$. Furthermore, if X is η which decays to $\gamma\gamma$, the γ angular distribution is flat. The continuum backgrounds usually have different angular distribution from the signal. For the cosine of the lepton helicity

angle or γ helicity angle. the backgrounds peak at ± 1 (Figure 4.3. Figure 4.4).

4.5. Intermediate Candidate Preselection

The `CompositionTools` packages are used to form particle candidates. This is a tool kit or *BABAR* software package. used to compose new lists from existing lists such as `GoodTracksLoose`. `GoodPhotonLoose`. etc. The tool kit provides selectors and combinatoric engines so candidates can be combined into decay trees. Geometric and kinematic constraints can then be applied to the tree. Different vertexing and kinematic fitting routines are also possible. Thus the whole decay chain can be easily built.

When a composite particle list is built. the cuts used are very loose. They can be tightened in the final exclusive selections.

4.5.1. π^0 Candidate

The `pi0AllLoose` list was used. Two `GoodPhotonLoose` photons with energy greater than 0.03 GeV. $LAT < 0.8$ are combined. The invariant mass of the two photons should be less than 35 MeV/c^2 from the nominal π^0 mass in PDG [19]. A mass constraint is applied. but no χ^2 cut is required. This improves the resolutions but has no loss of potential signals. The π^0 mass resolution is ~ 5 MeV/c^2.

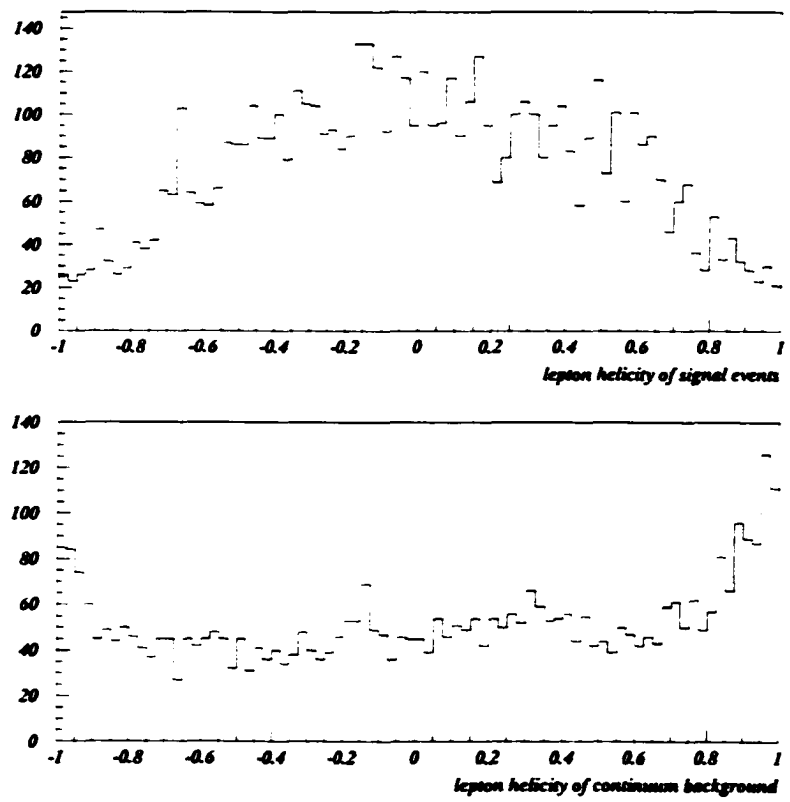

Figure 4.3: $cos\theta_l$ from J/ψ decay.

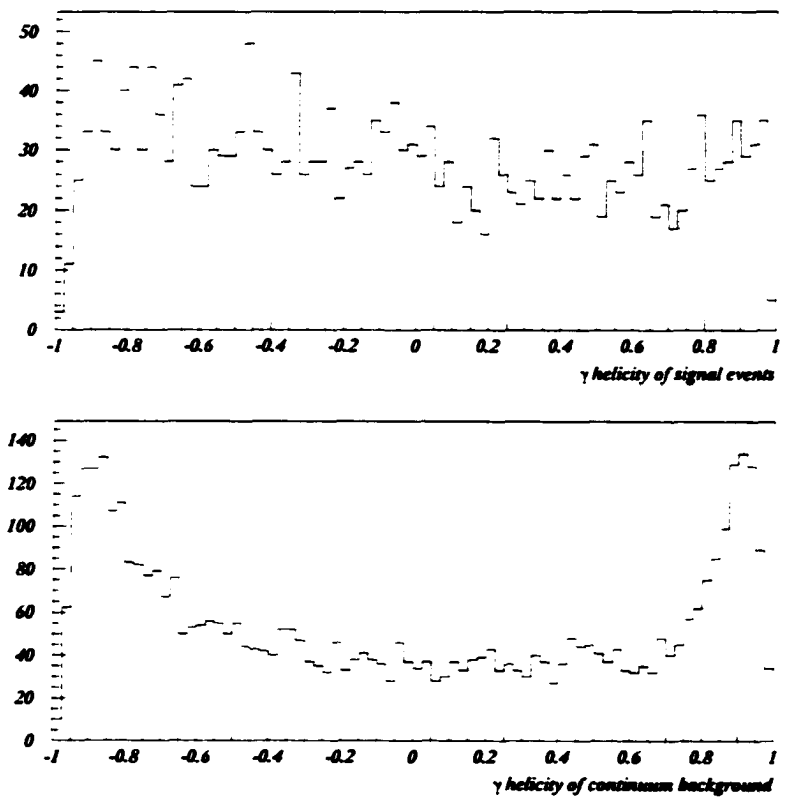

Figure 4.4: $cos\theta_\gamma$ from η decay.

4.5.2. K_S^0 Candidate

The `KsDefault` list was used for all $K_S^0 \to \pi^+\pi^-$ candidates. The list is constructed from all pairs of `ChargedTracks` tracks with opposited charge. which are assigned pion mass (but no PID is yet applied). The invariant mass of the two tracks is required to be less than 35 MeV/c^2 from the nominal K_S^0 mass in PDG [19]. Vertexing is applied but no convergence is required. This improves the resolutions but has no loss of potential signals. The K_S^0 mass resolution is ~ 3MeV/c^2.

4.5.3. o Candidate

The `phiDefault` list was used for all $o \to K^+K^-$ candidates. The list is constructed all pairs of `ChargedTracks` tracks with opposited charge. which are assigned kaon mass (but no PID is yet applied). The invariant mass of the two tracks is required less than 30 MeV/c^2 from the nominal o mass in PDG [19]. Vertexing is applied but no convergence is required. The o mass resolution is ~ 5 MeV/c^2.

4.5.4. η Candidate

The `etaDefault` list combined two lists. `etaggDefault`. which was used for $\eta \to \gamma\gamma$. and `eta3piDefault`. which was used for $\eta \to \pi^+\pi^-\pi^0$. The first one constructs two `GoodPhotonLoose` photons with energy great than 50 MeV. The invariant mass is required to be in the range from 0.47 GeV/c^2 to 0.62 GeV/c^2. The mass constraint

was applied but no χ^2 cut is applied. The latter one constructs two **GoodTracksLoose** tracks assigned pion mass and one **pi0AllLoose** π^0 candidate. The invariant mass is required to be in the range from 0.515 GeV/c^2 to 0.575 GeV/c^2. The vertexing is applied and the χ^2 probability is required to be greater than 0.001. This helps to reject background.

When the $\eta \to \gamma\gamma$ candidates are built, the number of fake combinations is large because there are many photons from π^0s in the event, which could be picked to form η candidates. A π^0 veto was applied to η candidates. This means the event was rejected if at least one γ from the η can be combined with any other γ in the event to construct a $\gamma\gamma$ with mass that is less than 20MeV/c^2 from the π^0 mass.

4.5.5. η' Candidate

The **etaPeppDefault** was used for $\eta' \to \pi^+\pi^-\eta, \eta \to \gamma\gamma$. It combines two **GoodTracksLoose** tracks assigned pion mass and one **etaggDefault** η candidate. The invariant mass is required to locate in the range from 0.900 GeV/c^2 to 1.010 GeV/c^2. The vertexing is applied and the χ^2 probability is required to be greater than 0.001.

4.5.6. J/ψ Candidate

The **JPsiLooseChm** list was constructed for J/ψ decays to leptons. The **ChargedTracks** tracks were used and the subsequent selections require **GoodTracksLoose** tracks. Two lists were included. $J/\psi \to e^+e^-$ and $J/\psi \to \mu^+\mu^-$.

The $J/\psi \to e^+e^-$ list constructs two **ChargedTracks** tracks with opposited charge. one can pass the **Loose** electron selection or **noCal** selection if it has no calorimeter information. The bremsstrahlung recovery procedure is applied. It is important because if radiation of bremsstrahlung photons occurs. the momentum of the $e^\pm$ tracks is lower than what it should be and a long tail is produced in the e^+e^- mass distributions. If the loss is not recovered the selection efficiency will be reduced. Vertexing is applied but no convergence is required. If the vertexing fails. a simple 4-vector addition is used to make a J/ψ. The final invariant mass must be in the very wide range 2.8 GeV/c^2 to 3.3 GeV/c^2.

The $J/\psi \to \mu^+\mu^-$ list constructs two **ChargedTracks** tracks with opposited charge. one can pass the **Loose** muon selection and the other can pass **MIP** selection. Vertexing is applied but no convergence is required. If the vertexing is fails. a simple 4-vector addition is used to make a J/ψ. The final invariant mass must be in the very wide range 2.8 GeV/c^2 to 3.3 GeV/c^2.

The J/ψ mass resolution is $\sim$ 11 MeV/c^2.

4.6. B Candidate Preselection

The B candidates were first reconstructed from combinations of candidate lists that result in an invariant mass between 3 GeV/c^2 and 7 GeV/c^2. Five decay modes were combined as in Table 4.4. A vertex constraint was applied but no convergence was required. The B selection was further refined in the final selections of the exclusive modes.

Table 4.4: The final states were combined.

$B^0 \rightarrow J/\psi(e^+e^-, \mu^+\mu^-)\eta(\gamma\gamma, \pi^+\pi^-\pi^0)$
$B^0 \rightarrow J/\psi(e^+e^-, \mu^+\mu^-)\eta'(\pi^+\pi^-\eta(\gamma\gamma))$
$B^0 \rightarrow J/\psi(e^+e^-, \mu^+\mu^-)\phi(K^+K^-)$
$B^+ \rightarrow J/\psi(e^+e^-, \mu^+\mu^-)\phi(K^+K^-)K^+$
$B^0 \rightarrow J/\psi(e^+e^-, \mu^+\mu^-)\phi(K^+K^-)K^0_S(\pi^+\pi^-)$

B meson production at the $\Upsilon(4S)$ has polar angle distribution $1 - cos^2\theta$, while the continuum background has $1 + cos^2\theta$. So $cos\theta$ can be used to reject continuum background. It turns out, however, that $cos\theta$ is a relatively weak variable to reject background. Two other parts of the 4-vector, the momentum of the B candidate, $|p|$, and the energy of the B candidate, E, are much more discriminating variables.

Two minimally correlated functions of E and p, were used to isolate the B meson signal: ΔE and M_{ES}. The first variable is

$$\Delta E = E^*_B - E^*_{beam}. \tag{4.16}$$

which is the difference between the reconstructed energy of the B meson in center-of-mass frame. E_B^*. and the expected energy of the B candidate in the center-of-mass frame. E_{beam}^*. which is a half of the total energy of the e^+e^- system in the center-of-mass frame. and called the beam energy conventionally. The second variable is

$$M_{ES} = \sqrt{E_{beam}^{*2} - P_B^{*2}}. \tag{4.17}$$

which is called energy substituted mass. P_B^* is the reconstructed momentum of the B meson in center-of-mass frame.

Typically these two variables form a two dimensional Gaussian distribution for the B signal and a nearly flat two dimensional distribution for background. The data will be displayed and analyzed in this plane and the one-dimensional projections.

4.7. Cut Optimization

Several cuts have been intensively studied within *BABAR* [61] such as the J/ψ mass cut. and the K_S^0 mass cut. These cuts were not optimized again here. For this work the cut optimization was performed by varying the remaining cuts. which are the combinations of PID modes. angular cuts and other mass cuts. For $B \to J/\psi\phi K$ the ratio $s/\sqrt{s+b}$ was maximized because it leads to the minimal statistical error on the branching fractions. where s is the number of signal events and b is the number of background events. However. for $B^0 \to J/\psi\phi$. $B \to J/\psi\eta$ and $B \to J/\psi\eta'$. s/b

was maximized because the maximum yield was expected to set the best upper limit on the branching fractions.

For each set of cuts, the number of signal MC events falling into 3σ box, called *signal box* in the $\Delta E - M_{ES}$ plane, was counted. This number was subsequently scaled to reflect the yield in $1fb^{-1}$ on-peak data, which is s. The factor was calculated from the cross section of $B\overline{B}$ production, and the available branching fraction from CLEO [46] measurement or an assumed branching fraction of 1×10^{-5} if no result is available. For background b, in order to get enough statistics, the number of events in the *Grand SideBand* (GSB) region was counted. A flat distribution of background was assumed so the scaling factor is just the area ratio between the GSB and the signal box. All possible background sources were combined by weight of the cross section then scaled to the yield in $1fb^{-1}$ on-peak data.

The GSB refers to the following region excluding the signal box:

-0.3 GeV $< \Delta E <$ 0.3 GeV: 5.2 GeV/$c^2 < M_{ES} <$ 5.3 GeV/c^2.

The signal box varies slightly channel by channel:

For $B \rightarrow J/\psi\eta, \eta \rightarrow \gamma\gamma$ (Fig. 4.5), $B \rightarrow J/\psi\eta'$ (Fig. 4.7): -0.1 GeV$< \Delta E <$ 0.1 GeV: 5.27 GeV/$c^2 < M_{ES} <$ 5.29 GeV/c^2;

For $B \rightarrow J/\psi\eta, \eta \rightarrow \pi^+\pi^-\pi^0$ (Fig. 4.6): -0.072 GeV$< \Delta E <$ 0.072 GeV: 5.27 GeV/$c^2 < M_{ES} <$ 5.29 GeV/c^2.

For $B^0 \rightarrow J/\psi\omega$ (Fig. 4.8), $B^+ \rightarrow J/\psi\phi K^+$ (Fig. 4.9) and $B^0 \rightarrow J/\psi\phi K^0_S$

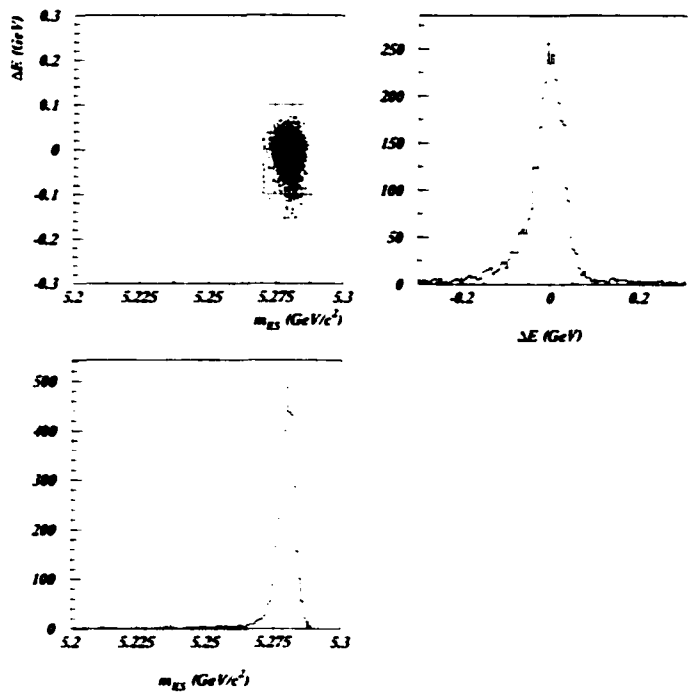

Figure 4.5: $B \rightarrow J/\psi\eta, \eta \rightarrow \gamma\gamma$ signal MC. ΔE vs M_{ES} (left top). M_{ES} projection in ΔE signal region (left bottom), and ΔE projection in M_{ES} signal region (right).

(Fig. 4.10): -0.057 GeV< ΔE < 0.057 GeV: 5.272 GeV/c^2 < M_{ES} < 5.288 GeV/c^2:

4.8. Exclusive Selection

After cut optimization, the final cuts were obtained for these analyses:

- $B \rightarrow J/\psi\eta, \eta \rightarrow \gamma\gamma$ selection
  - J/ψ
    - ee channel
      - 2.95 GeV/c^2 < $M_{J/\psi}$ < 3.14 GeV/c^2;

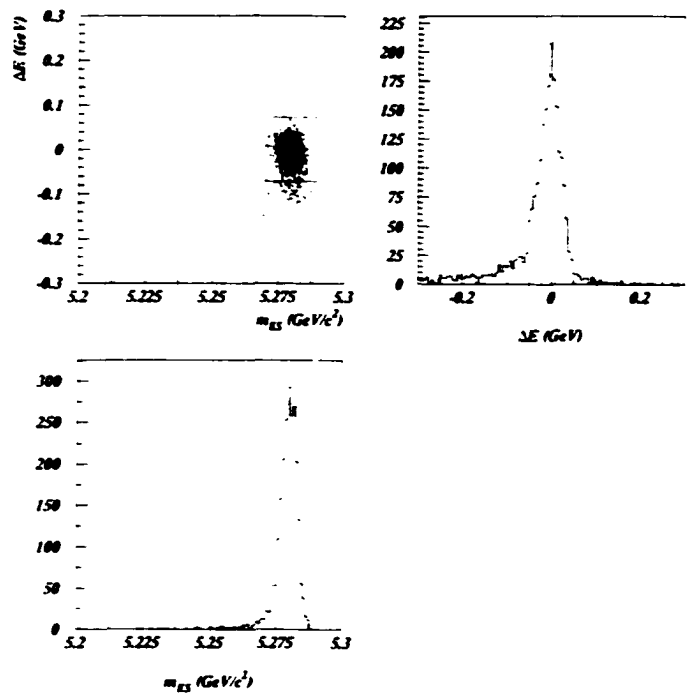

Figure 4.6: $B \rightarrow J/\psi\eta, \eta \rightarrow \pi^+\pi^-\pi^0$ signal MC. ΔE vs M_{ES} (left top). M_{ES} projection in ΔE signal region (left bottom), and ΔE projection in M_{ES} signal region (right).

· PID(**VeryTight** electron, **VeryTight** electron);

* $\mu\mu$ channel

· 3.06 GeV/c^2 < $M_{J/\psi}$ < 3.14 GeV/c^2;

· PID(**Tight** moun, **Tight** moun);

– η

* 0.529 GeV/c^2 < M_η < 0.565 GeV/c^2;

* π^0 veto;

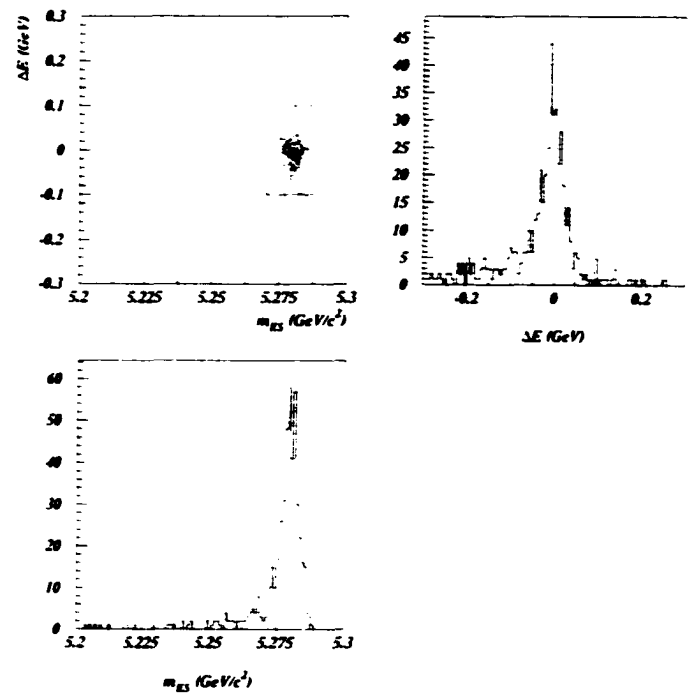

Figure 4.7: $B \rightarrow J/\psi\eta'$ signal MC. ΔE vs M_{ES} (left top). M_{ES} projection in ΔE signal region (left bottom). and ΔE projection in M_{ES} signal region (right).

- helicity
  - $|cos(\theta_l)| < 0.8$:
  - $|cos(\theta_\gamma)| < 0.8$:
- Thrust
  - $|cos(\theta_T)| < 0.8$.

- $B \rightarrow J/\psi\eta, \eta \rightarrow \pi^+\pi^-\pi^0$ selection
  - J/ψ

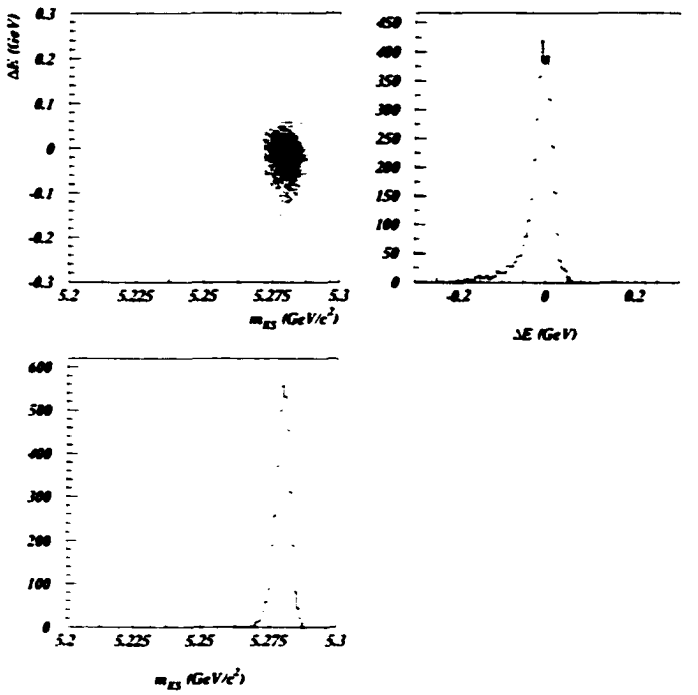

Figure 4.8: $B^0 \rightarrow J/\psi\, o$ signal MC. ΔE vs M_{ES} (left top). M_{ES} projection in ΔE signal region (left bottom). and ΔE projection in M_{ES} signal region (right).

* ee channel

  · $2.95\text{GeV}/c^2 < M_{J/\psi} < 3.14\text{GeV}/c^2$:

  · PID (**VeryTight** electron. **VeryTight** electron):

* $\mu\mu$ channel

  · $3.06\ \text{GeV}/c^2 < M_{J/\psi} < 3.14\ \text{GeV}/c^2$:

  · PID(**Tight** moun. **Tight** moun):

– η

* $0.529\ \text{GeV}/c^2 < M_{\eta} < 0.565\ \text{GeV}/c^2$:

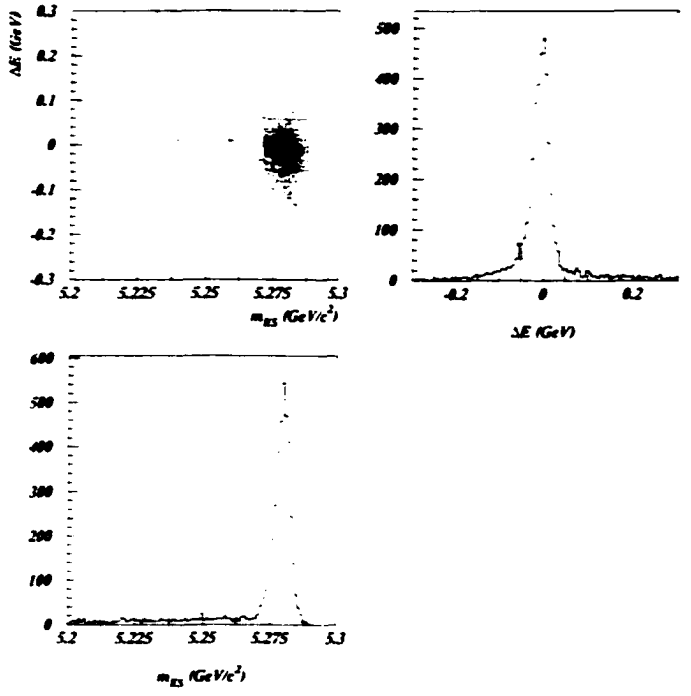

Figure 4.9: $B^{+} \rightarrow J/\psi K^{+}$ signal MC. ΔE vs M_{ES} (left top). M_{ES} projection in ΔE signal region (left bottom). and ΔE projection in M_{ES} signal region (right).

* π^0: 0.120 GeV/c^2 < M_{π^0} < 0.150 GeV/c^2:

* two **GoodTracksLoose** tracks. !(**NotAPion**):

- Helicity

  * $|cos(\theta_l)| < 0.8$:

- Thrust

  * $|cos(\theta_T)| < 0.8$.

- $B \rightarrow J/\psi\eta'$ selection

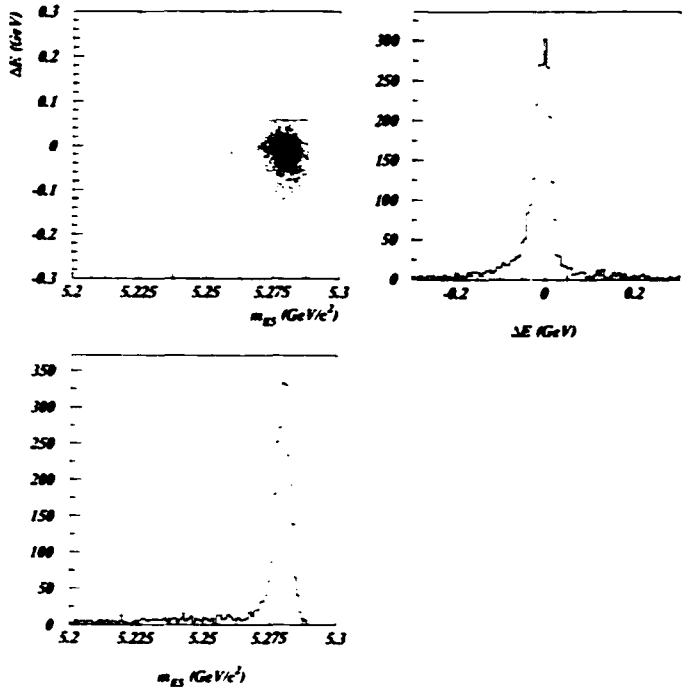

Figure 4.10: $B^0 \rightarrow J/\psi K^0_S$ signal MC. ΔE vs M_{ES} (left top). M_{ES} projection in ΔE signal region (left bottom). and ΔE projection in M_{ES} signal region (right).

- J/ψ
  - ee channel
    - $2.95\text{GeV}/c^2 < M_{J/\psi} < 3.14\text{GeV}/c^2$:
    - PID (**VeryTight** electron. **VeryTight** electron):
  - $\mu\mu$ channel
    - $3.06\ \text{GeV}/c^2 < M_{J/\psi} < 3.14\ \text{GeV}/c^2$:
    - PID: (**Tight** muon. **Tight** muon):
- η'

* 0.938 GeV/c^2 < $M_{\eta'}$ < 0.978 GeV/c^2:

* η

· 0.529 GeV/c^2 < M_{η} < 0.565 GeV/c^2:

· π^0 veto:

* two **GoodTracksLoose** tracks. !(**NotAPion**):

– Helicity

* $|cos(\theta_l)| < 0.8$:

– Thrust

* $|cos(\theta_T)| < 0.8$.

• $B^0 \rightarrow J/\psi o$ selection

– J/ψ

* ee channel

· 2.95 GeV/c^2 < $M_{J/\psi}$ < 3.14 GeV/c^2:

· PID(**VeryTight** electron. **VeryTight** electron):

* $\mu\mu$ channel

· 3.06 GeV/c^2 < $M_{J/\psi}$ < 3.14 GeV/c^2:

· PID (**Tight** muon. **Tight** muon):

– o

* 1.004 GeV/c^2 < M_ϕ < 1.034 GeV/c^2:

* PID (**VeryTight** kaon. **Loose** kaon):

- Thrust

* $|cos(\theta_T)| < 0.8$.

- $B^+ \rightarrow J/\psi\phi K^+$ selection

- J/ψ

* ee channel

· 2.95 GeV/c^2 < $M_{J/\psi}$ < 3.14 GeV/c^2:

· PID (**VeryTight** electron. **Loose** electron):

* $\mu\mu$ channel

· 3.06 GeV/c^2 < $M_{J/\psi}$ < 3.14 GeV/c^2:

· PID (**Loose** muon. **VeryLoose** muon):

- ϕ

* 1.004 GeV/c^2 < M_ϕ < 1.034 GeV/c^2:

* PID (**VeryTight** kaon. **Loose** kaon):

- kaon

* PID: **NotAPion**.

- $B^0 \rightarrow J/\psi\phi K^0_S$ selection

- J/ψ
  - ee channel
    - 2.95 GeV/c^2 < $M_{J/\psi}$ < 3.14 GeV/c^2:
    - PID (**VeryTight** electron. **Loose** electron):
  - $\mu\mu$ channel
    - 3.06 GeV/c^2 < $M_{J/\psi}$ < 3.14 GeV/c^2:
    - PID(**Loose** muon. **VeryLoose** muon):
- ϕ
  - 1.004 GeV/c^2 < M_ϕ < 1.034 GeV/c^2:
  - PID (**VeryTight** kaon. **Loose** kaon).
- K_S^0
  - 0.489 GeV/c^2 < $M_{K_S^0}$ < 0.507 GeV/c^2.

The final selection criteria will be applied to the signal MC. background MC and the real data. to obtain the efficiency. the background and the signal in the next several chapters.

Chapter 5

Background Estimation

5.1. Background Description

We use M_{ES} distributions in different regions from different samples to estimate the background. For the exclusive B decay modes, the background in the M_{ES} distribution can have two components [61]: the combinatoric background, which is described by an ARGUS [62] function, and the peaking background, which peaks in the signal region and is described by a Gaussian function.

The ARGUS function is a parameterization of the shape of the beam constrained mass near the kinematic endpoint:

$$y = p_1 \cdot \frac{x}{E^*_{beam}} \cdot \sqrt{1 - (\frac{x}{E^*_{beam}})^2} \cdot e^{p_2(1-\frac{x}{E^*_{beam}})^2}. \tag{5.1}$$

where p_1 is the normalization factor, p_2 is called the shape parameter, E^*_{beam} is the beam energy described in Section 4.6, and x is the measured M_{ES} of events passing the

cuts. The shape parameter p_2 has critical impact on the background determination and should be obtained reliably.

5.2. Sources and Samples

For each decay mode, the combinatoric background, denoted N_{ARGUS}, comes from three independent sources: continuum events, denoted N_{cont}; generic $B\overline{B}$ decay events without a J/ψ, denoted $N_{b\bar{b}}$; and inclusive $B \rightarrow J/\psi + X$ decay events, denoted $N_{J/\psi-ARGUS}$. The peaking background only comes from inclusive $B \rightarrow J/\psi + X$ decay events, denoted $N_{J/\psi-Gauss}$. The sum of N_{ARGUS} and $N_{J/\psi-Gauss}$ is the total background used in the next chapters.

The different components of the background appear in different data samples separately or together. Based on the data samples available, redundant measurements on background components can be performed. Thus some data samples may be used to determine the background number for the result, while some other samples can be used for cross-checking.

There are six data samples for cross-checking:

- Continuum MC events, which include both *uds* and $c\bar{c}$. After scaling to the on-peak data luminosity, this sample gives an estimation of N_{cont};
- Off-peak data, which also measures N_{cont} after scaling to the on-peak data luminosity. When off-peak data was used, the M_{ES} was calculated based on

beam parameters fixed to the on-peak data:

P_x = -0.11943 GeV/c;

P_y = 0.0;

P_z = 5.8534 GeV/c;

E_{cms} = 12.0919 GeV;

E_{beam} = (10.58 GeV)/2.

- Generic $B\overline{B}$ MC events without a J/ψ, which provides an estimation of $N_{b\overline{b}}$ after scaling to the on-peak data luminosity;

- Inclusive J/ψ MC events, which measure the combinatoric component $N_{J/\psi-ARGUS}$ and the peaking background $N_{J/\psi-Gauss}$ after scaling to the on-peak data luminosity;

- J/ψ *mass sideband* of the on-peak data, which is used to estimate a combinatoric component equal to $N_{b\overline{b}} + N_{cont}$ after the right scaling. Instead of the J/ψ mass region used for signal selection described in the previous chapter, the following regions make up the J/ψ mass sideband for events passing the same cuts except J/ψ mass:

  - ee: $3.156\text{GeV}/c^2 < m_{J/\psi} < 3.300\text{GeV}/c^2$;

  - $\mu\mu$: $2.980\text{GeV}/c^2 < m_{J/\psi} < 3.024\text{GeV}/c^2$ and $3.156\text{GeV}/c^2 < m_{J/\psi} < 3.300\text{GeV}/c^2$.

In order to translate the number of the combinatoric background events in the J/ψ mass sideband region into the combinatoric components $N_{cont} + N_{b\bar{b}}$ in the J/ψ mass signal region, scaling factors were determined by an inclusive J/ψ study [63]. The scaling factor can be different for different PID combinations of the two leptons from J/ψ. For each combination, the inclusive mass distribution of all J/ψ's with the right lepton PID in the `Jpsitoll` skim of the on-peak data was fitted with a Gaussian and a third order Chebychev polynomial (Figure 5.1). The Chebychev function was analytically integrated over both the J/ψ signal region (line-hatched area in Figure 5.1) and the J/ψ sideband region (box-hatched area in Figure 5.1). The ratio of the two integrals is the scaling factor. Table 5.1 summaries the scaling factors used in this analysis.

Table 5.1: J/ψ sideband scaling factors.

mode	ee	$\mu\mu$
`VeryTight, VeryTight`	1.35	0.46
`VeryTight, Tight`	1.35	0.46
`VeryTight, Loose`	1.35	0.46
`VeryTight, VeryLoose`	1.38	0.46
`Tight, Tight`	1.35	0.46
`Tight, Loose`	1.38	0.46
`Loose, VeryLoose`	1.42	0.46

- ΔE *sideband* of the on-peak data, which gives a measurement of the combinatoric component that can be converted to $N_{b\bar{b}} + N_{cont} + N_{J/\psi-ARGUS}$ in the ΔE

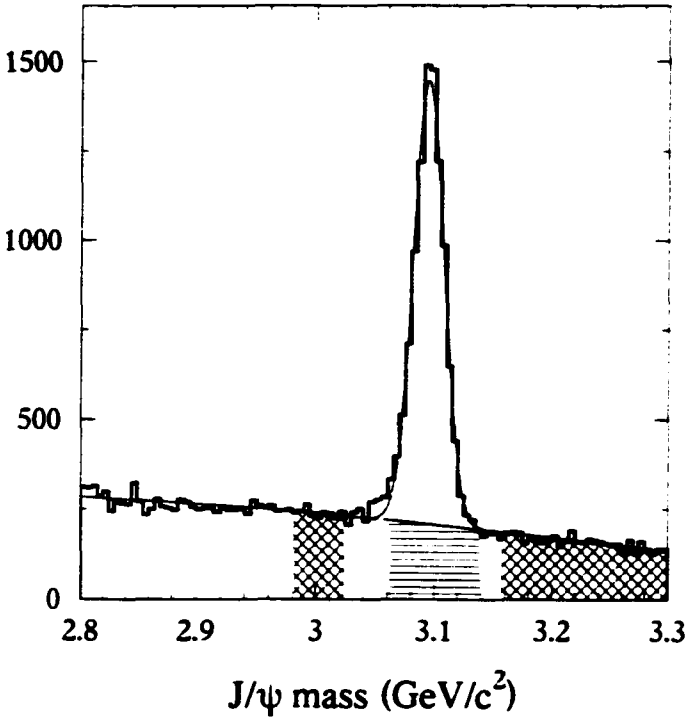

Figure 5.1: An example of inclusive J/ψ mass distribution with lepton PID combination (**VeryTight** muon. **VeryTight** muon).

signal region after applying the right scaling. It also has a peaking component $N_{\Delta E-Gauss}$. The ΔE sideband regions are defined as:

- for $B^+ \to J/\psi K^+$. $B^0 \to J/\psi K^0_S$. and $B^0 \to J/\psi \rho$
  - $0.057\text{GeV} < |\Delta E| < 0.3\text{GeV}$:
  - $5.2\text{GeV}/c^2 < m_{ES} < 5.3\text{GeV}/c^2$:
- for $B \to J/\psi\eta$. $\eta \to \gamma\gamma$ and $B \to J/\psi\eta'$
  - $0.1\text{GeV} < |\Delta E| < 0.3\text{GeV}$:
  - $5.2\text{GeV}/c^2 < m_{ES} < 5.3\text{GeV}/c^2$:

- for $B \rightarrow J/\psi\eta, \eta \rightarrow \pi^+\pi^-\pi^0$

  * $0.072\text{GeV} < |\Delta E| < 0.3\text{GeV}$:

  * $5.2\text{GeV}/c^2 < m_{ES} < 5.3\text{GeV}/c^2$.

A factor f_1 is necessary to convert the combinatoric background in the ΔE sideband region for the on-peak data to the combinatoric component in ΔE signal region. f_1 is just the relative area of the two regions (Table 5.2). The peaking component in ΔE sideband region. $N_{\Delta E-Gauss}$. should be comparable with the peaking background in ΔE signal region with additional scaling.

Table 5.2: f_1 value for all modes.

$B^+ \rightarrow J/\psi K^+$	0.2347
$B^0 \rightarrow J/\psi K_S^0$	0.2347
$B^0 \rightarrow J/\psi$	0.2347
$B \rightarrow J/\psi\eta, \eta \rightarrow \gamma\gamma$	0.3333
$B \rightarrow J/\psi\eta, \eta \rightarrow \pi^+\pi^-\pi^0$	0.2458
$B \rightarrow J/\psi\eta'$	0.3333

The ΔE signal region of the on-peak data is the sample used to show the final results. The events passing all cuts in this region include all combinatoric background. the peaking background. and the signal events.

5.3. Overall Strategy

All modes studied in this analysis are rare decays, where the background may be a significant fraction of the signal. In order to minimize the bias, the *blind analysis* technique described below was used.

5.3.1. Blind Analysis

The blind analysis requires the signal box in the $M_{ES} - \Delta E$ plane from the on-peak data be covered. Thus the M_{ES} distribution in ΔE signal region of the on-peak data was not looked at before the detailed background study and efficiency study had been done. Before the signal box was unblinded, all possible background studies were done only with the six cross-checking samples.

5.3.2. Measurement Method

When the result is determined, the M_{ES} distribution in ΔE signal region for events passing all cuts is examined and fit with an ARGUS function plus a Gaussian (The outer shape in Figure 5.2). The integral of the ARGUS in the M_{ES} signal region (The box-hatched area in Figure 5.2) gives the combinatoric background. The number of events in the Gaussian corresponds to the signal plus the peaking background, so somehow one needs to determine the amount of peaking background (A full hatched area under the line shape of a Gaussian in Figure 5.2). This can be estimated with the

inclusive J/ψ MC sample with signal events removed. During the fitting the ARGUS shape parameter is fixed to a value obtained from the *fake* sample described later.

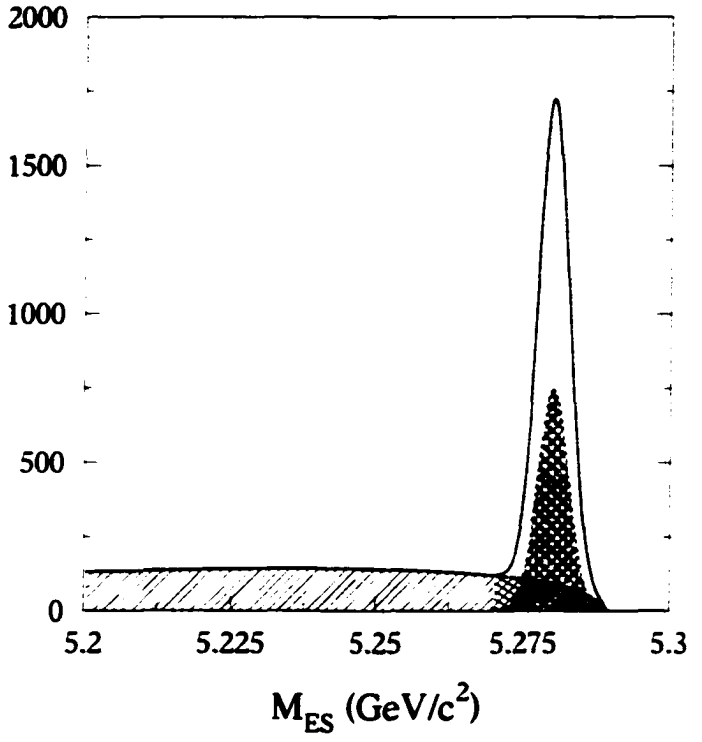

Figure 5.2: An illustration of M_{ES} distribution. Each component is just normalized to an arbitrary number.

While the measurement on one of the six samples mentioned in Section 5.2. J/ψ MC sample. gives the peaking background. the measurements from all six samples also give correlated estimations of the combinatoric background components. N_{cont}. $N_{b\bar{b}}$ and $N_{J/\psi-ARGUS}$. A fit to the six overconstrained measurements on these three components is described in Section 5.6. The result on the total combinatoric background from the fit was used as a cross-check to the combinatoric background used

in result determination described above. In all the fits to the cross-checking samples, if one sample has combinatoric background only, it was fitted with an ARGUS function. If one sample has both combinatoric background and peaking background, it was fitted with an ARGUS function plus a Gaussian. Fake samples were also used in all six samples to get ARGUS shape parameters.

5.4. The Fake Samples

In most cases both for result determination and background measurements, the M_{ES} distributions after all cuts have very few events, so determining the ARGUS shape and normalization from those sparse distributions would have large statistical uncertainties. A method to determine better ARGUS shape parameters was used (But the normalization of the ARGUS function in the final fit for results was still taken from the final M_{ES} distribution.).

This method employs *fake* samples, where the J/ψ is replaced by a fake J/ψ. The fake J/ψ is selected with identical selection criteria in each mode except for logically reversing the lepton identification. In modes with a ϕ, the ϕ can also be replaced by a fake ϕ, which is selected with identical selection criteria in each mode except for logically reversing the kaon identification. The point is to provide large statistics and thus to improve the knowledge of the ARGUS shape parameters.

For $B \to J/\psi\eta$ and $B \to J/\psi\eta'$, the fake J/ψ sample was used for all six cross-

checking data samples. For $B^0 \to J/\psi\phi$ the fake $J/\psi\phi$ sample was used for continuum MC, off-peak data, generic $B\overline{B}$ MC and J/ψ sideband samples. But the fake J/ψ sample without a fake ϕ was used for inclusive J/ψ MC and ΔE sideband samples because if all tight PID cuts for J/ψ and ϕ are reversed in these two samples, more peaking background due to other $B \to J/\psi + X$ decays will feed in and distort the distribution shape. For $B^+ \to J/\psi\phi K^+$ and $B^0 \to J/\psi\phi K^0_S$ the fake $J/\psi\phi$ sample was used for all six cross-checking data samples. The shape parameters for $B^+ \to J/\psi\phi K^+$ are listed in Table 5.3 as an example. They are comparable to each other within the statistical uncertainties. This shows that the fake sample works reasonably well.

Table 5.3: ARGUS shape parameters for $B^+ \to J/\psi\phi K^+$.

source	ARGUS shape Parameter from the fake samples
continuum(uds)	-30.41±3.33
continuum($c\bar{c}$)	-23.86±3.22
off-peak	-24.29±4.44
generic $B\overline{B}$	-21.44±3.47
Inclusive J/ψ	-20.39±4.01
J/ψ sideband(ee)	-23.96±1.58
J/ψ sideband($\mu\mu$)	-23.39±1.23
ΔE sideband	-21.59±0.73

5.5. The Background Distributions of Six Samples

The background distributions for all channels are shown in the following figures. For every plot, the upper part is the distribution of the fake sample and the bottom part is the background distribution after all cuts.

The fake samples are used to fix better the ARGUS shape parameter, but not to determine the ARGUS normalization. For example, Figure 5.6 shows the ARGUS shape determination from the off-peak data in the channels with a ϕ. The top plots of the three pairs of plots are the fake samples showing the fit that determines the shape parameter. The lower plots in the pairs show the events passing all cuts. In these channels only $B^0 \to J/\psi\phi K_S^0$ indicates that some events will pass all the cuts. The lower plot for $B^0 \to J/\psi\phi K_S^0$ shows one event, and the corresponding ARGUS curve is normalized to total area one, but its shape was determined using the higher statistics of the upper plot. After accounting for the ratio of off-peak to on-peak luminosity, the integral of the ARGUS shape from this lower plot over the M_{ES} signal region would project a combinatoric background estimation of about one event.

After applying the right scaling factors, the ARGUS components in the six background measurements for each mode are summarized in Table 5.4 and Table 5.5.

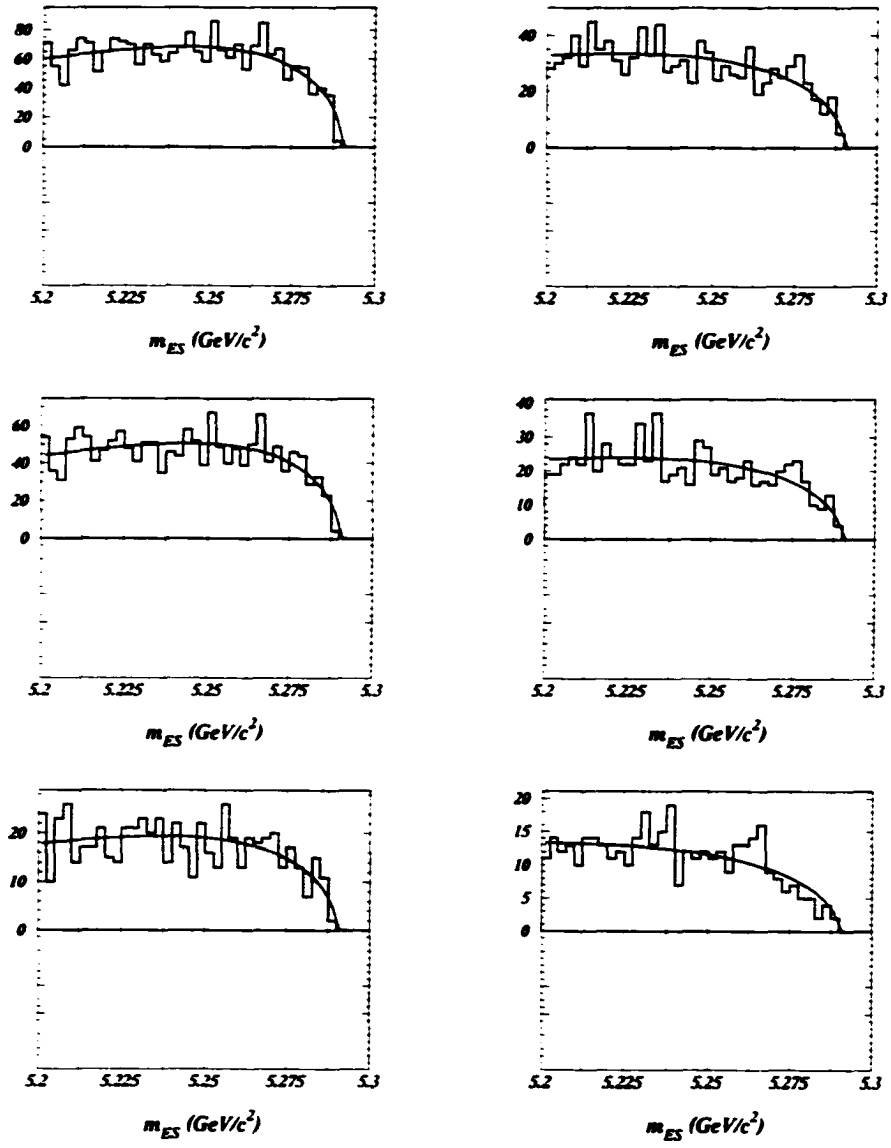

Figure 5.3: Continuum MC background: left, uds; right, $c\bar{c}$. From top to bottom: $B \to J/\psi\eta, \eta \to \gamma\gamma$, $B \to J/\psi\eta, \eta \to \pi^+\pi^-\pi^0$, $B \to J/\psi\eta'$. For every plot: upper, the distribution of the fake sample; bottom, the background distribution after all cuts.

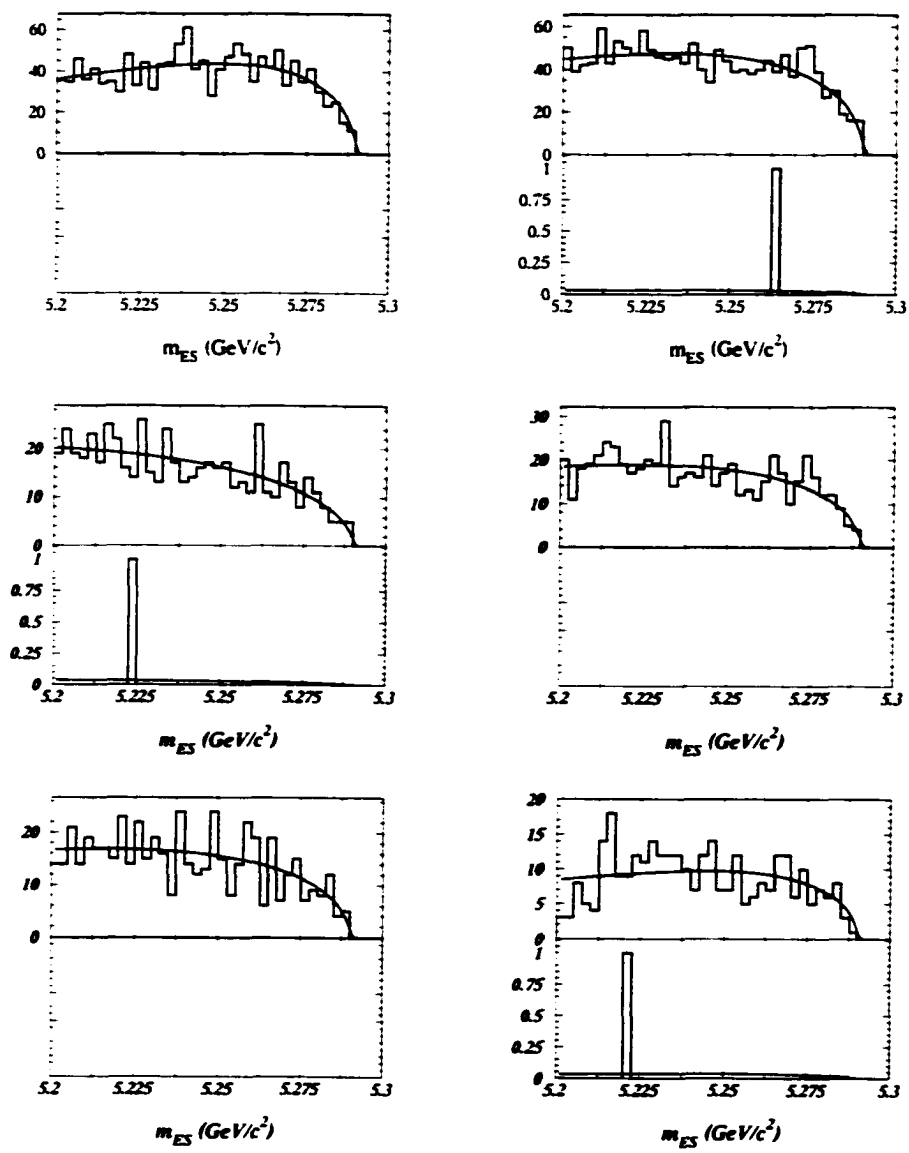

Figure 5.4: Continuum MC background: left, uds; right, $c\bar{c}$. From top to bottom: $B^+ \to J/\psi K^{*+}$, $B^0 \to J/\psi K^0_S$, $B^0 \to J/\psi\rho$. For every plot: upper, the distribution of the fake sample; bottom, the background distribution after all cuts.

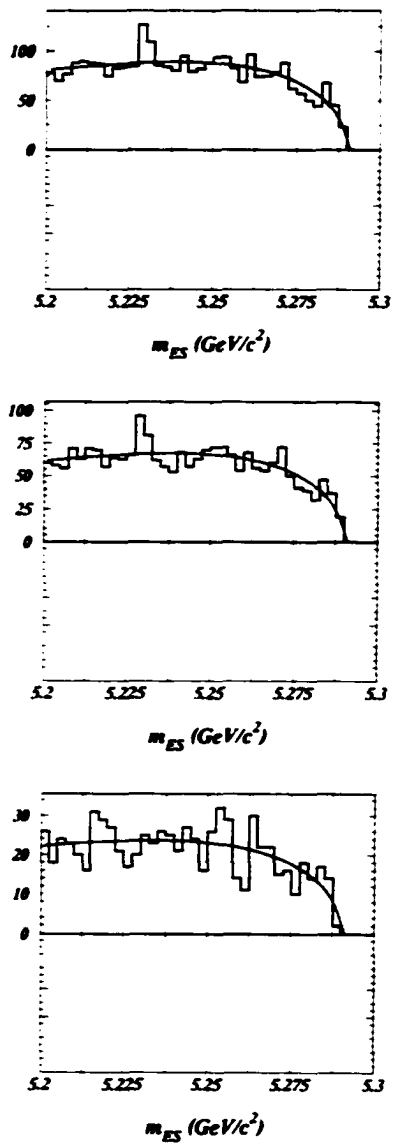

Figure 5.5: Off-peak data background. From top to bottom: $B \to J/\psi\eta, \eta \to \gamma\gamma$, $B \to J/\psi\eta, \eta \to \pi^+\pi^-\pi^0$, $B \to J/\psi\eta'$. For every plot: upper, the distribution of the fake sample; bottom, the background distribution after all cuts.

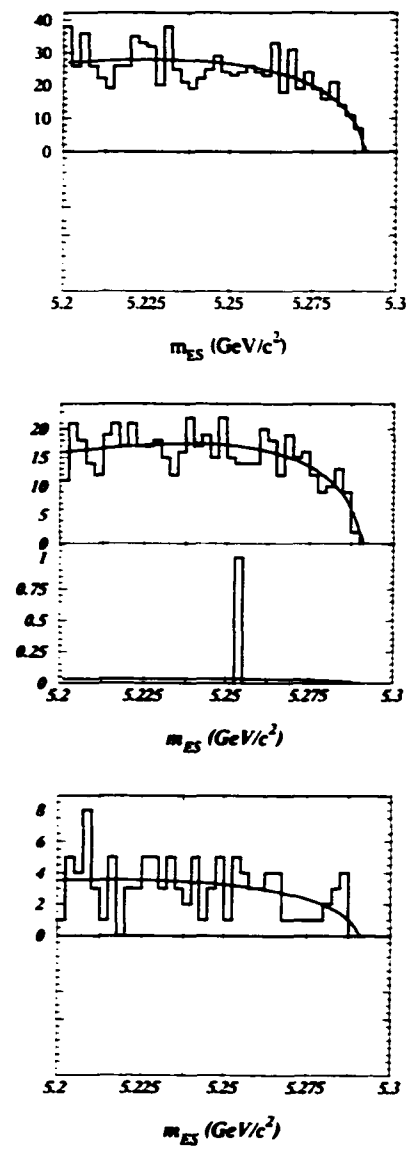

Figure 5.6: Off-peak data background. From top to bottom: $B^+ \to J/\psi K^+$, $B^0 \to J/\psi K^0_S$, $B^0 \to J/\psi$. For every plot: upper, the distribution of the fake sample; bottom, the background distribution after all cuts.

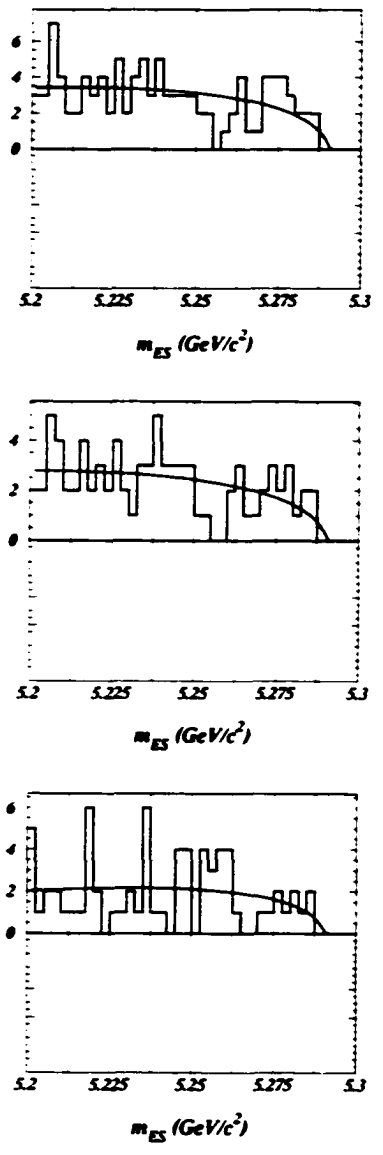

Figure 5.7: Generic $B\overline{B}$ MC background. From top to bottom: $B \to J/\psi\eta, \eta \to \gamma\gamma$. $B \to J/\psi\eta, \eta \to \pi^+\pi^-\pi^0$. $B \to J/\psi\eta'$. For every plot: upper, the distribution of the fake sample; bottom, the background distribution after all cuts.

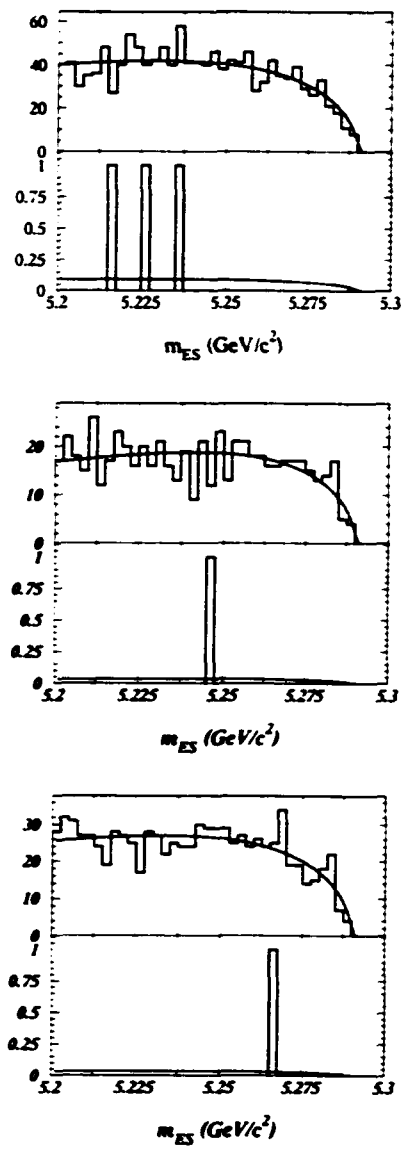

Figure 5.8: Generic $B\overline{B}$ MC background. From top to bottom: $B^+ \rightarrow J/\psi K^+$, $B^0 \rightarrow J/\psi K^0_S$, $B^0 \rightarrow J/\psi$. For every plot: upper, the distribution of the fake sample; bottom, the background distribution after all cuts.

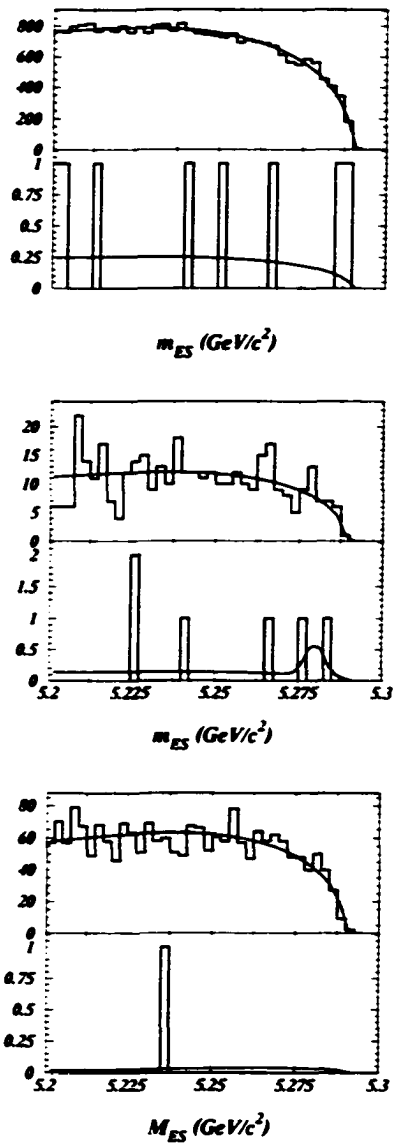

Figure 5.9: Inclusive J/ψ MC background. From top to bottom: $B \to J/\psi\eta, \eta \to \gamma\gamma$, $B \to J/\psi\eta, \eta \to \pi^+\pi^-\pi^0$, $B \to J/\psi\eta'$. For every plot: upper, the distribution of the fake sample; bottom, the background distribution after all cuts.

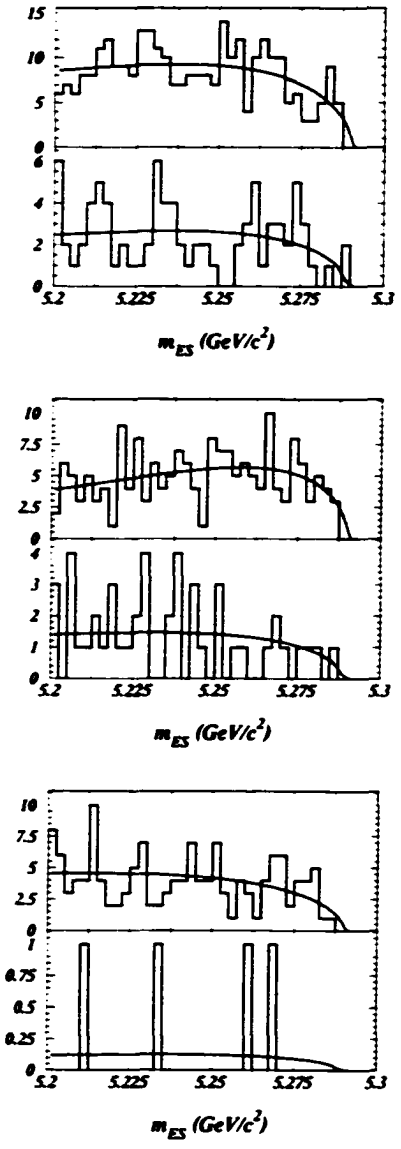

Figure 5.10: Inclusive J/ψ MC background. From top to bottom: $B^+ \to J/\psi\phi K^+$, $B^0 \to J/\psi\phi K^0_S$, $B^0 \to J/\psi\phi$. For every plot: upper, the distribution of the fake sample; bottom, the background distribution after all cuts.

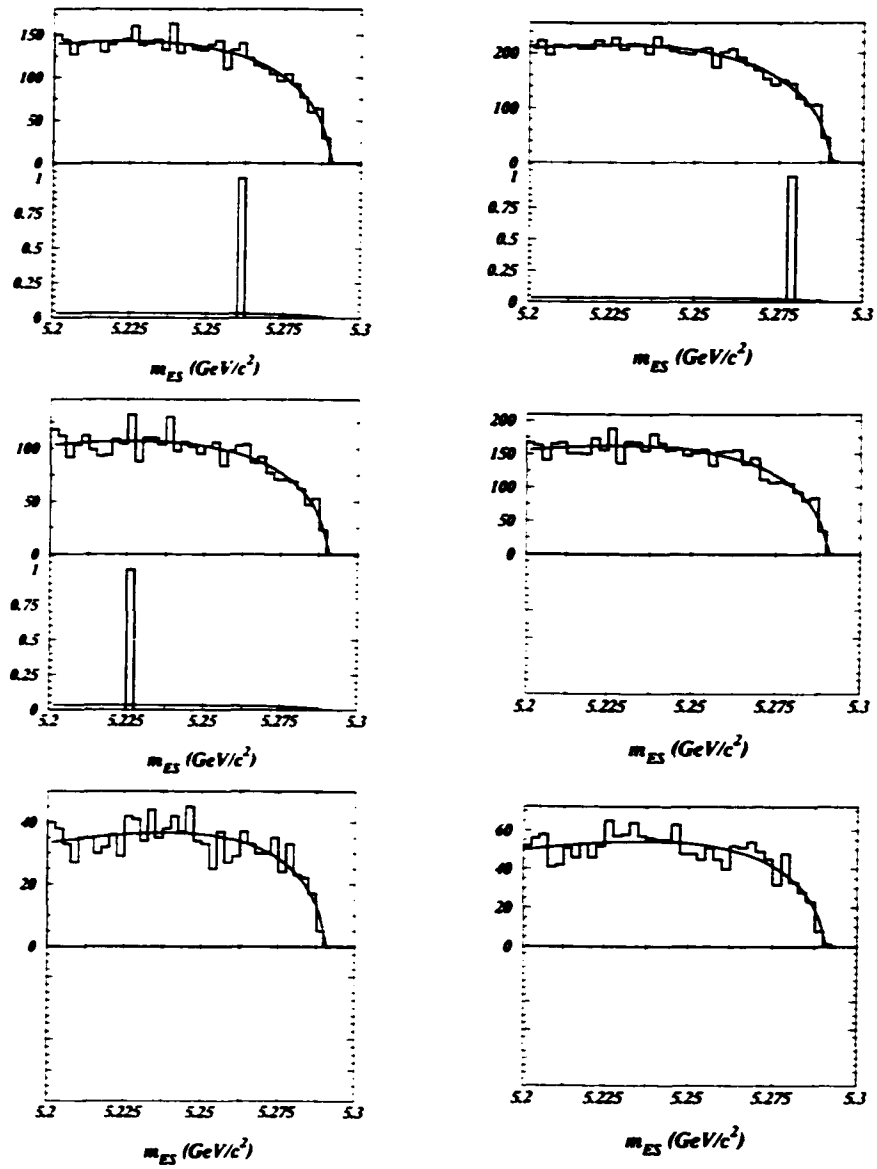

Figure 5.11: Background in J/ψ sidebands: left, ee channel: right, $\mu\mu$ channel. From top to bottom: $B \to J/\psi\eta, \eta \to \gamma\gamma$, $B \to J/\psi\eta, \eta \to \pi^+\pi^-\pi^0$, $B \to J/\psi\eta'$. For every plot: upper, the distribution of the fake sample: bottom, the background distribution after all cuts.

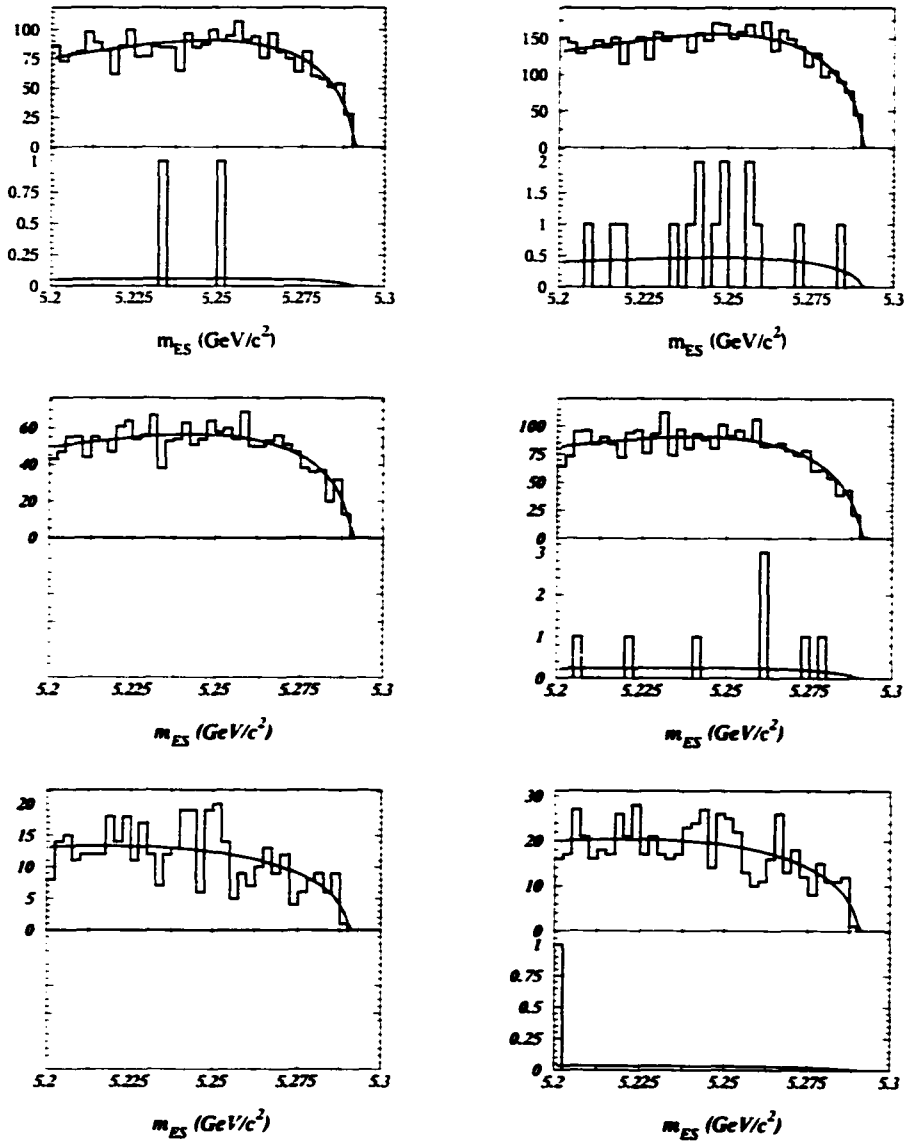

Figure 5.12: Background in J/ψ sidebands: left, ee channel: right, $\mu\mu$ channel. From top to bottom: $B^+ \to J/\psi\phi K^+$, $B^0 \to J/\psi\phi K^0_S$, $B^0 \to J/\psi\phi$. For every plot: upper, the distribution of the fake sample: bottom, the background distribution after all cuts.

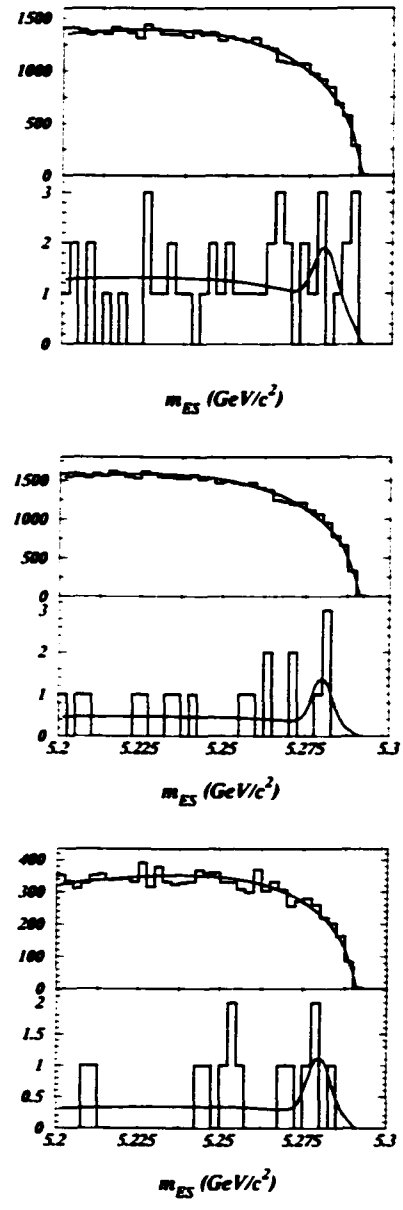

Figure 5.13: Background in ΔE sideband. From top to bottom: $B \to J/\psi\eta, \eta \to \gamma\gamma$. $B \to J/\psi\eta, \eta \to \pi^+\pi^-\pi^0$. $B \to J/\psi\eta'$. For every plot: upper, the distribution of the fake sample; bottom, the background distribution after all cuts.

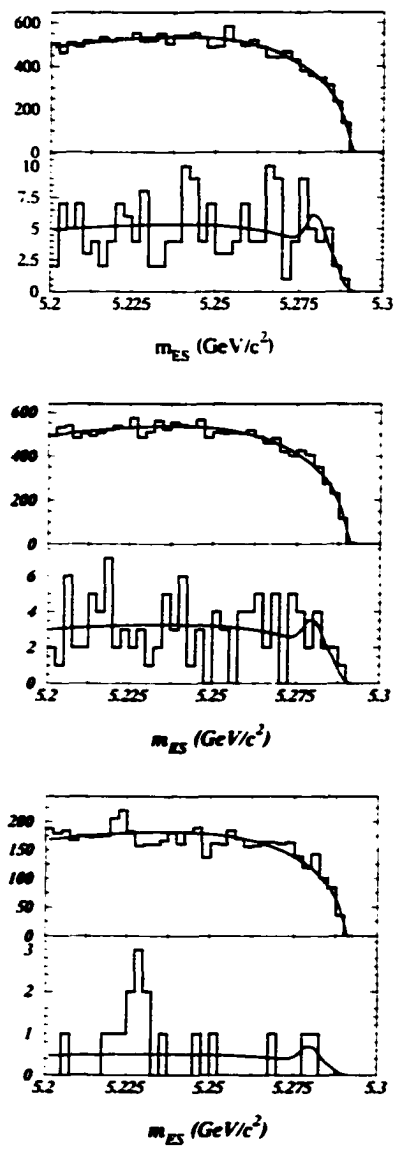

Figure 5.14: Background in ΔE sideband. From top to bottom: $B^+ \to J/\psi\phi K^+$. $B^0 \to J/\psi\phi K^0_S$. $B^0 \to J/\psi\phi$. For every plot: upper, the distribution of the fake sample; bottom, the background distribution after all cuts.

Table 5.4: The six correlated measurements for cross-checking combinatoric background after scaling to the $50.9fb^{-1}$ on-peak data luminosity for $B \to J/\psi\eta, \eta \to \gamma\gamma$, $B \to J/\psi\eta, \eta \to \pi^+\pi^-\pi^0$ and $B \to J/\psi\eta'$.

source	$B \to J/\psi\eta, \eta \to \gamma\gamma$	$B \to J/\psi\eta, \eta \to \pi^+\pi^-\pi^0$	$B \to J/\psi\eta'$
continuum MC	0.0	0.0	0.0
off-peak data	0.0	0.0	0.0
generic $B\overline{B}MC$	0.0	0.0	0.0
Inclusive J/ψ MC	0.7±0.2	0.4±0.2	0.2±0.1
J/ψ sideband of on-peak data	0.3±0.2	0.2±0.2	0.0
ΔE sideband of on-peak data	2.0±0.2	0.6±0.2	0.6±0.2

Table 5.5: The six correlated measurements for cross-checking combinatoric background after scaling to the $50.9fb^{-1}$ on-peak data luminosity for $B^0 \to J/\psi\phi$, $B^+ \to J/\psi\phi K^+$ and $B^0 \to J/\psi\phi K_S^0$.

source	$B^0 \to J/\psi\phi$	$B^+ \to J/\psi\phi K^+$	$B^0 \to J/\psi\phi K_S^0$
continuum MC	0.8±0.7	0.7±0.7	0.5±0.5
off-peak data	0	0	1.0±1.0
generic $B\overline{B}$ MC	0.4±0.4	1.1±0.6	0.4±0.4
Inclusive J/ψ MC	0.5±0.2	6.5±0.3	3.6±0.3
J/ψ sideband of on-peak data	0.1±0.1	1.3±0.4	0.4±0.2
ΔE sideband of on-peak data	0.4±0.1	5.0±0.3	2.9±0.2

5.6. A Global Fit to the Six Samples

Three uncorrelated ARGUS components can be extracted from a global χ^2 fit to the six correlated background measurements. If we denote the six measurements as y_1 (Inclusive J/ψ MC), y_2 (Continuum MC), y_3 (Off-peak data), y_4 (Generic $B\bar{B}$), y_5 (J/ψ Sideband) and y_6 (ΔE sideband), and denote the three unknowns as x_1 (Inclusive J/ψ, $N_{J/\psi-ARGUS}$), x_2 (Continuum, N_{cont}) and x_3 (Generic, $N_{b\bar{b}}$), the following matrices can be constructed:

$$\vec{Y} = \begin{pmatrix} y_1 \\ y_2 \\ y_3 \\ y_4 \\ y_5 \\ y_6 \end{pmatrix}, \quad \hat{U} = \begin{pmatrix} 1 & 0 & 0 \\ 0 & 1 & 0 \\ 0 & 1 & 0 \\ 0 & 0 & 1 \\ 0 & 1 & 1 \\ 1 & 1 & 1 \end{pmatrix}, \quad \vec{X} = \begin{pmatrix} x_1 \\ x_2 \\ x_3 \end{pmatrix}. \tag{5.2}$$

Here $\vec{Y}$ is the measurement matrix and $\vec{X}$ is the unknown matrix. The relationship between them is:

$$\vec{Y} = \hat{U}\vec{X}. \tag{5.3}$$

The covariance matrix for the measured quantities $\widehat{C_y}$ is known. Each element was

Table 5.6: The fit results on combinatoric components in the cross-checking samples for $B \to J/\psi\eta, \eta \to \gamma\gamma$, $B \to J/\psi\eta, \eta \to \pi^+\pi^-\pi^0$ and $B^+ \to J/\psi K^+$.

	$B \to J/\psi\eta, \eta \to \gamma\gamma$	$B \to J/\psi\eta, \eta \to \pi^+\pi^-\pi^0$	$B \to J/\psi\eta'$
N_{cont}	0.0	0.0	0.0
N_{bb}	0.0	0.0	0.0
$N_{J/\psi-ARGUS}$	1.0 ± 0.2	0.2±0.1	1.8±0.4
total	1.7±0.2	0.6±0.2	0.6±0.2

obtained from the error on the normalization of the fit. So the χ^2 is

$$\chi^2(\vec{X}) = (\vec{Y} - \hat{U}\vec{X})^T \widehat{C}_y^{-1} (\vec{Y} - \hat{U}\vec{X}). \tag{5.4}$$

and the three estimated backgrounds are given by

$$\vec{X} = \widehat{C}_x^{-1} \hat{U}^T \widehat{C}_y^{-1} \vec{Y}. \tag{5.5}$$

$$\widehat{C}_x = \hat{U}^T \cdot \widehat{C}_y^{-1} \cdot \hat{U}. \tag{5.6}$$

The covariance matrix of the backgrounds is $\hat{U}^{-1}$ itself and the error on the total background is

$$\sigma_{bckg} = \sum_{i,j} \hat{U}_{ij}^{-1}. \tag{5.7}$$

The fitting results on three components for all modes are shown in Tables 5.6 and Tables 5.7 .

Table 5.7: The fit results on combinatoric components in the cross-checking samples for $B^0 \to J/\psi\rho$, $B^+ \to J/\psi\rho K^+$ and $B^0 \to J/\psi\rho K^0_S$.

	$B^0 \to J/\psi\rho$	$B^+ \to J/\psi\rho K^+$	$B^0 \to J/\psi\rho K^0_S$
N_{cont}	0	0.3±0.5	0.2±0.3
N_{bb}	0.1±0.3	0.8±0.5	0.0
$N_{J/\psi-ARGUS}$	0.4±0.1	5.7±0.3	3.0±0.2
total	0.4±0.1	5.8±0.3	3.2±0.2

5.7. Background Results and Cross-Checking

The combinatoric background used to determine the results, N_{ARGUS}, are listed in Table 5.8. The M_{ES} distributions used to obtain these numbers are discussed in the next chapter.

Table 5.8: The combinatoric background used to determine the results, N_{ARGUS}.

$B \to J/\psi\eta, \eta \to \gamma\gamma$	1.7±0.4
$B \to J/\psi\eta, \eta \to \pi^+\pi^-\pi^0$	0.7±0.3
$B \to J/\psi\eta'$	0.5±0.3
$B^0 \to J/\psi\phi$	0.3±0.2
$B^+ \to J/\psi\rho K^+$	7.8±0.6
$B^0 \to J/\psi\rho K^0_S$	3.3±0.4

A quick comparison between Table 5.8 and Row total in Table 5.6 and in Table 5.7 shows that the global fit results are consistent with the combinatoric background used to determine the results.

The peaking background from inclusive J/ψ after scaling to the $50.9fb^{-1}$ on-peak data luminosity are listed in Table 5.9. For example, the contribution from the very small peaking background can be seen together with the combinatoric background in the plots in Figure 5.9.

Table 5.9: The peaking background results from inclusive J/ψ sample after scaling to the $50.9fb^{-1}$ on-peak data luminosity. $N_{J/\psi-Gauss}$.

$B \rightarrow J/\psi\eta, \eta \rightarrow \gamma\gamma$	0.0
$B \rightarrow J/\psi\eta, \eta \rightarrow \pi^+\pi^-\pi^0$	0.8±0.8
$B \rightarrow J/\psi\eta'$	0.0
$B^0 \rightarrow J/\psi o$	0.0
$B^+ \rightarrow J/\psi o K^+$	0.0
$B^0 \rightarrow J/\psi o K_S^0$	0.0

The sum of N_{ARGUS} and $N_{J/\psi-Gauss}$ is the total background used in the next chapters.

Chapter 6

Efficiencies, Yields and Systematic Uncertainties

6.1. Efficiencies

For each mode, the raw efficiency was calculated as the ratio between the number of MC signal events falling into the signal box after all cuts and the total number of MC events generated. Several corrections were applied to the raw efficiency because of discrepancies between the real data and MC in a few areas such as PID efficiency, tracking efficiency, and the absolute momentum scale.

6.1.1. PID Corrections

The corrections are necessary because of selector efficiency differences between the MC and the real data. The efficiency look-up tables were produced by binning the track information in momentum, θ, ϕ using efficiencies of the PID selectors applied to the high purity control samples from the real data. When the MC events were

used, the default particle lists , which usually have higher efficiency, were not used. Alternatively, the new candidate lists with more realistic efficiency from the look-up tables were produced. Thus the same level of inefficiency was imposed on the MC as was found in the real data. This is the so-called the PID killing technique [64].

At the early stage of the analysis with SP3 MC, an additional correction from lepton PID was applied because the lepton PID is used in hadronic B decays for this analysis, but the control samples for look-up tables were created using Bhabha events, dimuon events, and other low multiplicity events. The correlation between the momenta and the angles of the two leptons from J/ψ decays could introduce a systematic effect. The inclusive J/ψ analysis [65] gives the corrections to the efficiencies for different lepton PID combinations (Table 6.1). The average value for ee modes and $\mu\mu$ modes was used because the two modes were not separated in this analysis. This correction is unnecessary when the SP4 signal MC was used because of better agreement between the real data and the simulation.

The kaon momentum is very low in these decays. Particularly, most of kaons from ϕ decay in $B \to J/\psi\phi K$ have momentum less than 1 GeV/c (Figure 6.1). The bachelor kaon momentum in $B^+ \to J/\psi\phi K^+$ is higher but still less than 1.5GeV/c (Figure 6.2). In this region the kaon selectors have large discrepancies between MC and the real data(Fig.6.3, [66]) so the correction factor can be quite large.

Table 6.1: Relative efficiency with lepton PID corrections.

mode	ee	$\mu\mu$
VeryTight. VeryTight	0.946	0.960
VeryTight. Tight	0.959	0.960
VeryTight. Loose	0.960	0.964
VeryTight. VeryLoose	0.971	0.989
Tight. Tight	0.960	0.964
Tight. Loose	0.971	0.989
Loose. VeryLoose	0.974	1.019

6.1.2. Track Smearing

Track smearing was used for SP3 MC because there is a momentum resolution difference between the simulation and the real data in Run1 period. The high statistics sample of $B \rightarrow J/\psi K^{-}$ was used to study this feature [61]. The sample shows the difference between MC and the real data is different for $J/\psi \rightarrow e^{+}e^{-}$ and $J/\psi \rightarrow \mu^{+}\mu^{-}$. $J/\psi \rightarrow \mu^{+}\mu^{-}$ is better because the Bremsstrahlung is less in $\mu^{+}\mu^{-}$ than in $e^{+}e^{-}$. And the difference varies with the DCH high voltage from 1900V to 1960V for $J/\psi \rightarrow \mu^{+}\mu^{-}$ but not for $J/\psi \rightarrow e^{+}e^{-}$. The correction procedure is to apply a smearing factor to degrade the resolution in the p_t of the MC tracks to match the resolution in the real data. For $\mu\mu$ mode, the smearing factors applied to the p_t resolution are 1.32 ± 0.13 and 1.14 ± 0.13 for DCH voltage at 1900V and 1960V separately, but for ee mode a unique factor is used, which is 1.48 ± 0.18. The factors are the numbers which

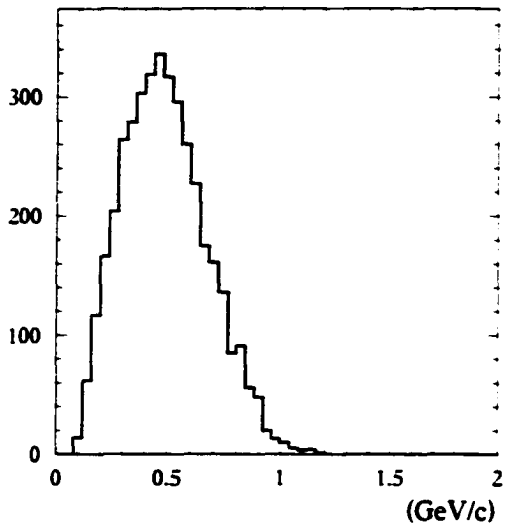

Figure 6.1: Kaon momentum from ϕ decay in $B \to J/\psi\phi K$ MC events.

gave the best agreement on ΔE distribution between MC and the real data in the $B \to J/\psi K^{\pm}$ sample [61]. Again, this is not necessary for SP4 MC because of the good agreement between the simulation and the real data [67].

6.1.3. Tracking Efficiency Correction

For `GoodTracksLoose` tracks, the look-up tables for tracking efficiency were made following a similar method as was used to make the PID look-up tables. By applying track killing [68], which assigns the efficiency from the tables to the single tracks, realistic tracking efficiency for a selected MC event can be obtained. Similarly, the K^0_S efficiency tables were also used to get realistic K^0_S efficiency [69], which was made

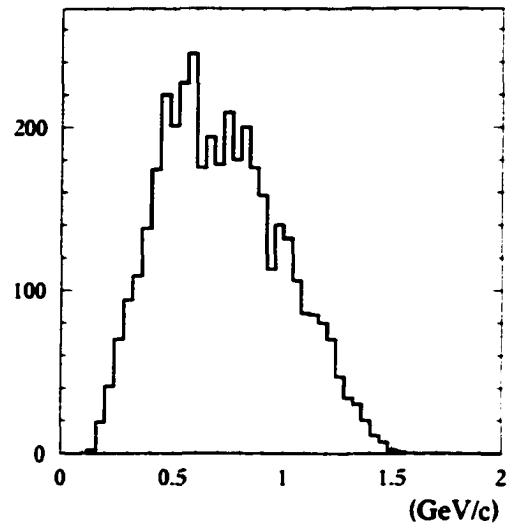

Figure 6.2: The momentum of bachelor kaon in $B^+ \to J/\psi K^+$ MC events.

by binning the K_S^0 decay length as a function of selection efficiency for the control sample.

6.1.4. Single Photon Efficiency Correction

In order to match the single photon efficiency in MC to that determined in the real data, 2.5% of photons were randomly killed in the simulation [70] for modes which have π^0s. But for the modes with η, this is not necessary [71] because the correction is decreasing when the photon energy is increasing, and the energies of the photons from η decays are very high.

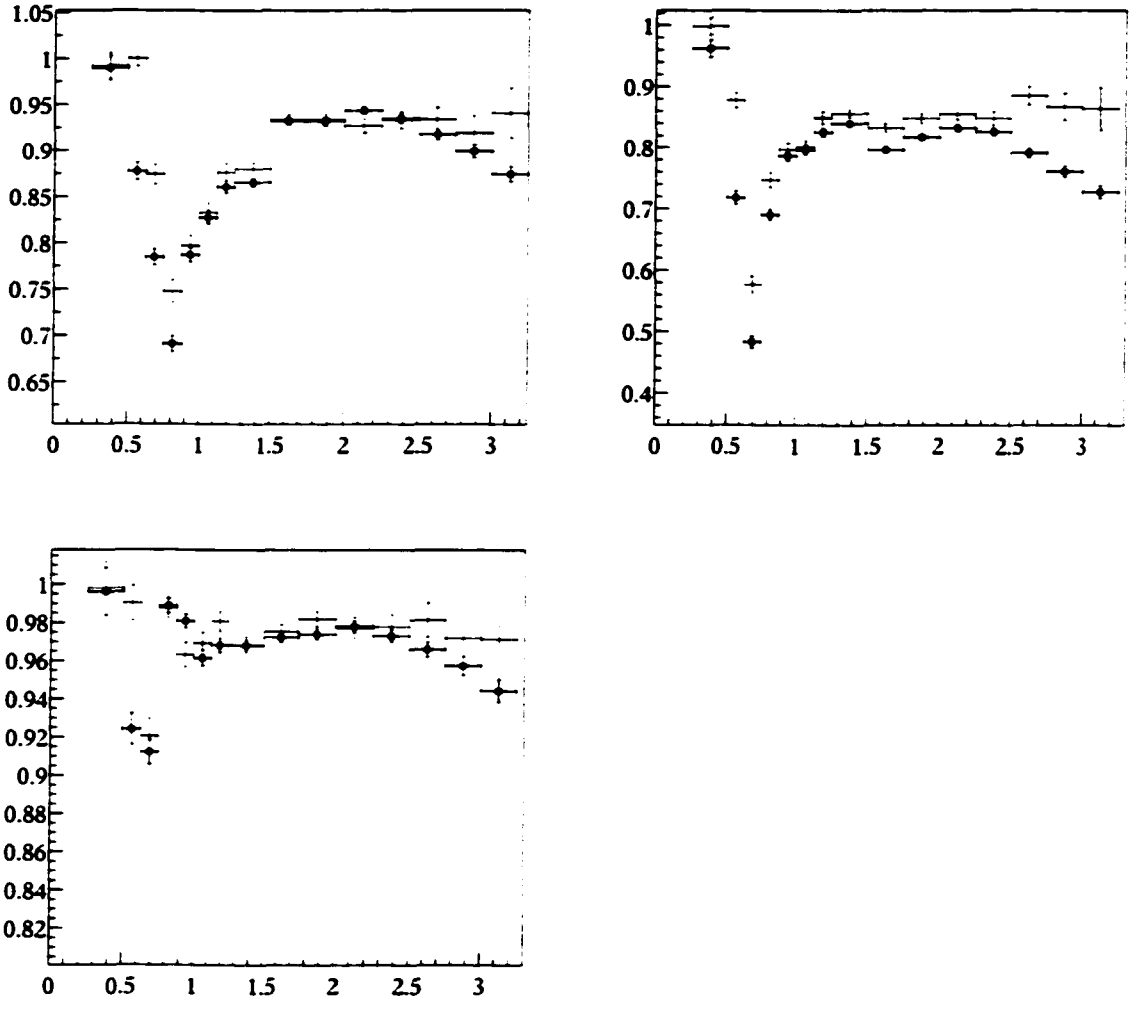

Figure 6.3: The discrepancy of kaon selectors between MC and the real data [66]: `Loose` mode (top left); `VeryTight` mode (top right); `NotAPion mode` (bottom). Dash-cross: MC. solid-cross: Data. The dip region is the momentum range where dE/dx information in SVT and DCH can not provide effective π/K separation any more. and the Cherenkov threshold region for the DIRC.

6.1.5. The Overall Efficiency

The efficiencies after corrections are summarized as in Table 6.2 and Table 6.3 .

Table 6.2: Efficiencies of the three channels with corrections.

Efficiency correction	$B \to J/\psi\eta, \eta \to \gamma\gamma$		$B \to J/\psi\eta, \eta \to \pi^+\pi^-\pi^0$		$B \to J/\psi\eta'$	
	Abs. Eff.(%)	Rel. Eff.(%)	Abs. Eff.(%)	Rel. Eff.(%)	Abs. Eff. (%)	Rel. Eff.(%)
Raw MC	16.3	-	9.9	-	2.7	-
PID Killing	15.5	95.0	9.1	92.0	2.5	93.6
Photon Killing	16.3	-	9.4	95.0	2.7	-
Track Killing	16.3	100.0	9.9	100.0	2.7	100.0
Total	15.5	95.0	8.7	87.4	2.5	93.6

Table 6.3: Efficiencies of the three channels with corrections.

Efficiency correction	$B^+ \to J/\psi K^+$		$B^0 \to J/\psi K^0_S$		$B^0 \to J/\psi$	
	Abs. Eff.(%)	Rel. Eff.(%)	Abs. Eff.(%)	Rel. Eff.(%)	Abs. Eff. (%)	Rel. Eff.(%)
Raw MC	13.9	-	10.3	-	14.5	-
PID Killing	10.8	78.0	8.7	84.1	12.1	83.6
Track Killing	13.6	97.6	10.2	98.8	14.5	99.7
K^0_S Efficiency	-	-	10.3	100.7	-	-
Total	10.6	76.1	8.6	83.7	12.1	83.3

6.2. Event Yield

The yield is calculated as:

$$n_s = n_0 - N_{ARGUS} - N_{J/\psi-Gauss}. \tag{6.1}$$

where n_0 is the total number of events in 3σ signal box. N_{ARGUS} is the combinatoric background, which is the ARGUS function area integrated across 3σ signal region in M_{ES} and has been shown in the previous chapter, and $N_{J/\psi-Gauss}$ is the peaking background, which has been determined in the previous chapter. The statistical error on the yield is given by

$$\sigma_{n_s} = \sqrt{n_0 + \sigma^2_{N_{ARGUS}} + \sigma^2_{N_{J/\psi-Gauss}}}. \tag{6.2}$$

The $B \to J/\psi\eta, \eta \to \gamma\gamma$ signal in 50.9 fb^{-1} on-peak data is shown in Figure 6.4. There are eight events that populate the signal box. The M_{ES} distribution in the ΔE signal region is fit with a Gaussian plus an ARGUS with its shape parameter fixed from the fake J/ψ sample. The background is estimated to be 1.7 events.

The $B \to J/\psi\eta, \eta \to \pi^+\pi^-\pi^0$ results are shown in Figure 6.5 and four events fall into the signal box. The ARGUS shape parameter is again fixed from the fake sample before the M_{ES} distribution is fit. The background is about 1.5 events.

The $B \to J/\psi\eta'$ results are shown in Figure 6.6 and no event in the signal box is found. An ARGUS fit with fixed shape parameter from the fake sample is performed and the background is estimated to be 0.5 events.

By running over on-peak data, one $B^0 \to J/\psi\phi$ event in the signal box is found (Fig 6.7). The combinatoric background from a fit with the fixed ARGUS shape parameter from the fake sample is 0.3 events.

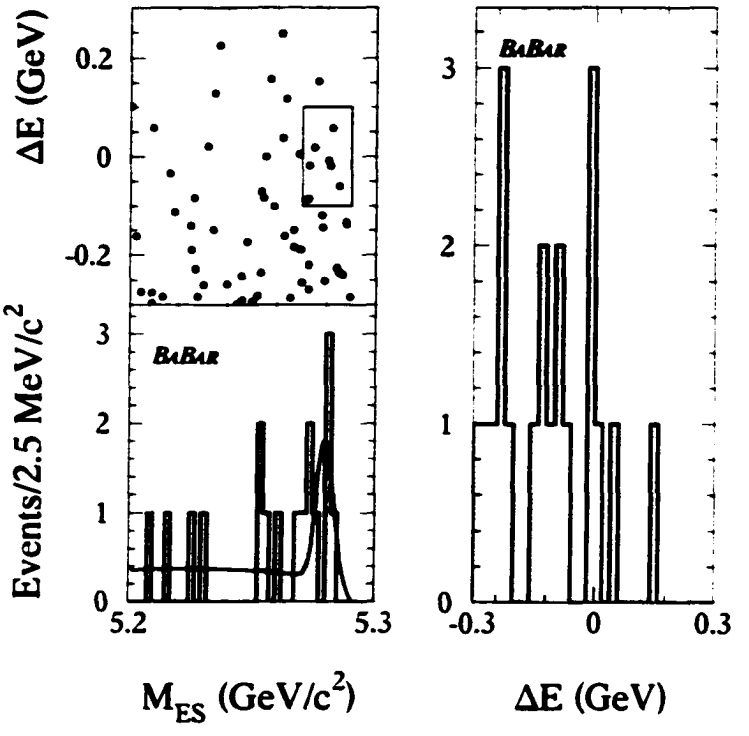

Figure 6.4: On-peak data result on $B \to J/\psi\eta, \eta \to \gamma\gamma$.

The $B^+ \to J/\psi K^+$ signal in on-peak data is shown in Figure 6.8. There are 23 events in the signal box. The M_{ES} distribution in the ΔE signal region is fit with a Gaussian plus an ARGUS with the fixed shape parameter from the fake sample. The background is about 7.8 events. The yield and its error are $n_s \pm \sigma_{n_s} = 15.2 \pm 4.8$.

In Figure 6.9. 13 $B^0 \to J/\psi K^0_S$ events fall into the signal box. The ARGUS shape parameter is fixed from the fake sample before the M_{ES} distribution is fit. The background is estimated to be 3.3 events. The yield and its error are $n_s \pm \sigma_{n_s} = 9.7 \pm 3.6$.

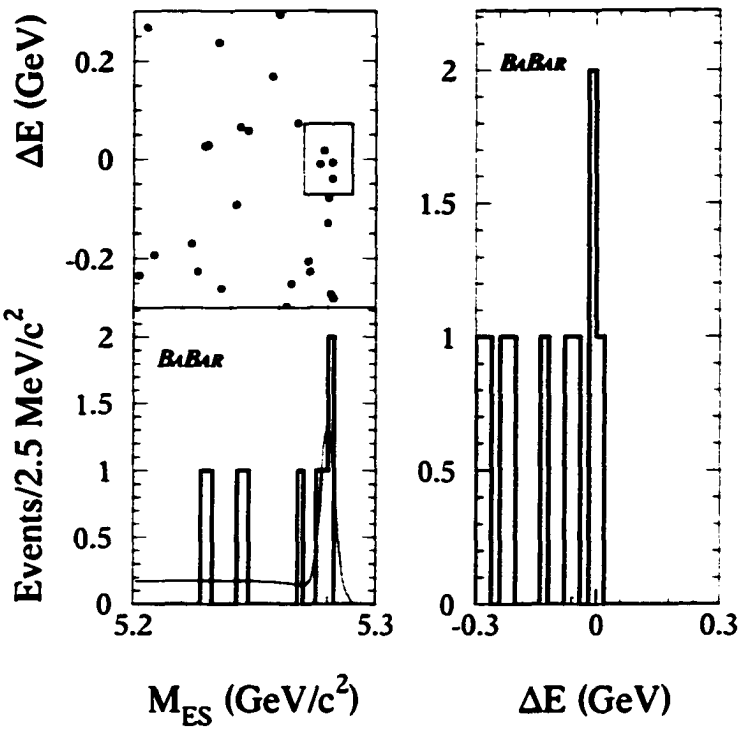

Figure 6.5: On-peak data result on $B \rightarrow J/\psi\eta, \eta \rightarrow \pi^+\pi^-\pi^0$.

6.3. Systematic Errors

The following sources of systematic uncertainty are considered.

6.3.1. Systematic Error from $N_{B\overline{B}}$

Based on the $B\overline{B}$ counting study [51]. a 1.6% systematic error is quoted on the total number of B$\overline{B}$ produced in 50.9 fb^{-1} on-peak data.

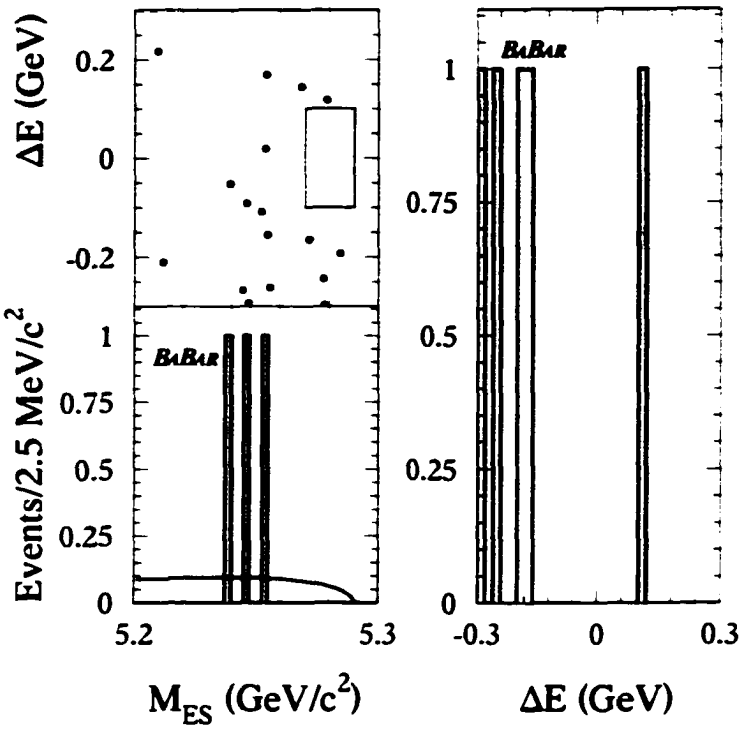

Figure 6.6: On-peak data result on $B \to J/\psi\eta'$.

6.3.2. Systematic Error from Secondary Branching Fractions

The secondary branching fractions involved in this analysis from PDG [19] are :

$$\mathcal{B}(J/\psi \to e^+e^-) = (5.93 \pm 0.10)\% \tag{6.3}$$

and

$$\mathcal{B}(J/\psi \to \mu^+\mu^-) = (5.88 \pm 0.10)\%, \tag{6.4}$$

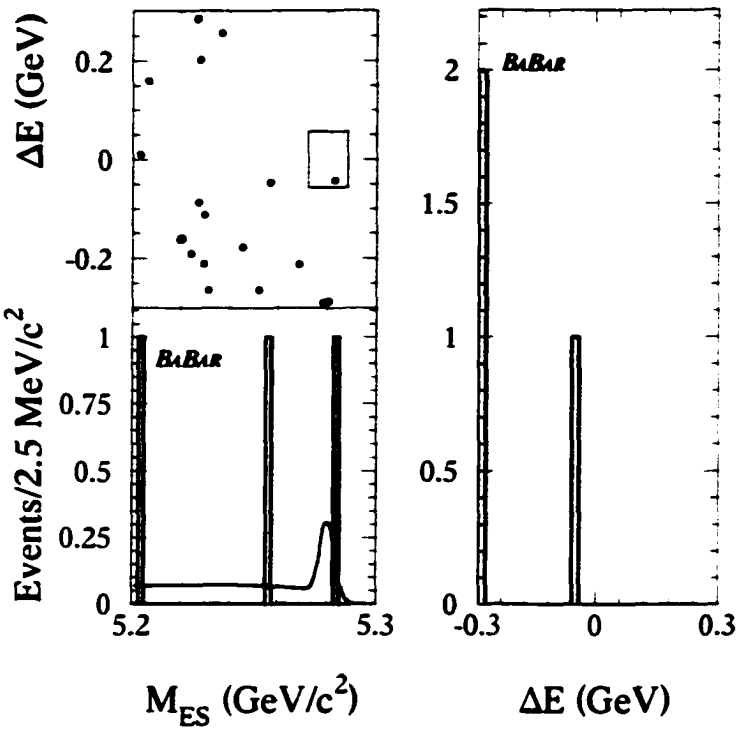

Figure 6.7: On-peak data result on $B^0 \to J/\psi o$.

which give a 1.7% total systematic error.

$$\mathcal{B}(o \to K^+K^-) = (49.2 \pm 0.7)\%. \tag{6.5}$$

which gives 1.4% systematic error.

$$\mathcal{B}(K_s^0 \to \pi^+\pi^-) = (68.61 \pm 0.28)\%. \tag{6.6}$$

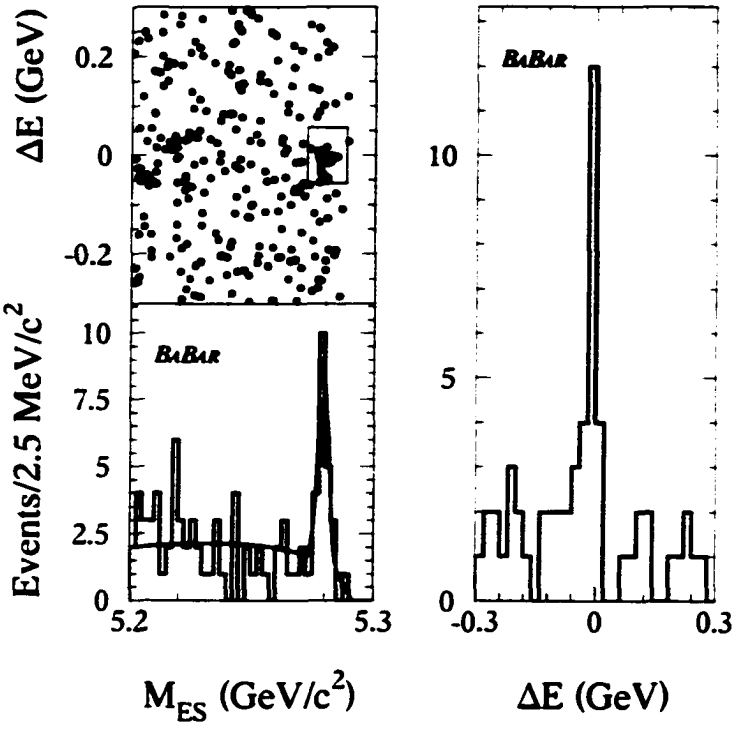

Figure 6.8: On-peak data result on $B^+ \to J/\psi\phi K^+$.

which gives 0.4% systematic error, two η channels.

$$\mathcal{B}(\eta \to \gamma\gamma) = (39.33 \pm 0.25)\% \tag{6.7}$$

$$\mathcal{B}(\eta \to \pi^+\pi^-\pi^0) = (23.0 \pm 0.4)\%, \tag{6.8}$$

which give 0.6% and 1.7% systematic errors respectively, and

$$\mathcal{B}(\eta' \to \pi^+\pi^-\eta) = (44.3 \pm 1.5)\%, \tag{6.9}$$

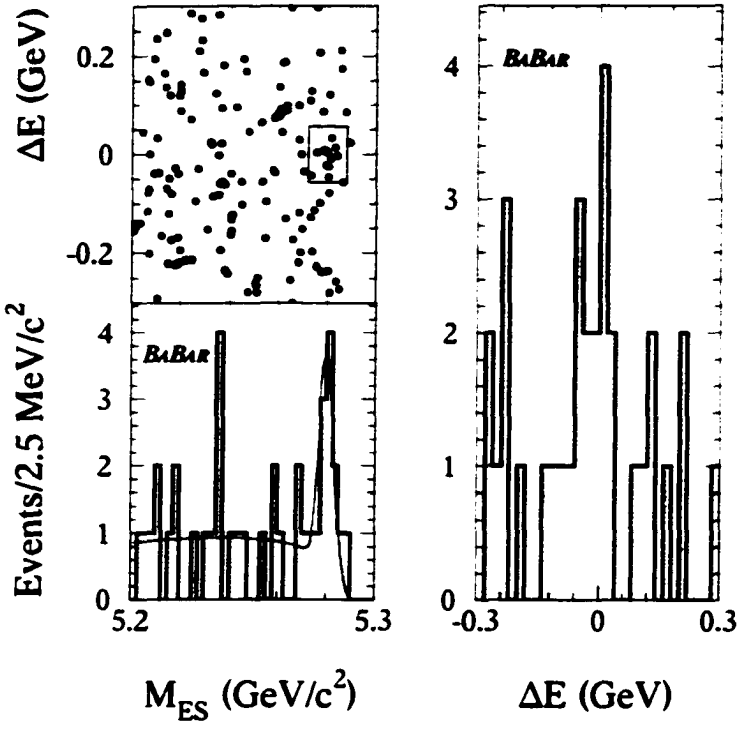

Figure 6.9: On-peak data result on $B^0 \to J/\psi K^0_S$.

which gives a 3.4% systematic error. Add these in quadrature for the channels respectively. the total systematic error from secondary branching fractions are shown in Table 6.4.

6.3.3. Systematic Errors from Efficiency

The raw efficiency for each channel was calculated with the events that satisfy the final selection criteria in the generated MC signal events. The systematic errors associated with the calculations. which are treated as binomial errors. are shown in

Table 6.4: Systematic error from secondary branching fractions.

$B \to J/\psi\eta, \eta \to \gamma\gamma$	1.8%
$B \to J/\psi\eta, \eta \to \pi^+\pi^-\pi^0$	2.4%
$B \to J/\psi\eta'$	3.8%
$B^0 \to J/\psi\phi$	2.2%
$B^+ \to J/\psi\phi K^+$	2.2%
$B^0 \to J/\psi\phi K_S^0$	2.2%

Table 6.5.

Table 6.5: Systematic error from MC statistics.

$B \to J/\psi\eta, \eta \to \gamma\gamma$	1.6%
$B \to J/\psi\eta, \eta \to \pi^+\pi^-\pi^0$	2.2%
$B \to J/\psi\eta'$	4.6%
$B^0 \to J/\psi\phi$	1.6%
$B^+ \to J/\psi\phi K^+$	1.6%
$B^0 \to J/\psi\phi K_S^0$	2.1%

When the signal MC events were generated, three-body phase space was assumed for the three body modes ($B^+ \to J/\psi\phi K^+$, $B^0 \to J/\psi\phi K_S^0$) and two-body phase space for the vector-vector mode $B^0 \to J/\psi\phi$. But there could be some complicated decay dynamics that give different decay amplitudes and angular distributions. Thus there is some uncertainty in the raw efficiencies found in this way.

In order to study the systematic error due to other possible decay models, two extreme samples were generated, one with 100% transversely polarized J/ψ and ϕ,

another with 100% longitudinally polarized J/ψ and ϕ. The corresponding helicity, angular distribution, efficiency and fractional change from the efficiency calculation using phase space are summarized in Table 6.6.

Table 6.6: Efficiency changes due to decay models.

Polarization	d function of lepton	d function of kaon	Efficiency	$\Delta\varepsilon/\varepsilon$
$\lambda_{J/\psi}=0$	$(d^1_{0,\pm1})^2=\sin^2\theta/2$	$(d^1_{0,0})^2=\cos^2\theta$	$B^+\to J/\psi\phi K^+$, 13.86%	0.4%
			$B^0\to J/\psi\phi K^0_S$, 10.14%	1.6%
$\lambda_\phi=0$			$B^0\to J/\psi\phi$, 14.12%	2.6%
$\lambda_{J/\psi}=\pm1$	$(d^1_{\pm1,\pm1})^2=(1+\cos\theta)^2/4$	$(d^1_{\pm1,0})^2=\sin^2\theta/2$	$B^+\to J/\psi\phi K^+$, 13.91%	0.1%
			$B^0\to J/\psi\phi K^0_S$, 10.84%	5.2%
			$B^0\to J/\psi\phi$, 14.42%	0.6%
$\lambda_\phi=\pm1$	$(d^1_{\pm1,\pm1})^2=(1-\cos\theta)^2/4$		$B^+\to J/\psi\phi K^+$, 14.14%	1.6%
			$B^0\to J/\psi\phi K^0_S$, 10.07%	2.2%
			$B^0\to J/\psi\phi$, 14.81%	2.1%

For leptons from J/ψ decays, the angular distribution is $d^{J_{J/\psi}}_{\lambda_{J/\psi},\lambda_{l^+}-\lambda_{l^-}}$. Similarly for kaons, $d^{J_\phi}_{\lambda_\phi,\lambda_{K^+}-\lambda_{K^-}}$. Vector meson J/ψ and ϕ have total angular momentum $J_{J/\psi}=1$, $J_\phi=1$. For 100% transverse polarization they have helicity 0 while for 100% longitudinal polarization they have helicity ±1. The helicity relations of decay daughters are $\lambda_{l^+}-\lambda_{l^-}=\pm1$ and $\lambda_{K^+}-\lambda_{K^-}=0$. $\Delta\varepsilon$ in Table 6.6 was calculated with respect to the raw efficiencies in Table 6.3.

The true angular distribution should lie between these two extreme cases. Thus a uniform distribution can be assumed and the corresponding error calculation can be followed [72]. For each mode, the absolute systematic error was assigned as the difference between the efficiency from the transverse case and the average of the efficiencies from the two longitudinal cases divided by $\sqrt{12}$. The fractional systematic

errors with respect to the raw efficiencies in Table 6.3 are 1.0% for $B^0 \to J/\psi\omega$, 0.4% for $B^+ \to J/\psi\phi K^+$ and 0.9% for $B^0 \to J/\psi\phi K^0_S$.

All corrections in Section 6.1 contribute systematic errors to the efficiency. The systematic error from the lepton PID consists of three components [65], the statistical error from the fit to the inclusive J/ψ sample, the uncertainty from the correction described in Section 6.1.1, and the uncertainty due to the method to use the PID tables. Various uncertainties for different PID combinations were based on Run1 data and SP3 MC. The numbers were still quoted for SP4 MC results without corrections [73]. The errors on ee channel and $\mu\mu$ channel for the selected modes were averaged because the total efficiencies for two channels were not calculated separately.

The PID group evaluated the systematics in the kaon killing tables. The D^* decay control sample from the real data and D^* MC sample were fitted to extract the kaon PID efficiency and to evaluate the systematic error. The possible systematic sources include fitting/counting method for background subtraction, the difference between D^* MC truth and the fitting results in background subtraction, data statistics in background subtraction, D^* MC statistics, the possible difference between the signal MC in this analysis and the D^* control sample, and D^* control sample statistics [74]. For the first five sources, the track-based error on each kaon was given by the PID group then multiplied by the kaon multiplicity of the event to give the total contribution. For the last source, the event-based systematic error was obtained by rerunning

the signal MC with the tables adjusted within the statistical error on the control sample (Table 6.7 and Table 6.8).

For all modes containing charged pions, the kaon veto was applied so the systematic error from kaon PID was included as well.

Table 6.7: Systematic error from kaon PID.

source	$B \to J/\psi\eta, \eta \to \gamma\gamma$(%)	$B \to J/\psi\eta, \eta \to \pi^+\pi^-\pi^0$(%)	$B \to J/\psi\eta'$(%)
fitting/counting	-	1.6	1.6
MC truth difference	-	2.2	2.2
MC statistics	-	0.4	0.4
BG data statistics	-	1.12	1.12
Signal/Control difference	-	3.0	3.0
Control sample statistics	-	0.1	0.1
Total	-	4.2	4.2

Table 6.8: Systematic error from kaon PID.

source	$B^+ \to J/\psi\phi K^+$(%)	$B^0 \to J/\psi\phi K^0_S$(%)	$B^0 \to J/\psi\phi$(%)
fitting/counting	2.4	1.6	1.6
MC truth difference	3.3	2.2	2.2
MC statistics	0.6	0.4	0.4
BG data statistics	1.68	1.12	1.12
Signal/Control difference	5.0	3.5	3.5
Control sample statistics	1.8	3.0	2.8
Total	6.9	5.5	5.4

The error from tracking efficiency has been studied by the tracking group [75]. Following their prescription, a 0.8% fractional systematic error was assigned to every `GoodTracksLoose` track and a 1.3% fractional systematic error was assigned to

every **GoodTracksVeryLoose** track or **ChargedTracks** track. For all modes except $B^0 \to J/\psi K^0_S$, all tracks for B candidates are **GoodTracksLoose** tracks, but for $B^0 \to J/\psi K^0_S$, the two tracks combined for K^0_S are **ChargedTracks** tracks, and their contribution was considered into the error from K^0_S efficiency.

The K^0_S efficiency tables need be used to evaluate this systematic error [76]. It includes three components: systematic error on efficiency for tracks at low radius, which can be evaluated with two **ChargedTracks** tracks; the statistics of the control sample, which is negligible; and the uncertainty in the momentum spectrum. The uncertainty requires use of the alternate tables produced only with K^0_S having $p_t > 1$ GeV/c. A total 5% was obtained.

There is also a systematic error due to using the track smearing. The efficiency with track smearing can be obtained by applying the smearing factor as described in Section 6.1.2. Varying the smearing parameters within $\pm\sigma$ yields a different efficiency. The change on the efficiency is treated as the systematic error due to the track smearing for SP3 MC. This is not necessary for SP4 MC because of the good agreement with the real data.

The photon killing factor metioned above is $(2.5 \pm 1.25)\%$. So the systematic error coming from photon detection probability can be determined by the efficiency changes when rerunning photon killing with factor 3.75% and factor 1.25% [70].

The systematic error from photon energy scale shift and worse resolution in the

real data were considered by varying all mass cuts on neutrals (η, η', π^0) and ΔE to recalculate the results, described in the next section. In order to avoid double counting, energy smearing and shifting were not applied [70].

All errors related to the efficiency corrections are summarized in Table 6.9 and Table 6.10.

Table 6.9: Systematic errors from efficiency corrections.

source	$B \to J/\psi\eta, \eta \to \gamma\gamma$(%)	$B \to J/\psi\eta, \eta \to \pi^+\pi^-\pi^0$(%)	$B \to J/\psi\eta'$(%)
Lepton PID	2.4	2.4	2.4
Kaon PID	-	4.2	4.2
Tracking Efficiency	1.6	3.2	3.2
photon Efficiency	-	5.1	-
Total	2.9	7.7	5.7

Table 6.10: Systematic errors from efficiency corrections.

source	$B^+ \to J/\psi\phi K^+$(%)	$B^0 \to J/\psi\phi K^0_S$(%)	$B^0 \to J/\psi\phi$(%)
Lepton PID	2.0	2.0	2.4
Kaon PID	6.9	5.5	5.4
Tracking	4.0	3.2	3.2
K^0_S Efficiency	-	5.0	-
Total	8.2	8.3	6.7

6.3.4. Systematic Error Estimates from Cut Variations

To obtain a rough measurement of the sensitivity of the results to the placement of the selection cuts, all cuts (except PID) were varied by $\pm\sigma$ if possible, or a reasonable

amount (Table 6.11 and Table 6.12). The branching fractions were recalculated for both changes. Then the average of the magnitudes of the two differences from nominal was taken as an estimate of the systematic error. When the branching fractions were recalculated, the number of events in signal box was recounted, the ARGUS component was reevaluated by refitting, and the peaking background from inclusive J/ψ was reestimated using the new set of cuts. Estimates in Table 6.11 and Table 6.12 are fractional change in result from the nominal values.

Table 6.11: Systematic error estimates from cut variations.

source	$B \to J/\psi\eta, \eta \to \gamma\gamma$(%)	$B \to J/\psi\eta, \eta \to \pi^+\pi^-\pi^0$(%)	$B \to J/\psi\eta'$(%)
$M_{J/\psi} \pm 1\sigma$ (11MeV)	1.4	1.5	2.1
$M_\eta \pm 1\sigma$ (6MeV)	9.8	2.8	7.4
$M_{\eta'} \pm 1\sigma$ (7MeV)	-	-	2.9
$M_{\pi^0} \pm 1\sigma$ (5MeV)	-	9.0	-
π^0 veto $\pm 1\sigma$ (5MeV)	0.5	-	0.6
$\lvert cos\theta_l \rvert$ $\pm$0.05	3.4	3.3	2.9
$\lvert cos\theta_\gamma \rvert$ $\pm$0.05	6.0	-	-
$\lvert cos\theta_T \rvert$ $\pm$0.05	6.2	6.4	5.8
$\Delta E \pm 1\sigma$	4.8	7.0	5.2
Total	14.3	13.9	11.7

6.3.5. Disentangling the Systematic Error on Cut Variation

Traditionally as described above, each cut was changed by $\pm\sigma$ or a reasonable amount, and the subsequent change on the branching fraction could be assigned as systematic error. But statistical fluctuations also play a part and can be significant

Table 6.12: Systematic error estimates from cut variations.

source	$B^+ \to J/\psi\phi K^+(\%)$	$B^0 \to J/\psi\phi K^0_S(\%)$	$B^0 \to J/\psi\phi(\%)$
$M_{J/\psi} \pm 1\sigma$ (11MeV)	9.3	7.1	5.5
$M_\phi \pm 1\sigma$ (5MeV)	2.7	6.9	3.7
$M_{K_S} \pm 1\sigma$ (3MeV)	-	10.3	-
$\lvert cos\theta_T \rvert \pm 0.05$	-	-	7.4
$\Delta E \pm 1\sigma$	6.2	3.9	6.2
Total	11.5	14.8	11.7

for low statistical analyses. BAD168 [77] introduced a method to examine these two contributions based on the statistics theory described in G. Cowan's book [78].

G. Cowan's procedure works as follows. Assume N changes on a cut in a sensible range, which lead to a set of branching fractions $\vec{\mathcal{B}} = (\mathcal{B}_1, \mathcal{B}_2, ... \mathcal{B}_N)$ and the associated statistical errors $\vec{\sigma} = (\sigma_1, \sigma_2, ... \sigma_N)$. The measurements are arranged with ascending yields. $n_1 < n_2 < ... < n_N$. The definitions of these quantities have been described in previous sections. The χ^2 to test the measurement goodness is

$$\chi^2(\lambda) = \sum_{i,j=1}^{N} (\mathcal{B}_i - \lambda)(V^{-1})_{ij}(\mathcal{B}_j - \lambda). \tag{6.10}$$

where V is the covariance matrix with elements

$$V_{ij} = \begin{cases} \sigma_i^2, & i = j \\ \rho_{ij}\sigma_i\sigma_j, & i \neq j \end{cases} \tag{6.11}$$

The correlation coefficients are calculated as $\rho_{ij} = \rho_{ji} = \sqrt{n_i/n_j}$ with $i < j$. The χ^2 is minimized when λ equals the weighted combination of N measurements, $\bar{\mathcal{B}}$, which is obtained by

$$\bar{\mathcal{B}} = \sum_{i=1}^{N} w_i \mathcal{B}_i. \quad w_i = \frac{\sum_{j=1}^{N} (V^{-1})_{ij}}{\sum_{k,l=1}^{N} (V^{-1})_{kl}}. \tag{6.12}$$

The essence of the method is this. If the quantity

$$r = \sqrt{\frac{\chi^2_{min}}{N-1}} \tag{6.13}$$

is larger than 1, then the statistical error σ_i is considered too small to account for the total change in $\mathcal{B}$ due to the variation of this cut. In this case the true error should be inflated by a factor of r times the statistical error. So a compensated part, the systematic error, which one could reasonably say need be added in quadrature, is given by

$$\sigma_{syst} = \sigma_{stat}\sqrt{r^2 - 1} = \sqrt{U[\bar{\mathcal{B}}](r^2 - 1)}. \tag{6.14}$$

where $U[\bar{\mathcal{B}}]$ is the covariance of $\bar{\mathcal{B}}$, which can be calculated with

$$U[\bar{\mathcal{B}}] = \sum_{i,j}^{N} w_i V_{ij} w_j. \tag{6.15}$$

However, if $r \leq 1$, the statistical error can cover the total error, and any extra systematic error associated with the given cut is considered unnecessary.

Each cut in Table 6.11, 6.12 was changed five times. The results are summarized in Table 6.13 and Table 6.14. It is clear that all r values are less than 1 and no systematic error is needed for cut variations.

Table 6.13: $\chi^2_{min}/(N-1)$ test for $B \to J/\psi\eta, \eta \to \gamma\gamma$, $B \to J/\psi\eta, \eta \to \pi^+\pi^-\pi^0$ and $B \to J/\psi\eta'$.

Cut range	$B \to J/\psi\eta, \eta \to \gamma\gamma$	$B \to J/\psi\eta, \eta \to \pi^+\pi^-\pi^0$	$B \to J/\psi\eta'$
$2.939GeV/c^2 < M_{J/\psi} < 3.151GeV/c^2$	0.73	0.91	0+
$0.931GeV/c^2 < M_{\eta'} < 0.985GeV/c^2$	-	-	0+
$0.523GeV/c^2 < M_{\eta} < 0.571GeV/c^2$	0+	0.65	0+
π^0 veto. $(15 \sim 25)MeV/c^2$	0+	-	0+
$0.115GeV/c^2 < M_{\pi^0} < 0.155GeV/c^2$	-	0.72	-
$0.75 < \lvert cos\theta_l \rvert < 0.85$	0.41	0+	0+
$0.75 < \lvert cos\theta_\gamma \rvert < 0.85$	0.94	-	-
$0.75 < \lvert cos\theta_T \rvert < 0.85$	0.13	0+	0+
$0.048GeV < \lvert \Delta E \rvert < 0.096GeV$	-	0.50	-
$0.066GeV < \lvert \Delta E \rvert < 0.133GeV$	0.80	-	0.17

Table 6.14: $\chi^2_{min}/(N-1)$ for $B^0 \to J/\psi\phi$, $B^+ \to J/\psi\phi K^+$ and $B^0 \to J/\psi\phi K^0_S$.

Cut range	$B^0 \to J/\psi\phi$	$B^+ \to J/\psi\phi K^+$	$B^0 \to J/\psi\phi K^0_S$
$2.939GeV/c^2 < M_{J/\psi} < 3.151GeV/c^2$	0.16	0.44	0.33
$0.999GeV/c^2 < M_\phi < 1.039GeV/c^2$	0.18	0.43	0.64
$0.486GeV/c^2 < M_{K^0_S} < 0.510GeV/c^2$	-	-	0.65
$0.75 < \lvert cos\theta_T \rvert < 0.85$	0.53	-	-
$0.038GeV < \lvert \Delta E \rvert < 0.076GeV$	0.09	0.98	0.47

6.3.6. Systematic Error from Background Parameterization

The shape of ARGUS function changes the total background. For each mode, the M_{ES} distribution in ΔE signal region of on-peak data was refitted with the ARGUS shape parameter determined from ΔE sideband. The difference between the new N_{ARGUS} and the original one leads to negligible systematic error for $B \to J/\psi\eta$ and $B \to J/\psi\eta'$, but 1.4% for $B^0 \to J/\psi\phi$, 2.6% for $B^+ \to J/\psi\phi K^+$ and 1.1% for $B^0 \to J/\psi\phi K_S^0$.

The estimation of the peaking background also contributes a systematic error. The J/ψ MC was used to estimate the peaking background for the results. A method to test this peaking background estimation comes from the ΔE sideband in both the real data and the J/ψ MC. The ΔE sideband in these two samples gives different numbers of peaking events, and we use those differences to calculate a systematic error. Quoted as a fractional error the systematics from this source are 6.9% systematic error for $B \to J/\psi\eta, \eta \to \gamma\gamma$, 8.0% for $B \to J/\psi\eta, \eta \to \pi^+\pi^-\pi^0$, 7.1% for $B \to J/\psi\eta'$, 11.9% for $B^0 \to J/\psi\phi$, 5.3% for $B^+ \to J/\psi\phi K^+$ and 1.6% for $B^0 \to J/\psi\phi K_S^0$.

6.3.7. The Total Systematic Error

All systematic errors described above were added in quadrature. The total systematic errors are listed in Table 6.15. There the abbreviated column labels are: $\Delta N_{B\bar{B}}$, which is the systematic error from the total $B\bar{B}$ events; SBF, which is the systematic

Table 6.15: Systematic error summary.

Mode	$\Delta N_{B\overline{B}}$	SBF	MCS	PidTrkG	BkgdP	ModelD	Total ($\sigma_T/\mathcal{B}$)
$J/\psi\phi$	1.6%	2.2%	1.6%	6.7%	12.0%	1.0%	14.1%
$J/\psi\phi K^+$	1.6%	2.2%	1.6%	8.2%	5.9%	0.4%	10.5%
$J/\psi\phi K^0_S$	1.6%	2.2%	2.1%	8.3%	1.9%	0.9%	9.4%
$J/\psi\eta(\gamma\gamma)$	1.6%	1.8%	1.6%	2.9%	6.9%	-	8.0%
$J/\psi\eta(3\pi)$	1.6%	2.4%	2.2%	7.7%	8.0%	-	11.7%
$J/\psi\eta'$	1.6%	3.8%	4.6%	5.7%	7.1%	-	11.1%

error from the secondary branching fractions: MCS, which is the systematic error from MC statistics: PidTrkG, which is the systematic error from PID, tracking efficiency and photon killing: BkgdP, which is systematic error from background parameterization: ModelD, which is the systematic error from the decay models rather than phase space: and Total, which is the total fractional systematic error.

For most of modes, the biggest systematic error comes from the background, which is dominated by uncertainty of the peaking background. For mode $B^+ \to J/\psi\phi K^+$ the biggest systematic error comes from PID because there are three tracks with low momentum that use kaon PID.

Chapter 7

Results and Conclusions

7.1. Upper Limits

The branching fraction and its statistical error are determined as follows:

$$\mathcal{B} = \frac{n_s}{N_{B\bar{B}} \times \varepsilon \times f} = A n_s. \tag{7.1}$$

$$\sigma_{stat} = \frac{\sigma_{n_s}}{N_{B\bar{B}} \times \varepsilon \times f}. \tag{7.2}$$

where acceptance A is the combined factor for the overall efficiency ε, $N_{B\bar{B}}$ and the product of all secondary branching fractions f. The number of signal events n_s, is calculated by

$$n_s = n_0 - n_b. \tag{7.3}$$

where n_0 is the total number of events observed in the signal box, and n_b is the total number of background events, which is the sum of N_{ARGUS} and $N_{J/\psi-Gauss}$.

When the measurement value is close to the physics boundary, generally a single-sided confidence interval, i.e., an upper limit is set. For a Poisson process with n_0 observed and n_b background, the Poisson upper limit N on the signal expected n_s, for which the probability is $1-\varepsilon$ that one could get more than n_0 events in a random experiment, can be obtained by

$$\epsilon = \frac{\sum_{n=0}^{n_0} P(n: n_b + N)}{\sum_{n=0}^{n_0} P(n: n_b)}. \tag{7.4}$$

Here $P(n: n_b + N), P(n: n_b)$ are Poisson distribution functions. The calculation assumes n_b is precisely determined. But in the case of this analysis there are uncertainties in n_b and A. Assuming that a normal distribution for the uncertainty is reasonable (both for the background and the acceptance), the method to incorporate this uncertainty into the upper limit is to convolute the Poisson distribution with two normal distributions for the uncertainties, one for background and the other for acceptance [72].

Suppose we have the value of n_b with an overall (statistical plus systematic) Gaussian error σ_b, and the value of A with an overall error σ_A. For the Poisson upper limit N on n_s at the confidence level (C.L.) 1-ϵ, one can calculate

$$\epsilon = \frac{\sum_{n=0}^{n_0} \frac{1}{\sqrt{2\pi}\sigma_N} \int_0^\infty \int_0^\infty e^{-(\tilde{n}_b+\tilde{n}_s)} \frac{(\tilde{n}_b+\tilde{n}_s)^n}{n!} e^{-\frac{(n_b-\tilde{n}_b)^2}{2\sigma_b^2}} e^{-\frac{(N-\tilde{n}_s)^2}{2\sigma_N^2}} d\tilde{n}_b d\tilde{n}_s}{\sum_{n=0}^{n_0} \int_0^\infty e^{-\tilde{n}_b} \frac{\tilde{n}_b^n}{n!} e^{-\frac{(n_b-\tilde{n}_b)^2}{2\sigma_b^2}} d\tilde{n}_b}$$

$$= \frac{\sum_{n=0}^{n_0} \frac{1}{\sqrt{2\pi}\sigma_A} \int_0^\infty \int_0^\infty e^{-(\tilde{n}_b + \frac{\tilde{A}}{A}N)} \frac{(\tilde{n}_b + \frac{\tilde{A}}{A}N)^n}{n!} e^{-\frac{(n_b - \tilde{n}_b)^2}{2\sigma_b^2}} e^{-\frac{(A-\tilde{A})^2}{2\sigma_A^2}} d\tilde{n}_b d\tilde{A}}{\sum_{n=0}^{n_0} \int_0^\infty e^{-\tilde{n}_b} \frac{\tilde{n}_b^n}{n!} e^{-\frac{(n_b - \tilde{n}_b)^2}{2\sigma_b^2}} d\tilde{n}_b} \quad (7.5)$$

This is an extension of Equation (7.15) in the *BABAR* Statistics Working Group (SWG) report [72]. The parameters in the equation are n_b and A and their respective errors. Here we take $\sigma_N = N\sigma_A/A$. For a 90% C.L. upper limit, we set $\epsilon = 0.1$ and determine N, the expected number of events for this upper limit.

In order to use the calculation tool based on the equation above from the *BABAR* SWG [79], the total systematic error on the branching fraction is considered as the systematic error on the acceptance, i.e., $\sigma_A/A = \sigma_T/\mathcal{B}$ (This is not completely true because although the total systematic error on the branching fraction is dominated by the contribution from the acceptance, the background contributes at some levels. A careful rearrangement does not change the results significantly.). The results are summarized in Table 7.1.

Table 7.1: Expected events, N at 90% C.L..

	n_0	$n_b \pm \sigma_b$	$\sigma_A/A(\%)$	N
$B \to J/\psi\eta, \eta \to \gamma\gamma$	8.0	1.7 ± 0.4	8.0	11.5
$B \to J/\psi\eta, \eta \to \pi^+\pi^-\pi^0$	4.0	1.5 ± 0.9	11.7	6.76
$B \to J/\psi\eta'$	0.0	0.5 ± 0.3	11.1	1.81
$B^0 \to J/\psi o$	1.0	0.3 ± 0.2	14.1	3.60

The resulting upper limits on the branching fractions are shown in Table 7.2. The

information for the calculation of A have been shown in previous chapter.

Table 7.2: Branching fraction upper limits at 90% C.L..

$B \to J/\psi\eta, \eta \to \gamma\gamma$	$< 2.9 \times 10^{-5}$
$B \to J/\psi\eta, \eta \to \pi^+\pi^-\pi^0$	$< 5.1 \times 10^{-5}$
$B \to J/\psi\eta'$	$< 6.3 \times 10^{-5}$
$B^0 \to J/\psi o$	$< 9.2 \times 10^{-6}$

7.2. Combined Upper Limit

When the different measurements of a branching fraction $\mathcal{B}$ or an upper limit on a branching fraction $\mathcal{B}$ are combined, the numbers of the observed, the numbers of the background and the acceptances must be known.

Consider m independent measurements of a branching fraction $\mathcal{B}$. The information on the numbers of the observed, the numbers of the background and the acceptances are given as $\{n_{01}, n_{b1}, A_1\}, \{n_{02}, n_{b2}, A_2\}, \ldots, \{n_{0i}, n_{bi}, A_i\}, \ldots, \{n_{0m}, n_{bm}, A_m\}$. The likelihood function is the product of probability density functions.

$$L(\mathcal{B}) = \prod_{i=1}^{m} P(n_{0i}; n_{bi} + \frac{\mathcal{B}}{A_i}). \tag{7.6}$$

The value of $\mathcal{B}$ is determined by the maximum likelihood estimator [80].

$$\frac{\partial ln L}{\partial \mathcal{B}} = \sum_{i=1}^{m} \frac{n_{0i}/A_i}{\mathcal{B}/A_i + n_{bi}} - 1/A_i = 0. \tag{7.7}$$

If there is uncertainty on the background and the acceptance, then Gaussian smearing is applied [81].

The two η channels were combined to set the upper limit on the branching fraction of $B \to J/\psi\eta$. The result calculated with the calculation tool from the *BABAR* SWG is $< 2.7 \times 10^{-5}$ at 90% C.L.

7.3. Branching Fractions

The modes $B^+ \to J/\psi K^+$ and $B^0 \to J/\psi K^0_S$ have significant signals: $B^+ \to J/\psi K^+$ is 3.1 statistical standard deviations from zero, while $B^0 \to J/\psi K^0_S$ is 2.7 statistical standard deviations from zero. The calculated branching fraction is based on Equation 7.1. ε, n_s and $N_{B\overline{B}}$ are described in previous chapters and the secondary branching fractions for the J/ψ, ϕ, and K^0_S are obtained from PDG [19]. The results are summarized in Table 7.3 including the total summed background events in the signal region. The first error is the statistical error, and the second error is the systematic error σ_T taken from Table 6.15. The derived result for $B^0 \to J/\psi K^0$ is also shown in Table 7.3.

K^0_S is half of the production of K^0 so $\mathcal{B}(B^0 \to J/\psi K^0) = 2\mathcal{B}(B^0 \to J/\psi K^0_S)$.

Table 7.3: Branching fractions for $B^+ \to J/\psi\phi K^+$, $B^0 \to J/\psi\phi K^0_S$ and the derived result for $B^0 \to J/\psi\phi K^0$.

Mode	Efficiency	n_0	$n_s \pm \sigma(n_s)$	$n_b \pm \sigma_b$	Branching Fraction
$J/\psi\phi K^+$	10.6%	23	15.2 ± 4.8	7.8 ± 0.6	$(\ 4.4 \pm 1.4(stat) \pm 0.5(syst)) \times 10^{-5}$
$J/\psi\phi K^0_S$	8.6%	13	9.7 ± 3.6	3.3 ± 0.4	$(\ 5.1 \pm 1.9(stat) \pm 0.5(syst)) \times 10^{-5}$
$J/\psi\phi K^0$					$(10.2 \pm 3.8(stat) \pm 1.0(syst)) \times 10^{-5}$

7.4. Combined Branching Fraction

The two results on $B \to J/\psi\phi K$ are combined in this section. The matrix elements involved in the decay amplitudes are the same for two modes and the partial decay widths follow:

$$\Gamma(B^+ \to J/\psi\phi K^+) = \Gamma(B^0 \to J/\psi\phi K^0). \tag{7.8}$$

So the two partial widths can be combined ideally. But the lifetime of B^0, τ_{B^0}, and the lifetime of B^+, τ_{B^+}, are different so that the total decay widths of B^0 and B^+, Γ_{B^0} and Γ_{B^+} are different [19].

$$\frac{\tau_{B^+}}{\tau_{B^0}} = \frac{\frac{\hbar}{\Gamma_{B^+}}}{\frac{\hbar}{\Gamma_{B^0}}} = 1.073 \pm 0.027. \tag{7.9}$$

Thus when the branching fractions

$$\mathcal{B}(B^+ \to J/\psi\phi K^+) \ = \ \frac{\Gamma(B^+ \to J/\psi\phi K^+)}{\Gamma_{B^+}}. \tag{7.10}$$

$$\mathcal{B}(B^0 \to J/\psi K^0) = \frac{\Gamma(B^0 \to J/\psi K^0)}{\Gamma_{B^0}}. \quad (7.11)$$

are combined. the difference of the total decay widths must be incorporated. As such. the charged mode is used to normalize and we combine

$$\mathcal{B}_1 = \mathcal{B}(B^+ \to J/\psi K^+). \quad (7.12)$$

$$\mathcal{B}_2 = \frac{\tau_{B^+}}{\tau_{B^0}} \cdot \mathcal{B}(B^0 \to J/\psi K^0). \quad (7.13)$$

The formula to combine two measurement based on the maximum likelihood method is:

$$\mathcal{B} = \frac{\frac{\mathcal{B}_1}{\sigma_1^2} + \frac{\mathcal{B}_2}{\sigma_2^2}}{\frac{1}{\sigma_1^2} + \frac{1}{\sigma_2^2}}. \quad (7.14)$$

σ_1 and σ_2 are given by

$$\sigma_1 = \sqrt{\sigma_{st1}^2 + \sigma_{usy1}^2}. \quad (7.15)$$

$$\sigma_2 = \sqrt{\sigma_{st2}^2 + \sigma_{usy2}^2}. \quad (7.16)$$

where σ_{st1}. σ_{st2} are the statistical errors for two measurements and σ_{usy1}. σ_{usy2} are the uncorrelated part of the systematic errors. σ_{usy2} includes the uncertainty from the lifetime ratio in Equation 7.9. The overall statistical error and systematic error

on the combined branching fraction are:

$$\sigma_{stat} = \sqrt{\frac{1}{\frac{1}{\sigma^2_{st1}} + \frac{1}{\sigma^2_{st2}}}}. \tag{7.17}$$

$$\sigma_{syst} = \sqrt{\frac{1}{\frac{1}{\sigma^2_{usy1}} + \frac{1}{\sigma^2_{usy2}}} + \sigma^2_{csy}}. \tag{7.18}$$

where σ_{csy} is the correlated systematic error for two measurements. which includes the systematic error on $N_{B\bar{B}}$. part of the systematic error on PID. part of the systematic error on tracking efficiency. These correlated components were added in quadrature to get the total fractional correlated systematic error. which equals 6.2%. It is trivial to apply the fractional amount to the branching fraction of $B^+ \to J/\psi K^+$ to obtain σ_{csy}. which is 0.27.

The combined result is:

$$\mathcal{B}(B^+ \to J/\psi K^+) = (5.1 \pm 1.3(stat.) \pm 0.5(syst.)) \times 10^{-5}. \tag{7.19}$$

The equal production of B^+B^- and $B^0\overline{B}^0$ pairs at the $\Upsilon(4S)$ resonance is assumed.

7.5. The Invariant Mass and the Helicity

The Dalitz plot for $B^+ \to J/\psi K^+$ final state is shown in Figure 7.1. The kinematic limit is shown on the figure and includes two curves. The upper one is

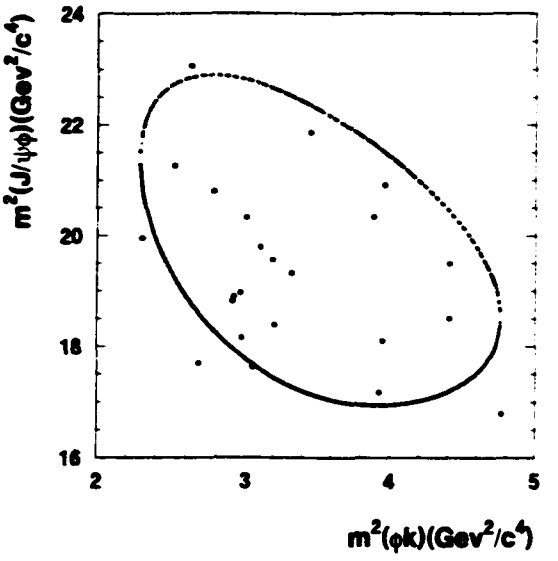

Figure 7.1: The Dalitz plot for 23 $B^{\pm} \rightarrow J/\psi\phi K^{\pm}$ events.

$(m^2(J/\psi\phi))_{max}$ and the lower one is $(m^2(J/\psi\phi))_{min}$:

$$(m^2(J/\psi\phi))_{max} = (E^*_\phi + E^*_{J/\psi})^2 - (\sqrt{E^{*2}_\phi - m^2_\phi} - \sqrt{E^{*2}_{J/\psi} - m^2_{J/\psi}})^2. \quad (7.20)$$

$$(m^2(J/\psi\phi))_{min} = (E^*_\phi + E^*_{J/\psi})^2 - (\sqrt{E^{*2}_\phi - m^2_\phi} + \sqrt{E^{*2}_{J/\psi} - m^2_{J/\psi}})^2. \quad (7.21)$$

where

$$E^*_\phi = \frac{m^2_{\phi K^\pm} - m^2_{K^\pm} + m^2_\phi}{2m_{\phi K^\pm}}. \quad (7.22)$$

$$E^*_{J/\psi} = \frac{m^2_{B^\pm} - m^2_{\phi K^\pm} - m^2_{J/\psi}}{2m_{\phi K^\pm}}. \quad (7.23)$$

The one-dimensional invariant mass of $J/\psi\phi$ distribution and the helicity distri-

bution of the 23 $B^+ \to J/\psi\phi K^+$ events in the signal region are shown in Figure 7.2 and Figure 7.3. The helicity angle for $J/\psi \to l^+l^-$ is defined as the angle between the momentum of the negative charged lepton in the J/ψ rest frame and the momentum of J/ψ in the parent B rest frame. The analogous definition is applied to $\phi \to K^+K^-$ system.

Because of the low statistics, no definitive hint for ψ_g appears in these plots.

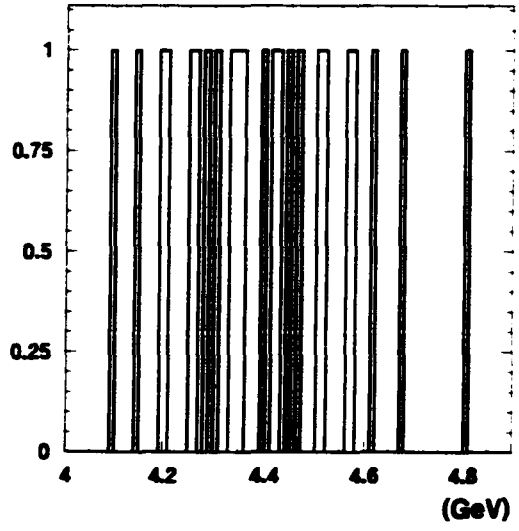

Figure 7.2: Invariant mass of $J/\psi\phi$ for 23 $B^+ \to J/\psi\phi K^+$ events.

7.6. Conclusions

Upper limits have been determined for the modes $B^0 \to J/\psi\eta$, and $B^0 \to J/\psi\eta'$. The results are consistent with the theoretical prediction based on the color-

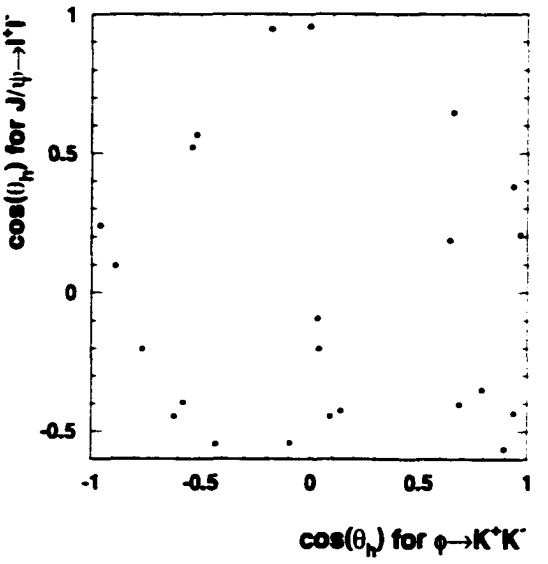

Figure 7.3: Helicity distribution for 23 $B^{\pm} \rightarrow J/\psi K^{\pm}$ events.

suppressed mechanism and the factorization in Section 1.3.1. The upper limit on the branching fraction of $B^0 \rightarrow J/\psi\eta$ is pushed down two orders of magnitude. The upper limit on the branching fraction of $B^0 \rightarrow J/\psi\eta'$ is the first measurement. Furthermore, the information in Table 7.1 for the two $B \rightarrow J/\psi\eta$ modes would correspond to a combined branching fraction of $(1.6 \pm 0.6(stat.) \pm 0.1(syst.)) \times 10^{-5}$, which is comparable to the $B \rightarrow J/\psi\pi^0$ branching fraction [82]. The results have very low statistics, still far away from the feasibility to perform the $sin2\beta$ measurement with inclusive states.

An upper limit has been determined for the mode $B \rightarrow J/\psi\phi$, which is consistent with the naive estimation in Section 1.4. This is the first measurement of this

process where final state interaction is at the leading order. More improvements on theoretical models can be pursued with this measurement. The result without significant observation gives strong support to the factorization mechanism that predicts rescattering should be very small. This helps to remove the 2-fold ambiguity in the $cos2\beta$ measurement with $B \to J/\psi K^*$ events.

We observed evidence for $B \to J/\psi\phi K$ in two modes and determine the branching fractions $\mathcal{B}(B \to J/\psi\phi K^+)=(4.4 \pm 1.4(stat) \pm 0.5(syst)) \times 10^{-5}$ and $\mathcal{B}(B \to J/\psi\phi K^0_S)=(5.1\pm1.9(stat)\pm0.5(syst))\times10^{-5}$. The branching fraction for $B \to J/\psi\phi K$ is consistent with CLEO results [46] but statistically improved. So far no conclusion can be drawn if there is a resonance structure in the final state $J/\psi\phi K$. More data are needed to test the existence of the ψ_g state.

All five measurements are statistically limited now. More data at *BABAR* are expected to improve the results.

Bibliography

[1] G. Luders. Kongl. Dansk. Medd. Fys. **28**. No. 5 (1954):

W. Pauli. Niels Bohr and the Development of Physics. ed. W. Pauli. L. Rosenfeld and V. Weisskopf. McGraw-Hill. New York (1955).

[2] J. H. Christenson *et al.*. Phys. Rev. Lett. **13**. 138 (1964).

[3] *BABAR* Collaboration. B. Aubert *et al.*. Phys. Rev. Lett. **87**. 091801 (2001):

BELLE Collaboration. A. Abashian *et al.*. Phys. Rev. Lett. **87**. 091802 (2001).

[4] D. Gross and F. Wilczek. Phys. Rev. Lett. **30**. 1343 (1973):

H. D. Politzer. Phys. Rev. Lett. **30**. 1346 (1973).

[5] S. L. Glashow. Nucl. Phys. **22**. 579 (1961):

S. Weinberg. Phys. Rev. Lett. **19**. 1264 (1967):

A. Salam. in: Elementary Particle Theory. ed. N. Swartholm. Almquist and Wissell. Stockholm (1968).

[6] M. Kobayashi and T. Maskawa. Prog. Th. Phys. **49**. 652 (1973).

[7] N. Cabibbo. Phys. Rev. Lett. **10**. 531 (1963).

[8] L. L. Chau and W. Y. Keung. Phys. Rev. Lett. **53**. 1802 (1984).

[9] L. Wolfenstein. Phys. Rev. Lett. **51**. 1945 (1983).

[10] M. Beneke. G. Buchalla and I. Dunietz. Phys. Lett. **B393**. 132 (1997).

[11] J. D. Bjorken. Nucl. Phys. B Proc. Suppl. **11**. 325 (1989).

[12] M. Neubert and B. Stech. hep-ph/9705292.

[13] K. G. Wilson. Phys. Rev. **179**. 1499 (1979).

[14] M. K. Gaillard and B. W. Lee. Phys. Rev. Lett. **33**. 108 (1974):
G. Altarelli and L. Maiani. Phys. Lett. **B52**. 351 (1974):
F. J . Gilman and M. B. Wise. Phys. Rev. **D20**. 2392 (1979).

[15] A. J. Buras. M. Jamin. M. E. Lautenbacher and P. H. Weisz. Nucl. Phys. **B370**. 69 (1992).

[16] M. Bauer. B. Stech and M. Wirbel. Z. Phys. **C29**. 637 (1985): Z. Phys. **C34**. 103 (1987).

[17] R. P. Feynman. in: Symmetries in Particle Physics. edited by A. Zichichi. Acad. Press 1965. p. 167:
O. Haan and B. Stech. Nucl. Phys. **B22**. 448 (1970).

[18] A. Deandrea, N. Di Bartolomeo, R. Gatto and G. Nardulli, Phys. Lett. **B318**, 549 (1993).

[19] Particle Data Group, D.E. Groom *et al.*, Eur. Phys. J. C. **15**, 1 (2000).

[20] L3 Collaboration, M. Acciarri *et al.*, Phys. Lett. **B391**, 481 (1997).

[21] Y. Grossman, G. Isidori and M. P. Worah, Phys. Rev. **D58**, 057504 (1998).

[22] M. Suzuki, hep-ph/0001170 (1999).

[23] J.-M. Gerard and J. Weyers, Eur. Phys. J. **C7**, 1 (1999).

[24] B. Blok, M. Gronau and J. L. Rosner, Phys. Rev. Lett. **78**, 3999 (1997).

[25] P. Zenczykowski, Phys. Rev. **D63**, 014016 (2000).

[26] Private communication, Yuval Grossman.

[27] Private communication, Michael Gronau, Stanley Brodsky and Susan Gardner.

[28] M. Gronau, O. F. Hernandez, D. London and J. L. Rosner, Phys. Rev. **D52**, 6356 (1995).

[29] *BABAR* Collaboration, B. Aubert *et al.*, hep-ex/0203008 (2002).

[30] R. L. Jaffe and K. Johnson, Phys. Lett. **B60**, 201 (1976):
R. Jaffe, Phys. Rev. **D15**, 267 (1977):
R. Jaffe, Phys. Rev. Lett. **38**, 195 (1977): err. **38**, 617 (1977).

[31] C. Morningstar and M. Peardon. Phys. Rev. **D60**. 034509 (1999):

GF11 Collaboration. J. Sexton *et al.*. Phys. Rev. Lett. **75**. 4563 (1995):

UKQCD Collaboration. G. S. Bali *et al.*. Phys. Lett. **B309**. 378 (1993):

B. Lucini and M. Teper. JHEP **0106**. 050 (2001).

[32] C. Amsler. Rev. Mod. Phys. **70**. 1293 (1998).

[33] MARK III Collaboration. R. M. Baltkusaitis *et al.*. Phys. Rev. Lett. **56**. 107 (1986):

BES Collaboration. J. Z. Bai *et al.*. Phys. Rev. Lett. **76**. 3502 (1996).

[34] S. Godfrey and J. Napolitano. Rev. Mod. Phys. **71**. 1411 (1999).

[35] N. Isgur and J. Paton. Phys. Rev. **D31**. 2910 (1985):

J. Merlin and J. Paton. J. Phys. **G11**. 439 (1985).

[36] T. Barnes. CalTech PhD thesis. 1977:

T. Barnes. F. E. Close and F. de Viron. Nucl. Phys. **B224**. 241 (1983):

M. Chanowitz and S. R. Sharpe. Nucl. Phys. **B222**. 211 (1983):

M. Flensburg. C. Peterson and L. Skold. Z Phys. **C22**. 293 (1984):

P. Hasenfratz. R. Horgan. J. Kuti and J. M. Richard. Phys. Lett. **B95**. 229 (1981).

[37] MILC Collaboration. C. Bernard *et al.*. Phys. Rev. **D56**. 7039 (1997).

[38] UKQCD Collaboration. P. Lacock *et al.*. Phys. Lett. **B401**. 308 (1997).

[39] CP-PACS Collaboration. T. Manke *et al.*. Phys. Rev. Lett. **82**. 4396 (1999).

[40] F. E. Close and P. R. Page. Nucl. Phys. **B443**. 233 (1995).

[41] F. E. Close. I. Dunietz. P. R. Page. S. Veseli and H. Yamamoto. Phys. Rev. **D57**. 5653 (1998).

[42] I. Dunietz. J. Incandela. F. D. Snider and H. Yamamoto. Eur. Phys. J. **C1**. 211 (1998).

[43] *BABAR* Analysis Document #139. Measurement of Inclusive Production of Charmonium States in B Meson Decays.

[44] G. T. Bodwin. E. Braaten. T. C. Yuan and G. P. Lepage. Phys. Rev. **D46**. 3703 (1992):

A. J. Buras. Nucl. Phys. **B434**. 606 (1995).

[45] F. E. Close. Phys. Lett. **B342**. 369 (1995).

[46] CLEO Collaboration. A. Anastassov *et al.*, Phys. Rev. Lett. **84**. 1393 (2000).

[47] A. Dighe. I. Dunietz. R. Fleischer. Phys. Lett. **B433**. 147 (1998):

M. Suzuki. Phys. Rev. **D64**. 117503 (2001).

[48] P. F. Harrison and H. R. Quinn (Editors). The *BABAR* Physics Book: Physics at an Asymmetric B Factory. SLAC-R-504 (1998).

[49] *BABAR* Techinical Design Report. SLAC-R-95-457 (1995).

[50] *BABAR* Collaboration. B. Aubert *et al.*, Nucl. Instr. and Methods **A479**, 1 (2002).

[51] http://babar-hn.slac.stanford.edu:5090/HyperNews/get/physAnal/1295.html.

[52] GEANT Detector Description and Simulation Tool. http://wwwinfo.cern.ch/asd/geant/index.html

[53] Objectivity.Inc., Mountain View, CA, USA.

[54] ROOT. An Object-Oriented Data Analysis Framework. http://root.cern.ch/root/

[55] H. A. Bethe. Ann. d. Phys. **5**. 325 (1930):
H. A. Bethe. Z. phys. **76**. 293 (1932):
F. Bloch. Z. phys. **81**. 363 (1933).

[56] *BABAR* Analysis Document #194. Trigger and Filter Documentation for Run1.

[57] G. C. Fox and S. Wolfram. Nucl. Phys. **B149**. 413 (1979).

[58] A. Drescher, *et al.*, Nucl. Instr. and Methods **A237**. 464 (1985).

[59] Ralph Sinkus and Thomas Voss. Nucl. Instr. and Methods **A391**. 360 (1997).

[60] S. Brandt. Ch. Peyrou. R. Sosnowski and A. Wroblewski. Phys. Lett. **12**. 57 (1964):

E. Fahri. Phys. Rev. Lett. **39**. 1587 (1977).

[61] *BABAR* Analysis Document #113. Measurement of Branching Ratios of Charged and Neutral B mesons into Exclusive Charmonium Final States.

[62] ARGUS Collaboration. H. Albrecht *et al.*. Z. Phys **C48**. 543 (1990).

[63] http://www.slac.stanford.edu/~milek/excl.ps.

[64] http://www.slac.stanford.edu/BFROOT/www/Physics/Tools/BetaTools/MicroKilling.html.

[65] *BABAR* Analysis Document #126. Lepton identification efficiencies and systematic errors.

[66] Private communication. Aaron Roodman.

[67] http://www.slac.stanford.edu/~coleman/datasp4comparison.html.

[68] http://babar-hn.slac.stanford.edu:5090/HyperNews/get/charmonium/458.html.

[69] http://babar-hn.slac.stanford.edu:5090/HyperNews/get/charmonium/481.html.

[70] http://babar-hn.slac.stanford.edu:5090/HyperNews/get/charmonium/459/2.html.

[71] http://www.slac.stanford.edu/BFROOT/www/Physics/Tools/BetaTools/MicroNeutralKilling-RUN2.html.

[72] *BABAR* Analysis Document #318. Recommended Statistical Procedures for BaBar.

[73] Private communication. *BABAR* Charmonium Working Group.

[74] http://babar-hn.slac.stanford.edu:5090/HyperNews/get/partID/373/1/2.html.

[75] http://www.slac.stanford.edu/BFROOT/www/Physics/TrackEfficTaskForce/TrackingTaskForce-2001.html.

[76] http://www.slac.stanford.edu/ bona/ks/v12/kshort.html.

[77] *BABAR* Analysis Document #168. Measurement of the Branching Fractions for $B^0 \to D^{*-} a_1^+$ using the partial reconstruction technique.

[78] G. Cowan. Statistical Data Analysis. Oxford University Press (1998).

[79] http://www.slac.stanford.edu/~barlow/syslimit.html.

[80] G. Cowan. J. Phys. **G27**. 1277 (2001).

[81] *BABAR* Analysis Document #340, A Calculator for Confidence Intertals.

[82] We use $\mathcal{B}(B^0 \to J/\psi\pi^0) = (2.0 \pm 0.6 \pm 0.2) \times 10^{-5}$ from the *BABAR* Collaboration. Phys. Rev. **D65**. 32001 (2002).